NEUTRON WAVE PROPAGATION
IN A HEAVY WATER, NATURAL URANIUM,
SUBCRITICAL ASSEMBLY

By
JOHNNY HALL DUNLAP

UNIVERSITY OF FLORIDA
December, 1967

For their assistance in the preparation for the experiment, the author thanks the following: Robert H. Hartley, Fred A. Primo, and Henry H. Moos.

Nearly all the data were taken with the assistance of John Whitford, who recorded data, maintained the electronics, and operated the neutron generator. His good work, cheerful spirit and willingness to stay through lunch or after hours for the good of the experiment are appreciated.

The author thanks Nils J. Diaz for his assistance in the use of the CEPTR and BUCKSHOT computer codes and for sharing much of the literature and data he has accumulated concerning heavy water. Dr. Robert G. Cockrell has also been helpful in the area of computer codes.

The author is especially grateful to his good friend and once fellow student, Dr. Ray Sturgis Booth. It is well remembered that it was Booth's analytical approach that located the last "bugs" in the electronic system, making it possible finally to start taking good data early in April, 1965. Also, the heart of the analysis was performed through the use of computer codes written earlier and later modified for this experiment by Booth. In many ways this work is a refined extension of the experimental and data

analysis techniques in neutron wave propagation developed by Perez, Booth and Hartley.

Finally, recognizing that there is no end without a beginning, the author wishes to thank his mother for her original insistence that her sons have at least one year of college education.

TABLE OF CONTENTS

TABLE OF CONTENTS (Continued)

LIST OF TABLES

LIST OF TABLES (Continued)

LIST OF TABLES (Continued)

Table   Page

LIST OF FIGURES

LIST OF FIGURES (Continued)

Figure   Page

xiii

LIST OF FIGURES (Continued)

xiv

LIST OF FIGURES (Continued)

LIST OF FIGURES (Continued)

Abstract of Dissertation Presented to the Graduate Council
in Partial Fulfillment of the Requirements for the Degree of
Doctor of Philosophy

NEUTRON WAVE PROPAGATION IN A HEAVY WATER,
NATURAL URANIUM, SUBCRITICAL ASSEMBLY

By

Johnny Hall Dunlap

December, 1967

Chairman: Professor Glen J. Schoessow
Major Department: Nuclear Engineering

The propagation of neutron waves in a multiplying
medium was studied experimentally, and the resulting dis-
persion law was compared with that predicted by two
theoretical models: a two-group diffusion theory model,
and a Fermi age diffusion model.

Thermal neutron wave propagation in a subcritical
assembly was studied via numerical Fourier analysis of a
thermal neutron pulse of low spatial harmonic distortion
introduced through one boundary of the assembly. One
detector explored the axis of the assembly and supplied a
description of the pulse in the time domain for input to a

1024 channel analyzer. A second detector served to monitor the source strength for each run, providing a means of normalizing data taken at different positions. Corrections for counting resolution losses and background were given careful attention. A computer code was used to perform the Fourier analysis of the pulse, giving amplitude and phase information as functions of frequency for each detector position. The experimental dispersion law was determined by further analysis of this output to obtain the real and imaginary parts of the inverse relaxation length of the Fourier components.

Since an almost perfect fundamental spatial mode had been obtained for the source pulse in the experiment, the corresponding theoretical calculations were specialized to this mode in the transverse directions. The source neutrons were assumed to vary sinusoidally in time, and were introduced into the assembly through the XY plane at Z = 0.

In the two-group treatment, the model led to an equation for a buckling-like term from which the parameters describing attenuation and phase shift as functions of frequency could be found. The Fermi age calculations were based on a complex equation derived by R. B. Perez, which yielded two real, coupled, transcendental equations.

The principal conclusions from the above work are:
(1) The experimentally determined dispersion law is a smooth

function of frequency and both the real and imaginary parts of the inverse relaxation length increase with increasing frequency in the range of frequencies studied.

(2) The calculated dispersion laws from both models agree in general trend with that of the experiment except for a dramatic failure of the two-group theory for frequencies over 350 cps.

(3) Effects of the slowing-down process are important at high frequencies. (That the Fermi age theory describes the high frequency behavior in a more correct fashion than the two-group treatment is probably a consequence of the more accurate description of slowing-down in the age theory.)

(4) Since neither model gives entirely satisfactory agreement with the experiment, it appears that the thermalization effects should be included to describe the dispersion law of well-moderated systems.

(5) The dispersion law poses a severe test to a theoretical model.

In addition to the measurements made with the loaded assembly, the dispersion law for heavy water without fuel was determined, and further analysis of the dispersion data yielded the following experimental values for the diffusion coefficient and the diffusion cooling coefficient, respectively: $D_o = (1.996 \pm .002) \times 10^5$ $cm^2 sec^{-1}$, and $C_o = (3.0 \pm .381) \times 10^5$ cm^4 sec^{-1}.

CHAPTER I

INTRODUCTION

Those involved in the design and control of nuclear reactors are necessarily interested in neutron kinetics in various arrangements of materials. Information in this area has been sought by many persons through the two principal avenues of scientific investigation: by studying the problem through a mathematical formulation based upon an assumed physical model, and by the performance of experimental observations and measurements. Any genuine difference between the experimental results and the predictions based on a model must be attributed to inaccuracies in the model or to errors in the experiment.

A. Neutron Waves

In this dissertation, neutron behavior was investigated in a multiplying medium by studying the propagation of neutron waves in a subcritical assembly of natural uranium and heavy water. The investigation was conducted by theory and experiment followed by a comparison of the results from the two approaches.

It should be understood at the outset that the neutron waves spoken of are not de Broglie waves, but are temporal variations in the neutron population density per unit volume, which may be observed at any position in a moderating or multiplying medium when an appropriate time-dependent source of neutrons is placed at the boundary of the medium.

It is also important to note that when one speaks of a sinusoidal neutron wave, he does not imply a physical impossibility. In practice, the sinusoidal signal rides on top of a background of population density such that the algebraic sum of this background plus the sinusoidal signal is never negative. Thus, one is not forced to find a supply of negative neutrons to compose half of the signal in order to perform the wave experiment. The bottom half of the sinusoidal pattern represents negative neutrons no more than the troughs between the crests of ocean waves represent negative water. Of course, in this analogy, assuming that the air-water interface is spatially sinusoidal, one could represent the depth of the water as the sum of the average depth plus a sinusoidal term which is negative half of the time. Such a representation works well for neutrons also, and is not a source of difficulty in the mathematics.

M. N. Moore (1) draws an illustrative analogy between neutron waves and elastic waves in a viscous dilute gas.

He pictures a volume of gas in a container at one end of which is a flexible diaphragm and points to the similarity between neutron waves and the acoustic waves that can be generated within this container if the diaphragm is caused to vibrate in a harmonic fashion. Moore uses the framework of this analogy to illustrate various other points not under consideration here. For our present purposes, one may observe that the acoustic wave is one in which the population density of the gas molecules could be detected by suitable pressure measuring devices. In the case of neutron waves, the population density of the neutrons may be detected by conventional neutron detectors which report a count rate proportional to the neutron flux. Variations in count rate as a function of time or position give information concerning the neutron wave. An important difference between the neutron wave and the acoustic wave, however, is that the neutron wave is studied in a material medium in which the neutrons scatter about, colliding with nuclei of the medium, but not with other neutrons. With the acoustic wave, there is no medium other than the gas molecules themselves, and their collisions are with each other. The absorption and leakage of the neutrons are not described by the analogy.

B. Historical Notes

Although the propagation of neutron waves was investi-
gated in 1948 by Weinberg and Schweinler (2), who used an
oscillating neutron absorber in a multiplying medium, the
subject has not received as much attention since then as
has been given to related techniques such as exponential and
pulse die-away measurements. Ten years later, in their well-
known text on nuclear reactor theory (3), Weinberg and
Wigner included derivations for the amplitude attenuation,
propagation velocity, and wave length of neutron waves in
infinite media. In 1955, Raievski and Horowitz reported
the determination of the mean transfer free path of thermal
neutrons by measurement of the complex diffusion length.
The measurements were made successfully in both graphite
and heavy water, and a mechanical source was used (4).

In the field of Nuclear Engineering, one turns ultimate-
ly to the Boltzmann equation, writing it in a form which
describes the neutron population density as a function of time,
position, speed (or energy), and direction. The solution of
the Boltzmann equation as applied to a nuclear reactor is too
difficult to perform without resorting to simplifying assump-
tions which result usually in an attendant loss of detail in
the description of the neutrons being studied. The detailed

information most frequently surrendered in order to obtain
a formulation amenable to solution is that of the detailed
direction of travel of the neutrons. Such a surrender is
characteristic of the often-used diffusion theory, in which
isotropic scattering is assumed.

One-group diffusion theory was used by R. E. Uhrig
(5,6) in 1959 and 1961 to relate phase shift and attenuation
to diffusion parameters. The results were compared with
measurements in both water-moderated and graphite-moderated
subcritical assemblies.

R. S. Booth (7) extended the diffusion treatment to
include two groups, and concluded that two-group theory
predicts the presence of two thermal waves that propagate
in the fundamental spatial mode.

Multigroup diffusion theory was applied to a subcriti-
cal assembly by Perez, Booth, Denning, and Hartley (8), and
showed promise of relating resonance wave effects to the
parameters of the system.

Both the experimental methods and theoretical treat-
ments employed in the study of neutron waves have undergone
considerable refinement. The energy dependence was given
additional attention by Perez and Uhrig (9) by use of an
expansion in associated Laguerre polynomials. A power series
in ω/vD was obtained which related the complex inverse

relaxation length to thermalization and diffusion properties.

Refinements in experimental work with neutron waves have appeared in two principal areas: the source used, and the method of data accumulation and analysis. The earlier rotating absorbers or rotating sources have been largely replaced by the use of sinusoidally modulated neutron generators using the (D,T) reaction or the (D,D) reaction. Higher source strengths and a wider frequency range have been obtained. The use of switching circuits and systems of scalers to record different intervals of the detected signal (10) has been replaced by the use of multichannel time analyzers and computer codes.

The use of numerical methods to Fourier analyze the pulses represented an improvement over the data analysis performed by Raievski and Horowitz, who did not have time analyzers, and hence were restricted to less sophisticated evaluation procedures.

Moore (11) extended the Fourier analysis by the inclusion of the Fourier widths, which allow the calculation of not only the dispersion law but also of its higher derivatives. An application of Moore's method was performed by Perez, Booth, and Hartley (12) in the pulse propagation of neutrons in graphite.

Since it is not possible to review here all the literature now in print on the subject of neutron waves, many good papers, both theoretical and experimental, will not be mentioned. However, the reader would find the work of R. L. Brehm (13) helpful, as he explores the use of both one-velocity diffusion theory, and age theory in the P_1 approximation as tools for analyzing neutron wave experiments, and deals with the dispersion parameters of the system as functions of frequency.

The experiment described in the body of this work is of such a nature as to afford an opportunity to seek experimental evidence of the existence of the "exceptional frequencies" first discussed by Moore (14). He spoke of the interesting possibility that there may exist preferred frequencies of excitation which produce a wave having either no spatial attenuation, or no phase change while traversing the medium, or both. This phenomenon is also discussed by Brehm (13 and 15), but it has not yet been found experimentally.

C. A Description of This Study

The principal emphasis in this work is directed toward the experimental approach to the study of neutron wave propagation. The theoretical portions of the work make use of available theories, evaluating the results from these for system parameters appropriate for the nuclear system in which the experiments were performed, so that a critical comparison of theory and experiment can be made. The principal aims of this work may be listed as follows:

1.   To determine the dispersion law for a multiply-
       ing system by experimental means.

2.   To evaluate the performance of various theoretical
       models in describing the dispersion law.

The dispersion law spoken of above is the quantitative relationship between the complex `inverse relaxation length of the neutron waves as a function of frequency. The terminology stems from the use of the term in electromagnetic theory and the fact that the relationship between the complex inverse relaxation length and frequency for neutrons is analogous to that between wave number and frequency for electromagnetic waves. Some secondary, although essential, aims of the work are:

1.   To develop a thermalizing apparatus which will effec-
       tively thermalize neutrons from the (D,T) reaction to
       provide a suitable supply of primarily thermal neutrons
       in the fundamental transverse spatial mode to serve as
       a source for wave or pulse propagation experiments.

2.   To further explore the advantages and disadvantages of the Fourier analysis of pulse propagation data as a method of studying neutron wave propagation (16).

3.   To determine diffusion and thermalization parameters of the moderating media by further analysis of the experimentally determined dispersion law.

4.   To give attention to any exceptional frequencies which may be discovered having unusual properties of propagation.

Wave propagation was studied by means of Fourier analysis of pulse propagation data because:

1.   If a modulated source were used, a new set of data would be necessary for each frequency, whereas one set of pulse data can be Fourier analyzed as a function of many different frequencies.

2.   The use of the method in graphite was successful (16), and the availability of the MOORE MOMENTS code made the method further attractive.

3.   The Fourier analysis of pulse propagation data is a method which itself was considered worthy of further use and evaluation.

In Chapters II and III, two different physical models are adopted and each is adhered to through the mathematical manipulations necessary to arrive at a useful prediction of neutron behavior. Both formulations employ a simplified treatment of the neutron energy variable in addition to using the diffusion approximation. In each, the neutron population density is left as a function of only time and space.

In Chapter II, two-group diffusion theory is used, in which the neutron energy variable is treated by assuming that

the neutrons are in two energy groups. Chapter III is devoted primarily to the solution of equations based on Fermi age diffusion theory. In both of these chapters, a mathematical prediction of the dispersion law for a multiplying medium is obtained and is solved specifically for the subcritical assembly used in the experimental measurements, thus making possible a comparison of theory and experiment.

Chapters IV through VII describe the experiment--the physical conditions imposed upon the neutron population under study, the experimental procedure and data analysis, and the results, including the dispersion law.

Throughout this work, the experiment itself is under study. Measurements are made in order to determine how well the experimental apparatus performs its task of imposing the assumed physical conditions upon the neutrons under study.

Remaining chapters compare the results of experiment and the predictions of theory with the dispersion law being the principal point of comparison. Some clear disagreements are found, the merits of each theory are evaluated, and suggestions for future work are made.

CHAPTER II

DERIVATION OF THE DISPERSION LAW
BY TWO-GROUP DIFFUSION THEORY

The two-group diffusion approximation has already been applied by others to describe neutron wave propagation. The brief derivation given here is based on the work of Booth (7). The two well-known differential equations for this approximation are:

$$D_1 \nabla^2 \phi_1(\vec{r}, t) - \Sigma_R \phi_1(\vec{r}, t) + F_o \phi_o(\vec{r}, t) = \frac{1}{v_1} \frac{\partial}{\partial t} \phi_1(\vec{r}, t) \qquad (2-1)$$

$$D_o \nabla^2 \phi_o(\vec{r}, t) - \Sigma_{ao} \phi_o(\vec{r}, t) + \Sigma_R \phi_1(\vec{r}, t) = \frac{1}{v_o} \frac{\partial}{\partial t} \phi_o(\vec{r}, t) \qquad (2-2)$$

The geometry of interest in this problem is that of a long, box-shaped medium, into which sinusoidally varied thermal source neutrons enter the boundary surface at $Z = 0$. The transverse axes are X and Y. Propagation of the neutron wave down the Z axis is to be studied. Both fast and thermal fluxes are everywhere zero at times $t = 0$, and are zero at the boundaries, except for the source neutrons entering the surface, $Z = 0$, where the diffusion theory relationship between current and flux gradient is used.

11

The fast and thermal fluxes will have the form:

$$\phi_1(\vec{r}, t) = \phi(x,y) \, A_1 \, e^{-\rho z + j\omega t} \tag{2-3}$$

$$\phi_o(\vec{r}, t) = \phi(x,y) \, A_o \, e^{-\rho z + j\omega t} \tag{2-4}$$

Inserting Eqs. 2-3 and 2-4 into the initial set yields:

$$\left[D_1 B^2 - \left(\Sigma_R + \frac{j\omega}{v_1} \right) \right] A_1 + F_o A_o = 0 \tag{2-5}$$

$$\Sigma_R A_1 + \left[D_o B^2 - \left(\Sigma_{ao} + \frac{j\omega}{v_o} \right) \right] A_o = 0 \tag{2-6}$$

where $B^2 = \rho^2 - B_\perp^2$ $\tag{2-7}$

The Eqs. 2-5 and 2-6 form a homogeneous set for which the compatibility condition is:

$$\begin{vmatrix} \left[D_1 B^2 - \left(\Sigma_R + \frac{j\omega}{v_1} \right) \right] & F_o \\ \Sigma_R & \left[D_o B^2 - \left(\Sigma_{ao} + \frac{j\omega}{v_o} \right) \right] \end{vmatrix} = 0$$

By developing the determinant, one obtains an equation for B^4.

$$B^4 - \left[\frac{1}{L^2} + \frac{1}{\tau} + \left(\frac{1}{D_o v_o} + \frac{1}{D_1 v_1} \right) j\omega \right] B^2 +$$

$$\left(\frac{1}{\tau} + \frac{j\omega}{D_1 v_1} \right) \left(\frac{1}{L^2} + \frac{j\omega}{D_o v_o} \right) - \frac{k_\infty}{\tau L^2} = 0 \tag{2-8}$$

Neglecting the term with $j\omega/D_1 v_1$, the roots of Eq. 2-8 are:

$$B_O^2 = \frac{1}{2} \left\{ \left[-\frac{1}{L^2} + \frac{1}{\tau} + \frac{j\omega}{D_o v_o} \right] - \left[\left(-\frac{1}{L^2} - \frac{1}{\tau} + \frac{j\omega}{D_o v_o} \right)^2 + \frac{4}{\tau} \frac{k_\infty}{L^2} \right]^{\frac{1}{2}} \right\}$$

(2-9)

$$B_1^2 = \frac{1}{2} \left\{ \left[-\frac{1}{L^2} + \frac{1}{\tau} + \frac{j\omega}{D_o v_o} \right] + \left[\left(-\frac{1}{L^2} - \frac{1}{\tau} + \frac{j\omega}{D_o v_o} \right)^2 + \frac{4}{\tau} \frac{k_\infty}{L_o^2} \right]^{\frac{1}{2}} \right.$$

(2-10)

Where $\rho_O^2 = B_O^2 + B_\perp^2$ $\qquad\qquad \rho_1^2 = B_1^2 + B_\perp^2$.

The quantity, ρ_O^2 , is the squared inverse complex relaxation length of the thermal neutron wave of frequency ω. The following relationships and definitions will be used to obtain α and ξ, the real and imaginary parts of ρ_O , the inverse complex relaxation length.

$\rho_O = \alpha + j\xi$ $\qquad\qquad\qquad \rho_O^2 = \chi^2 + j\sigma^2$

$\alpha = \left[\frac{1}{2} \left(r + \chi^2 \right) \right]^{\frac{1}{2}}$ $\qquad\qquad \xi = \left[\frac{1}{2} \left(r - \chi^2 \right) \right]^{\frac{1}{2}}$

$r^2 = \chi^4 + \sigma^4$

With the above relationships and Eq. 2-9, α and ξ can be calculated for a nuclear system provided the nuclear parameters in Eq. 2-9 are known. The results of such a calculation, performed through the use of a computer program based on these equations, are presented in Chapter VIII.

CHAPTER III

AGE-THEORY TREATMENT

The dispersion law for the subcritical assembly was
calculated using a Fermi age diffusion treatment. In this
treatment the fission spectrum was described by a Dirac
delta function in lethargy, and the frequency dependence of
the fast fission factor was not taken into account. Under
these conditions, and for the fundamental spatial mode, the
resulting equation[1] for this model is:

$$B_\perp^2 - \rho^2 = \frac{k_\infty}{\epsilon L^2} \exp\left(-B^2 \tau + \rho^2 \tau - iL_s\omega\right) - \frac{1}{L^2} - \frac{i\omega}{D_o} \tag{3-1}$$

A similar result was obtained independently by R. L. Brehm
in Ref. 13.

The dispersion law is contained within Eq. 3-1, but
its solution is not entirely simple. The method by which
the exact solution was obtained will be outlined first; then
a useful series approximation will be derived.

_____

[1]R. B. Perez, personal communication.

A. Exact Solution of the Age-Theory Equation

First express the complex inverse relaxation length, ρ, in terms of its real and imaginary parts:

$\rho = \alpha + i\xi$ Hence $\rho^2 = (\alpha^2 - \xi^2) + i2\alpha\xi.$

Letting $\chi^2 = \alpha^2 - \xi^2$ and $\sigma^2 = 2\alpha\xi$, we next

substitute the expression $(\chi^2 + i\sigma^2)$ for ρ^2 in Eq. 3-1

to obtain:

$$B_\perp^2 - \chi^2 - i\sigma^2 = \frac{K_\infty}{\epsilon L^2} \exp\left[- (B_\perp^2 - \chi^2)\tau + i(\sigma^2\tau - L_s\omega)\right]$$
$$- \frac{1}{L^2} - \frac{i\omega}{D_o}$$

$$(3-2)$$

or:

$$B_\perp^2 - \chi^2 - i\sigma^2 = \frac{K_\infty}{\epsilon L^2} \exp\left[- (B_\perp^2 - \chi^2)\tau\right]\left[\cos\ (\sigma^2\tau - L_s\omega)\right.$$
$$\left. + i\ \sin\ (\sigma^2\tau - L_s\omega)\right] - \frac{1}{L^2} - \frac{i\omega}{D_o}$$

$$(3-3)$$

Equating real and imaginary parts of Eq. 3-3, and using

the equalities:

$$B_r^2 = B_\perp^2 - \chi^2 \qquad \text{and} \qquad B_i^2 = -\sigma^2 \qquad \text{gives}$$

$$B_r^2 = \frac{K_\infty \exp(-B_r^2\tau)}{\epsilon L^2} \qquad \cos\ (B_i^2\tau + L_s\omega) - \frac{1}{L^2} \qquad (3-4)$$

$$B_i^2 = -\frac{K_\infty \exp(-B_r^2\tau)}{\epsilon L^2} \qquad \sin\ (B_i\tau + L_s\omega) - \frac{\omega}{D_o} \qquad (3-5)$$

From these two equations, B_r^2 and B_i^2 were computed for selected values of ω, and from the B_r^2 and B_i^2 values so obtained, α and ξ were calculated as functions of ω, thus yielding the dispersion law as predicted by the slowing-down model.

Some difficulty was encountered in solving for B_r^2 and B_i^2 since Equations 3-4 and 3-5 are coupled in both unknowns and are both transcendental in either B_r^2 or B_i^2. Also, the periodic nature of the trigonometric functions make possible the existence of solutions related to a multiplicity of slowing-down modes. It was found, however, that the additional solutions lie far outside of the range of values of B_r^2 and B_i^2 encountered in the experimental results. Therefore, attention was directed toward the finding of solutions related to the experiment.

The exact solution of Eqs. 3-4 and 3-5 was first accomplished by the use of a lengthy semigraphical method. Briefly, in this method, values of B_r^2 and B_i^2 which satisfy both Eqs. 3-4 and 3-5 for a particular value of ω were obtained by plotting B_r^2 versus B_i^2 for each of the two equations for various values of ω, and observing the points of intersection. For a given ω, the coordinates of the point of intersection are solutions to both equations. The reader is referred to Appendix H, where the method is described more fully, and a

sample calculation is given with the associated graphs and results based upon the initial set of parameters used. The semigraphical solution is a valuable check for alternate methods, and can be used to find the solutions related to higher slowing-down modes. The semigraphical method is also useful because the graphs reveal the manner in which the functions vary, and provide a basis for an estimate of the region of values which should be examined in the search for the higher mode solutions.

Coupled transcendental equations may also be solved by the Newton-Raphson method (17). A computer program for solving Eqs. 3-4 and 3-5 by this iterative technique recently became available, making parameter studies feasible.[1]

B. <u>Approximate Solution to the Age-Theory Equation</u>

The usefulness of the age-theory model would be greatly enhanced if one could obtain from Eq. 3-1 a simple approximation to the dispersion law which would give answers of reasonable accuracy over a useful frequency range. This was

---

[1]The semigraphical solution was performed in late 1965. In 1966, R. G. Cockrell adapted the Newton-Raphson method to the transcendental equations encountered in this work, and Nils J. Diaz wrote a computer program employing this technique in the solution of Eqs. 3-4 and 3-5 and studied the dependence of the results upon the values of various parameters. (N. J. Diaz, personal communication)

found to be possible, and the derivation is now presented, in which the real and imaginary parts of the quantity $(B_\perp^2 - \rho^2)$ are expressed as a power series in frequency.

Defining $F = k_\infty / \epsilon L^2$ and $B^2 = B_\perp^2 - \rho^2$, Eq. 3-1 becomes:

$$B^2 = F \exp(-B^2\tau - iL_s\omega) - \frac{1}{L^2} - \frac{i\omega}{D_o}$$

Multiplying through by τ gives:

$$B^2\tau = F\tau \exp(-B^2\tau - iL_s\omega) - \frac{\tau}{L^2} - \frac{i\tau\omega}{D_o}$$

Add $iL_s\omega$ to both sides; and let

$$\Psi(\omega) = B^2\tau + iL_s\omega$$

$$\Psi(\omega) = F\tau \exp[-\Psi(\omega)] - \frac{\tau}{L^2} - i\omega\left(\frac{\tau}{D_o} - L_s\right)$$

Develop $\Psi(\omega)$ in a power series:

$$\Psi(\omega) = \Psi(o) + \left(\frac{\partial\Psi}{\partial(i\omega)}\right)_o (i\omega) + \frac{1}{2!}\left(\frac{\partial^2\Psi}{\partial(i\omega)^2}\right)_o (i\omega)^2$$

$$+ \frac{1}{3!}\left(\frac{\partial^3\Psi}{\partial(i\omega)^3}\right)_o (i\omega)^3 + \ldots$$

Where

$$\Psi(o) = F\tau \exp[-\Psi(o)] - \frac{\tau}{L^2}$$

$$\frac{\partial\Psi}{\partial(i\omega)} = -F\tau \frac{\partial\Psi}{\partial(i\omega)} \exp(-\Psi) - \left(\frac{\tau}{D_o} - L_s\right)$$

$$\frac{\partial^2\Psi}{\partial(i\omega)^2} = -F\tau \exp(-\Psi)\left[\frac{\partial^2\Psi}{\partial(i\omega)^2} - \left(\frac{\partial\Psi}{\partial(i\omega)}\right)^2\right]$$

$$\frac{\partial^3 \Psi}{\partial (i\omega)^3} = -F\tau \, \exp(-\Psi) \left[\frac{\partial^3 \Psi}{\partial (i\omega)^3} - 3 \frac{\partial^2 \Psi}{\partial (i\omega)^2} \frac{\partial \Psi}{\partial (i\omega)} + \left(\frac{\partial \Psi}{\partial (i\omega)} \right)^3 \right]$$

Ψ and its derivatives at $\omega = 0$ can now be obtained.

$$\Psi(o) = F\tau \, \exp[-\Psi(o)] - \frac{\tau}{L^2}$$

Using $F\tau \, \exp[-\Psi(o)] = \Psi(o) + \frac{\tau}{L^2}$,

$$\left(\frac{\partial \Psi}{\partial (i\omega)} \right)_o = -\left[\Psi(o) + \frac{\tau}{L^2} \right] \left(\frac{\partial \Psi}{\partial (i\omega)} \right)_o - \left(\frac{\tau}{D}_o - L_s \right)$$

$$\left(\frac{\partial^2 \Psi}{\partial (i\omega)^2} \right)_o = -\left[\Psi(o) + \frac{\tau}{L^2} \right] \left[\left(\frac{\partial^2 \Psi}{\partial (i\omega)^2} \right)_o - \left(\frac{\partial \Psi}{\partial (i\omega)} \right)_o^2 \right]$$

$$\left(\frac{\partial^3 \Psi}{\partial (i\omega)^3} \right)_o = -\left[\Psi(o) + \frac{\tau}{L^2} \right] \left[\left(\frac{\partial^3 \Psi}{\partial (i\omega)^3} \right)_o - 3 \left(\frac{\partial^2 \Psi}{\partial (i\omega)^2} \right)_o \left(\frac{\partial \Psi}{\partial (i\omega)} \right)_o \right.$$

$$\left. + \left(\frac{\partial \Psi}{\partial (i\omega)} \right)_o^3 \right]$$

Or:

$$\left(\frac{\partial \Psi}{\partial (i\omega)}\right)_o = -\frac{\dfrac{\tau}{D_o} - L_s}{1 + \Psi(o) + \dfrac{\tau}{L^2}}$$

$$\left(\frac{\partial^2 \Psi}{\partial (i\omega)^2}\right)_o = \frac{\left[\Psi(o) + \dfrac{\tau}{L^2}\right]\left(\dfrac{\partial \Psi}{\partial (i\omega)}\right)_o^2}{1 + \Psi(o) + \dfrac{\tau}{L^2}}$$

$$\left(\frac{\partial^3 \Psi}{\partial (i\omega)^3}\right)_o = \frac{\left[\Psi(o) + \dfrac{\tau}{L^2}\right]\left[3\left(\dfrac{\partial^2 \Psi}{\partial (i\omega)^2}\right)_o \left(\dfrac{\partial \Psi}{\partial (i\omega)}\right)_o - \left(\dfrac{\partial \Psi}{\partial (i\omega)}\right)_o^3\right]}{1 + \Psi(o) + \dfrac{\tau}{L^2}}$$

The last two equations above may be rewritten:

$$\left(\frac{\partial^2 \Psi}{\partial (i\omega)^2}\right)_o = \frac{\left[\Psi(o) + \dfrac{\tau}{L^2}\right]\left[\dfrac{\tau}{D_o} - L_s\right]^2}{\left[1 + \Psi(o) + \dfrac{\tau}{L^2}\right]^3}$$

$$\left(\frac{\partial^3 \Psi}{\partial (i\omega)^3}\right)_o = \frac{3\left[\Psi(o) + \dfrac{\tau}{L^2}\right]^2\left[\dfrac{\tau}{D_o} - L_s\right]^3}{\left[1 + \Psi(o) + \dfrac{\tau}{L^2}\right]^5} + \frac{\left[\Psi(o) + \dfrac{\tau}{L^2}\right]\left[\dfrac{\tau}{D_o} - L_s\right]^3}{\left[1 + \Psi(o) + \dfrac{\tau}{L^2}\right]^4}$$

Next, express B^2 as the sum of its real and imaginary parts, and substitute the above results into the power series for $\Psi(w)$:

$$\left(B_r^2 + i\, B_i^2\right)\, \tau + i\, L_s w = \Psi(o) - \frac{\left(\frac{\tau}{D_o} - L_s\right)(iw)}{1 + \Psi(o) + \frac{\tau}{L^2}}$$

$$+ \frac{1}{2!}\; \frac{\left[\Psi(o) + \frac{\tau}{L^2}\right]\left[\frac{\tau}{D_o} - L_s\right]^2 (iw)^2}{\left[1 + \Psi(o) + \frac{\tau}{L^2}\right]^3}$$

$$+ \frac{1}{3!}\left[- \frac{3\left[\Psi(o) + \frac{\tau}{L^2}\right]^2\left[\frac{\tau}{D_o} - L_s\right]^3}{\left[1 + \Psi(o) + \frac{\tau}{L^2}\right]^5}\right.$$

$$\left. + \frac{\left[\Psi(o) + \frac{\tau}{L^2}\right]\left[\frac{\tau}{D_o} - L_s\right]^3}{\left[1 + \Psi(o) + \frac{\tau}{L^2}\right]^4}\right](iw)^3 + \dots$$

Separation of real and imaginary parts yields:

$$B_r^2 = \frac{\Psi(o)}{\tau} - \frac{\left[\Psi(o) + \frac{\tau}{L^2}\right]\left[\frac{\tau}{D_o} - L_s\right]^2 w^2}{2\tau\left[1 + \Psi(o) + \frac{\tau}{L^2}\right]^3} + \dots \qquad (3\text{-}6)$$

$$B_i^2 = \left[- \frac{\frac{\tau}{D_o} - L_s}{\tau\left[1 + \Psi(o) + \frac{\tau}{L^2}\right]} - \frac{L_s}{\tau} \right] \omega$$

$$- \left[- \frac{\left[\Psi(o) + \frac{\tau}{L^2}\right]^2 \left[\frac{\tau}{D_o} - L_s\right]^3}{2\tau\left[1 + \Psi(o) + \frac{\tau}{L^2}\right]^5} \right.$$

$$\left. + \frac{\left[\Psi(o) + \frac{\tau}{L^2}\right]\left[\frac{\tau}{D_o} - L_s\right]^3}{6\tau\left[1 + \Psi(o) + \frac{\tau}{L^2}\right]^4} \right] \omega^3 + \ldots \qquad (3-7)$$

Since $B_r^2(o) = \frac{\Psi(o)}{\tau}$, $\Psi(o)$ can be replaced by $B_r^2(o)\tau$ in Eqs. 3-6 and 3-7 to yield the following:

$$B_r^2(\omega) = B_r^2(o) - \frac{\left[B_r^2(o) + \frac{1}{L^2}\right]\left[\frac{\tau}{D_o} - L_s\right]^2 \omega^2}{2\left[1 + B_r^2(o)\tau + \frac{\tau}{L^2}\right]^3} + \ldots$$

$$\qquad (3-8)$$

23

$$B_i^2(\omega) = - \left[\frac{\dfrac{1}{D_o} + L_s\, B_r^2(o) + \dfrac{L_s}{L^2}}{\left[1 + B_r^2(o)\tau + \dfrac{\tau}{L^2} \right]} \right] \omega$$

$$+ \left[\frac{\left[B_r^2(o)\tau + \dfrac{\tau}{L^2} \right]^2 \left[\dfrac{\tau}{D_o} - L_s \right]^3}{2\tau \left[1 + B_r^2(o)\tau + \dfrac{\tau}{L^2} \right]^5} \right.$$

$$\left. - \frac{\left[B_r^2(o) + \dfrac{1}{L^2} \right] \left[\dfrac{\tau}{D_o} - L_s \right]^3}{6 \left[1 + B_r^2(o)\tau + \dfrac{\tau}{L^2} \right]^4} \right] \omega^3 + \ldots$$

$$(3-9)$$

$B_r^2(o)$ for the above equations can be obtained by solving
Eq. 3-1 for $\omega = 0$.

$$B_r^2(o) = \frac{k_\infty}{\epsilon L^2}\, \exp\left[- B_r^2(o)\tau \right] - \frac{1}{L^2} \qquad (3-10)$$

From the above results, $B_r^2(\omega)$ and $B_i^2(\omega)$ can be computed if τ, L^2, L_s, D_o, ϵ, and k_∞ are known. Then, from $B_r^2(\omega)$ and $B_i^2(\omega)$, and knowing $B_\perp^2$, one can calculate α and ξ as functions of ω through the use of the relationships:

$$B^2 = B_\perp^2 - \rho^2$$

$$B^2 = B_r^2 + iB_i^2$$

$$\rho^2 = B_\perp^2 - (B_r^2 + iB_i^2)$$

$$\rho = \alpha + i\xi$$

The coefficients in Eqs. 3-8 and 3-9 were evaluated for the parameters in Table 3-1, yielding the following approximations:

$$B_r^2(\omega) = 7.17 \times 10^{-4} - 1.044 \times 10^{-10} \; \omega^2 + \ldots \qquad (3\text{-}11)$$

$$B_i^2(\omega) = -2.024 \times 10^{-6} \; \omega + 5.843 \times 10^{-15} \; \omega^3 + \ldots \qquad (3\text{-}12)$$

In order to test the usefulness of the series approximations, B_r^2 and B_i^2 were evaluated from Eqs. 3-11 and 3-12. From these values of B_r^2 and B_i^2, $\alpha^2 - \xi^2$ and $2\alpha\xi$ were easily obtained and are listed in Table 3-2 for comparison with the results from the exact solution of Eqs. 3-4 and 3-5 by the Newton-Raphson method, using the same input parameters listed in Table 3-1.

An examination of Table 3-2 shows that the series approximation obtained by keeping only the first two terms yields results differing from the exact solution by less than

TABLE 3-1

VALUES OF PARAMETERS FOR THE SUBCRITICAL ASSEMBLY
USED IN THE SOLUTION OF THE AGE-THEORY EQUATIONS
BY THE NEWTON-RAPHSON METHOD

Parameter	Value		Remarks
$B_\perp^2$	0.001263	cm^{-1}	
τ	128.229	cm^2	
k_∞/ϵ	1.1684		
L^2	91.68	cm^2	
L_s	5.0×10^{-5}	sec	Slowing-down time
D_o	2.224×10^5	cm	$D_o = D_v$
v	2.67×10^5	cm/sec	

TABLE 3-2

COMPARISON OF RESULTS FROM THE APPROXIMATE AGE-THEORY
SOLUTION WITH THOSE FROM THE NEWTON-RAPHSON COMPUTER SOLUTION

Frequency (cps)	Exact Age-Theory Solution By Newton-Raphson Technique (Computer Solution)*		Approximate Age-Theory Solution By Series Expansion (Equations 3-11 and 3-12)	
	$(\alpha^2 - \xi^2) \times 10^4$	$2\alpha\xi \times 10^4$	$(\alpha^2 - \xi^2) \times 10^4$	$2\alpha\xi \times 10^4$
0	5.457	0	5.460	0
10	5.463	1.281	5.464	1.272
20	5.470	2.560	5.476	2.544
30	5.491	3.840	5.497	3.816
40	5.524	5.120	5.526	5.088
50	5.558	6.400	5.563	6.359
60	5.608	7.676	5.608	7.629
70	5.660	8.958	5.662	8.899
80	5.717	10.23	5.724	10.17
90	5.781	11.50	5.793	11.45
100	5.866	12.79	5.872	12.71
200	7.099	25.49	7.108	25.32
300	9.138	38.02	9.170	37.77
400	11.99	50.29	12.05	49.84
500	15.57	62.16	15.76	61.79

*Computer solution by N. J. Diaz, personal communication.

1 per cent for frequencies under 400 cps. The only entry in the table with an error exceeding 1 per cent is the 500 cps value of $\alpha^2 - \xi^2$, which differs from the exact result by 1.3 per cent. Therefore, it is seen that the series approximations as set forth in Eqs. 3-8 and 3-9 introduce little additional error compared with that inherent with the age-diffusion-theory model, and is useful over a reasonably wide frequency range.

Four digits are used to present the values in Table 3-2 in order to show the difference between the approximate solution and the exact solution. The reader must not assume from this that the theory itself, even when solved with no further approximations, is good to four-figure accuracy. In Chapter VIII, the accuracy and usefulness of the age-theory model in this application is evaluated by comparing the results of the exact solution of the age-theory equations with the experimental results.

CHAPTER IV

EXPERIMENTAL APPARATUS

A. Introduction

The apparatus assembled for this work consisted of
four units or systems: the subcritical assembly within
which the principal measurements were performed, the neutron
generator which externally supplied the input neutrons for
the subcritical assembly, the thermalizing apparatus inter-
posed between the neutron generator and the subcritical
assembly, and the detector systems. Figure 4-1 shows the
subcritical assembly, neutron generator, and thermalizing
apparatus in their relative operating positions. Each of
these systems will be discussed in turn.

B. Subcritical Assembly

General aspects

A rectangular subcritical assembly using heavy water
as moderator and natural uranium as fuel was designed and
constructed at the University of Florida for this and future

28
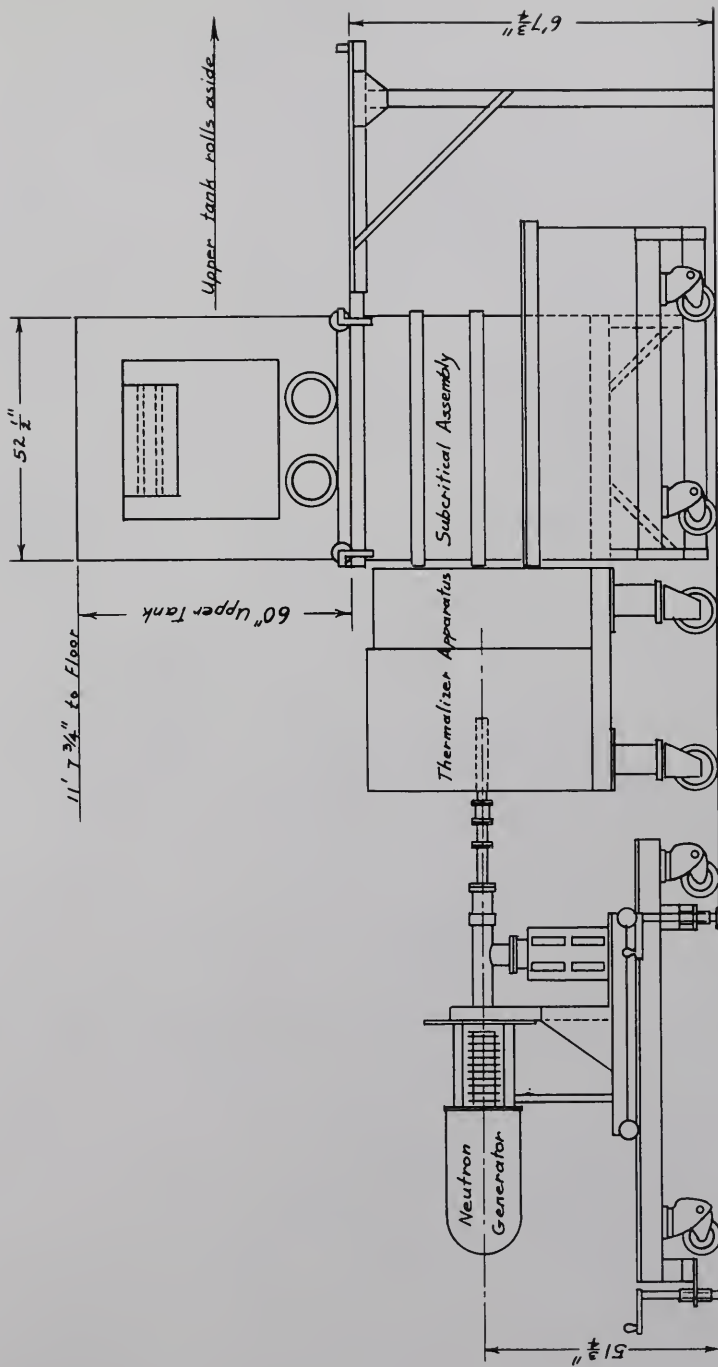
Fig. 4-1. Overall View of the Experimental Apparatus.

experimental work. Figures 4-2 and 4-3 present front and
end views of the assembly. Above the lower tank, which con-
tains the core, is a separate inverted tank with a window,
light, and two gloves on both sides. These features permit
manual positioning of the neutron detector (or detectors)
without opening the assembly and exposing the heavy water
to evaporation or to contamination by light water present
in the air. A small positive pressure is maintained inside
the upper tank by leaking in dry nitrogen at a rate of
approximately 1 ml/sec. Thus any vapor leakage through
seals or welds above moderator level is outwardly directed.
For loading or unloading the core, or whenever complete
access to the inside of the assembly is required, the upper
tank may be rolled aside by means of four attached wheels
and an elevated track structure.

The assembly rests on a heavy steel table inside an
emergency D_2O catch tank which also contains the necessary
pump, valves, and plumbing for filling and emptying the
assembly. See Fig. 4-4. The entire assembly, support table,
and catch tank rest on a rigid steel frame equipped with
leveling screws and 9" casters for a moderate degree of
portability.

Next, the detector positioning apparatus and the core
will be described in greater detail, including not only
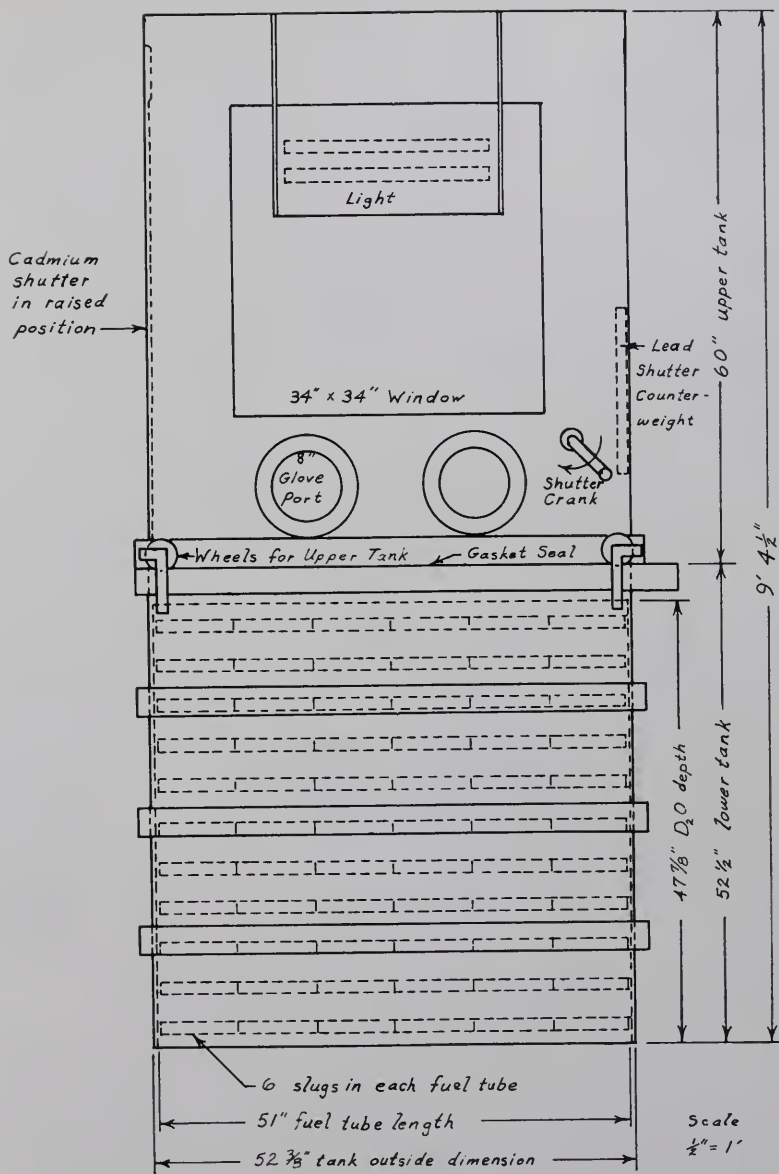
Fig. 4-2.   Front View of the Subcritical Assembly.
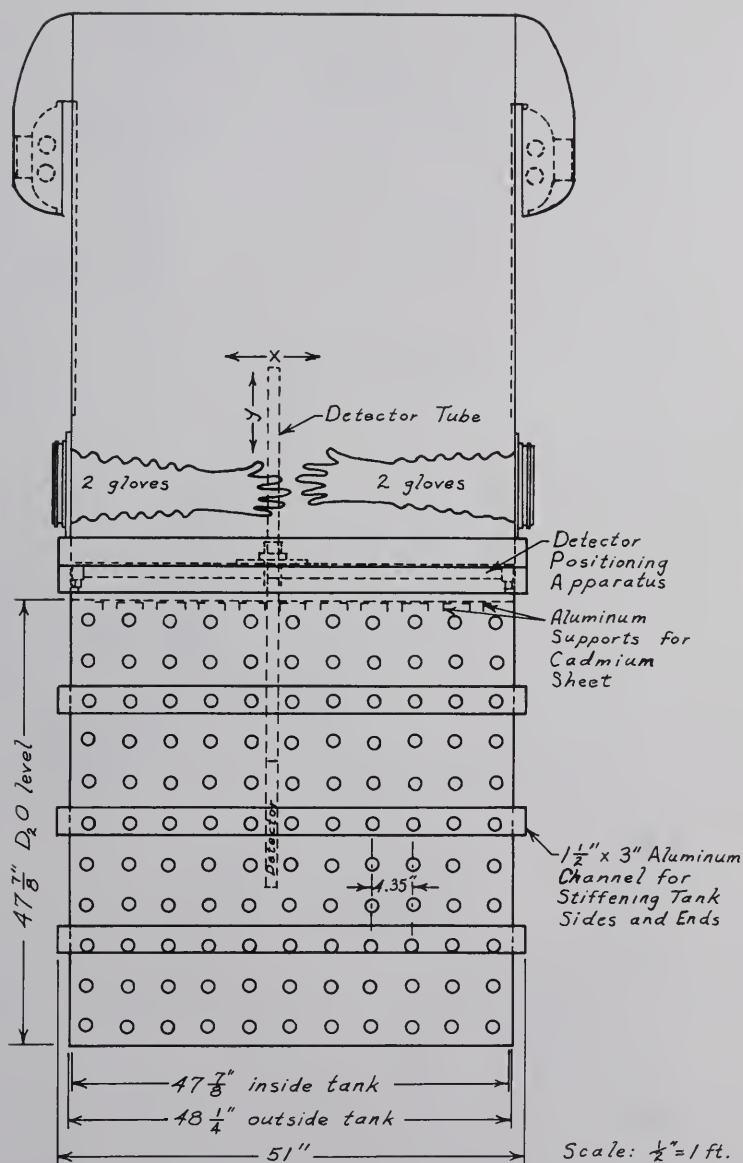
Fig. 4-3.   End View of the Subcritical Assembly.
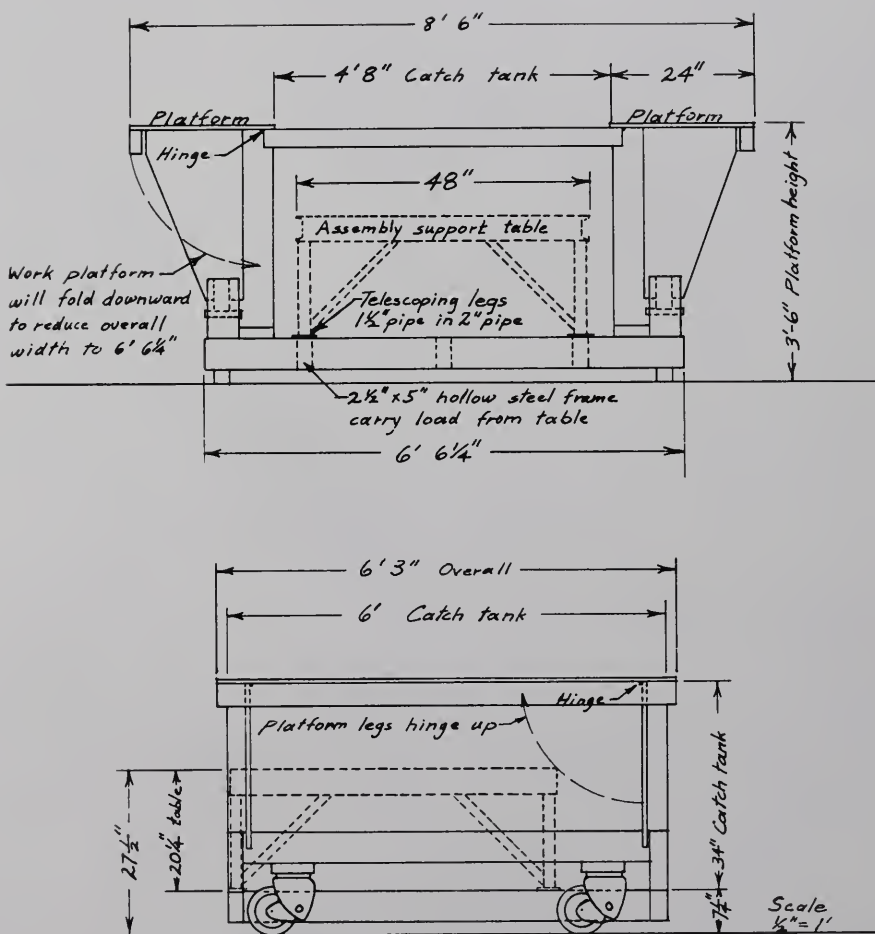
Fig. 4-4. Catch Tank and Support Structure for
the Subcritical Assembly.

information relative to the use of the equipment, but also
those dimensions, deflections and tolerances which are ex-
pected to be important in core calculations or in the con-
sideration of experimental errors stemming from imperfect
core geometry and inaccuracies in detector placement.

Positioning apparatus for detector

Figure 4-3 shows the manually operated detector
positioning apparatus which rolls the length of the assembly
in the Z direction parallel to the fuel tubes. The tracks
are above the water line, screwed to inside walls of the
core-containment tank. An aluminum measuring rod with
drilled holes spaced every 2.50 ± 0.025 cm engages an
alignment pin on the center line of the detector holder,
providing accurate positioning of the Z detector coordinate
from $Z = 5$ cm to $Z = 125$ cm. Screw-operated friction brakes
clamp against the tracks to prevent accidental movement
after the Z position has been set.

A nominal 1" diameter, 12" long He-3 detector may be
wrapped with a small amount of tape at each end to improve
centering, and lowered into a 1.25" OD aluminum tube sealed
at the bottom. This tube slides in a vertical guide and is
locked at the desired Y position by a thumb screw. Most
measurements are made with the center of the detector active

length at Y = 0, the mid-height of the core. Because
the length of the detector lies in the Y direction, trans-
verse flux mapping is best done along the X direction,
for then no part of the detector active volume is more
than 0.5" from the nominal detector position. Furthermore,
since the assembly core and the thermalizing apparatus are
both square in the XY plane, a true flux traverse in the Y
direction should differ little from that in the X direction
if the influence of epicadmium neutrons scattered from the
laboratory floor is negligible.

Since a full fuel loading consists of 121 fuel tubes
in a square array of 11 columns containing 11 fuel tubes
each, there are only 10 vertical YZ planes which are midway
between adjacent YZ columns of fuel tubes. These 10 planes
provide the most useful and natural detector positions for
flux mapping across the core if thermal flux depression by
the fuel is not the object of study. For convenient and
accurate detector placement, 10 alignment holes were drilled
into the transverse beams of the detector positioning appa-
ratus for an alignment pin.

Since one column of fuel tubes lies in the central
plane of the core, at X = 0, axial measurements which would
ordinarily be made with the detector placed on the true Z
axis must be made in a plane offset from the center plane.

If the 10 planes described above are numbered from one side of the core to the other, planes 5 and 6 are closest to the Z axis, and are at $X = \pm 2.175"$, where the dimension is half the lattice spacing of 4.35". All of the so-called Z axis measurements in this work were made in plane number 6. No problem should arise from this offset because if the fundamental spatial mode is well established, measurements made along a line parallel to the Z axis are related to true Z axis measurements through a multiplicative constant, which in this case is almost unity.

Core

Figure 4-3 shows the nearly optimum lattice spacing of approximately 4.35" for a core using D_2O and Mark I solid natural uranium slugs in a square lattice. This spacing produces 11 unit cells across the inside tank dimension of 47.87". Other lattice spacings are obtainable by leaving some fuel positions vacant or by constructing additional pairs of core support plates. The full loading requires 726 slugs in 121 horizontal fuel tubes 51" long, each containing six slugs with an accumulated length of 50.5". Moderator (and possibly a few tenacious gas bubbles) occupy the small remaining volume of the tubes. The machined diameter of the uranium metal is 1.000". Aluminum cladding

adds 1/16" to the diameter, giving a nominal outside diameter
of 1.0625" ± manufacturing tolerances. The length of each
slug, including end cladding measures approximately 8.41".

The fuel tubes have an OD of 1.25", a wall thickness
of 0.049" (stubs gauge no. 18), and are of ALCOA alloy
6061-T6, the same material used in the construction of the
subcritical assembly. This fully tempered alloy has the
following specifications: tension yield = 40,000 psi, tension
ultimate = 45,000 psi, shear = 30,000 psi. Its alloying ele-
ments have relatively low absorption cross sections and are:
0.25% copper, 0.6% silicon, 1.0% magnesium, and 0.25% chromium.
Aluminum and "normal impurities" constitute the remainder.
A calculation of the thermal neutron cross section for this
alloy is included in Appendix E. The resulting alloy is
also unusually resistant to corrosion in water. Each fuel
tube constitutes a uniformly loaded horizontal beam supported
near the ends and has a measured maximum deflection of 1/8"
at the middle. It is likely that deflections up to 1/4"
could be tolerated, particularly since the deflections are
in the Y direction and since most transverse flux studies
with this assembly are done in the X direction for reasons
already given. The design calculations had selected stubs
no. 20 (0.035" wall), but 1.25" OD tubing was not available
in wall thickness less than no. 18. Since the 18 gauge

tubing used weighs 0.210 pounds per foot, 121 tubes put 108
pounds of structural material into the core. This figure
could be reduced to 77 pounds safely if 20 gauge 6061-T6
tubing were available.

Ignoring deflections caused by hydrostatic forces, and
provided that the correct amount of moderator is present, core
dimensions are 47.87" x 47.87" x L, where L = 50.5" if the
core length is taken to be the accumulated length of 6 fuel
slugs. L = 51.12" if the core length is taken to be the
moderator-filled dimension between fuel tube support plates.
(The moderator-filled dimension exceeds the fuel length be-
cause the fuel tubes extend beyond the slugs by about 0.25"
on each end, and because of clearances required for loading
and unloading the core.) If one wishes to take into account
the additional small thickness of moderator present in the
0.38" space provided for movement of the cadmium shutter,
L = 51.50" with shutter up, and about 51.4" with shutter
down. (The shutter is a 0.030" sheet of cadmium cemented
to a 0.0625" aluminum backing sheet.) When the shutter is
lowered, it displaces moderator. Therefore, if the tank is
filled to a depth of 47.87" when the shutter is down, the
level will be less by about 0.08" when the shutter is raised.
(The 47.87" dimension corresponds to the lower surface of the
cadmium sheets which cover the upper moderator boundary.)

The outward deflection of the tank walls mentioned above is a maximum of approximately 0.1" on each of the two largest side panels, at a depth of about 30". Therefore, the maximum inside tank width would exceed the nominal value of 47.87" when the tank is filled with moderator. The bottom of the core tank rests on a steel table of such rigidity that deflections in the bottom core boundary are negligible.

Cadmium sheet, 0.030" thick, is attached to all outer surfaces of the core containment tank except for the end that has the movable cadmium shutter. Cadmium sheet in smaller, movable pieces also lies just above the water-level surface. Therefore, with the shutter down, the core has cadmium on all six boundaries.

C. Neutron Generator

The neutron generator used was model no. 9505, serial no. 52, manufactured by the Texas Nuclear Corporation of Austin, Texas. The neutron generator itself is shown in Fig. 4-1 along with the other major items of experimental equipment. The associated high voltage supply and control console are not shown. Figure 4-1 shows the generator mounted on a wheeled apparatus with elevating screws and an eight-foot-long track on which the generator could be rolled without disturbing alignment with the reentrant tube of the

thermalizer apparatus. This wheeled hardware was constructed at the University of Florida and is not a standard part of the generator as supplied by the manufacturer.

The original outside dimensions of the target end of the generator exceeded the inside diameter of the reentrant tube of the thermalizing apparatus, and was replaced by a redesigned assembly of smaller dimensions, with no glass parts and no suppressor ring. This proved satisfactory.

The neutron generator is basically a Cockcroft-Walton linear accelerator with a maximum accelerating voltage of 150 KV. Neutrons may be produced by either the (D,n) reaction with a tritium target, yielding neutrons of 14.74 MeV, or the (D,n) reaction with a deuterium target, which gives 2.86 MeV neutrons. The lower energy is desirable, but the tritium target was chosen because of its much greater yield. During this work, the maximum obtainable deuteron beam current as indicated by a microammeter circuit between target and ground was about 150μamp for continuous beam operation. During pulsing, with a typical duty cycle of 5 per cent, the time-averaged beam current was less than 10μamp.

No further description of the neutron generator will be given here as it is described in the manufacturer's literature.

The reader is also referred to the work of Hartley (18) for a description of the electronic equipment required to determine the pulse duration and frequency and to synchronize the data-recording equipment with the emission of the pulse from the generator.

D. Thermalizing Apparatus

In order to study the propagation of a thermal neutron pulse or wave in the subcritical assembly, it was considered necessary to assemble a thermalizing apparatus for the purpose of receiving 14 MeV neutrons emitted from the small target of the neutron generator and delivering these to the four-foot-square source boundary of the subcritical assembly as thermal neutrons in the fundamental spatial mode having a cosine shape in the X and Y directions.

After considerable experimentation with various thicknesses of graphite, water, lead and steel, an almost optimum arrangement was determined, and is shown in Fig. 4-5. Graphite serves as the final thermalizing and flux-shaping medium. A 48" x 48" x 17" stack of machined graphite is located outside the water tank. An additional 48" x 47.5" x 12" stack of rough, unmachined graphite was added inside the 49" x 48" x 31" water tank, bringing the graphite to a total thickness of 29", and a total weight of
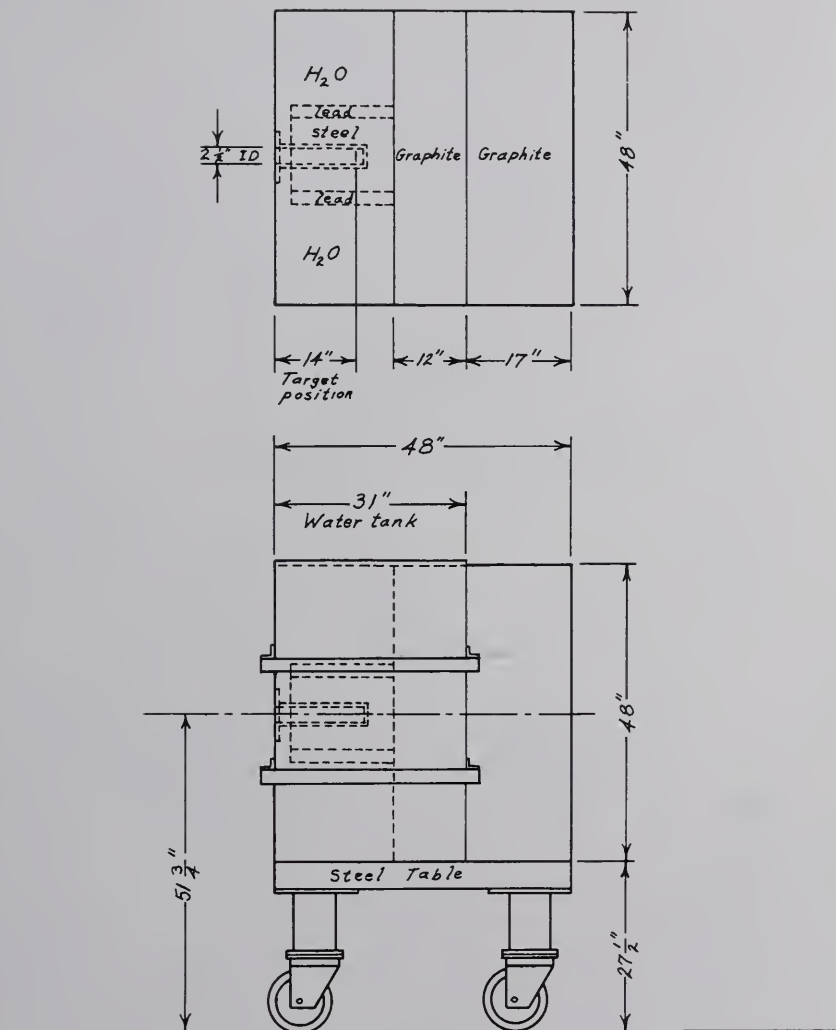
Fig. 4-5.   Thermalizing Apparatus.

about 3800 lbs.

Four inches of steel in the form of steel bricks, and about two inches of lead sheet surround the reentrant tube housing the target end of the neutron generator as shown in Fig. 4-5. The relatively large inelastic scattering cross sections of these heavier materials serve to reduce 14 MeV neutrons to lower energies at which graphite is an efficient moderator. The 2" x 4" x 8" steel bricks, machined and welded where necessary to reduce streaming and to improve stacking, were available from earlier neutron wave work.

Ordinary water occupies the remaining volume of the thermalizing tank, usefully filling voids and cracks. Measurements showed that the presence of water reduced the total neutron intensity at the output face of the graphite stack by a factor of 1.6, while reducing the epicadmium intensity by a greater factor of approximately 3.4. These two effects resulted in an increase in the cadmium ratio from 40 to 90 upon filling the dry tank with water. These measurements were made with the thermalizing apparatus away from the subcritical assembly. The detector was a 12" He-3 detector. The cadmium measurements were made with a cylinder of cadmium wrapped around the detector.

Water should not be regarded as merely an inexpensive substitute for graphite in its use here. A measurement was

made after approximately 4 cubic feet of additional graphite
was placed adjacent to the stack already in the tank, dis-
placing an equal volume of water. There was no measurable
improvement in intensity or cadmium ratio at the output face.
Therefore that additional graphite was removed in order to
avoid unnecessary broadening of the signal pulse. An effort
was made to use no more graphite than needed to produce a
useful cadmium ratio and to provide a sufficient volume for
adequate development of the fundamental spatial mode at the
output face. Graphs to be presented later show that the
thermalized pulse is much broader than the input width of
two msec, and associated with this broadening is an undesir-
able attenuation of the high frequency content of the source
pulse which presents a limitation in the experiment.

It was found that the pulse does not broaden nearly
so much in passing through light water as it does in graphite.
A detector placed in the corner of the water tank, about 27"
from the target, sees a nearly rectangular pulse with a very
rapid rise to saturation, and a rapid decay. Graphs of the
pulse are included in Appendix C. The difference between the
two materials is largely related to the absorption cross
sections. Therefore it is concluded that the water used in
the thermalizing tank is far less detrimental in widening
the output pulse than an equal volume of graphite would be.

At one time, heavy water was somewhat wishfully considered for use as the best possible thermalizing medium in place of part or all of the graphite. Now, in retrospect, it appears fortunate that this was not done because in view of the above considerations, it appears likely that the very low absorption cross section of D_2O would have resulted in an even wider output pulse than an equal volume of graphite in this application.

The water also serves as shielding for the target, and greatly diminishes leakage of epicadmium neutrons from the back and side surfaces of the tank. It is important that such leakage be small because epicadmium neutrons can scatter into the subcritical assembly and become an extraneous signal entering the wrong surface and out of phase with the desired input.

Flux maps at the face of the thermalizing apparatus are presented in Appendix A. Further information about the performance of the thermalizing apparatus is included in later chapters.

E. Detector Systems

Two detector systems were employed. One system used a 12" He-3 detector and terminated with equipment which produced binary and digital records of the neutron pulse shape

in the subcritical assembly. Figure 4-6 describes this system. A second system, employing a 6" He-3 detector, was used to monitor the source strength from the neutron genera-tor, and is shown in Fig. 4-7. Oscilloscope displays of the signal pulse (detector system response to individual neutrons) at various points in each system are reproduced in Figs. 4-8 and 4-9 for the 12" and 6" systems respectively. In both systems, the signal rise time was 0.3 μsec or less, and the pulse fell to 1/e of its maximum value in 2 μsec or less. Figure 4-10 presents graphs of count rate versus high voltage for the two systems. The operating voltages used were higher than ordinarily encountered with these detectors because of the length of cables required.

Additional information related to detector system resolving time, count rates, and resolution loss corrections is presented in Chapter V and in the appendices.
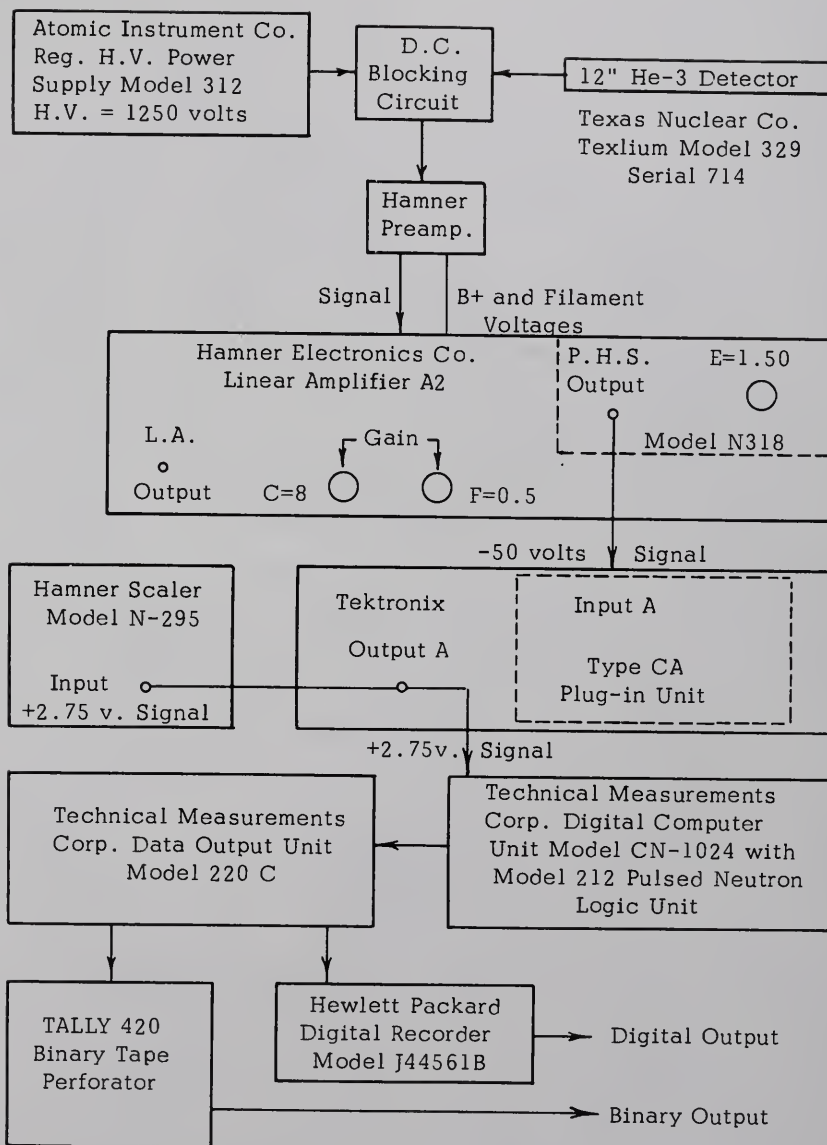
Fig. 4-6. Diagram of the Principal Detector System.
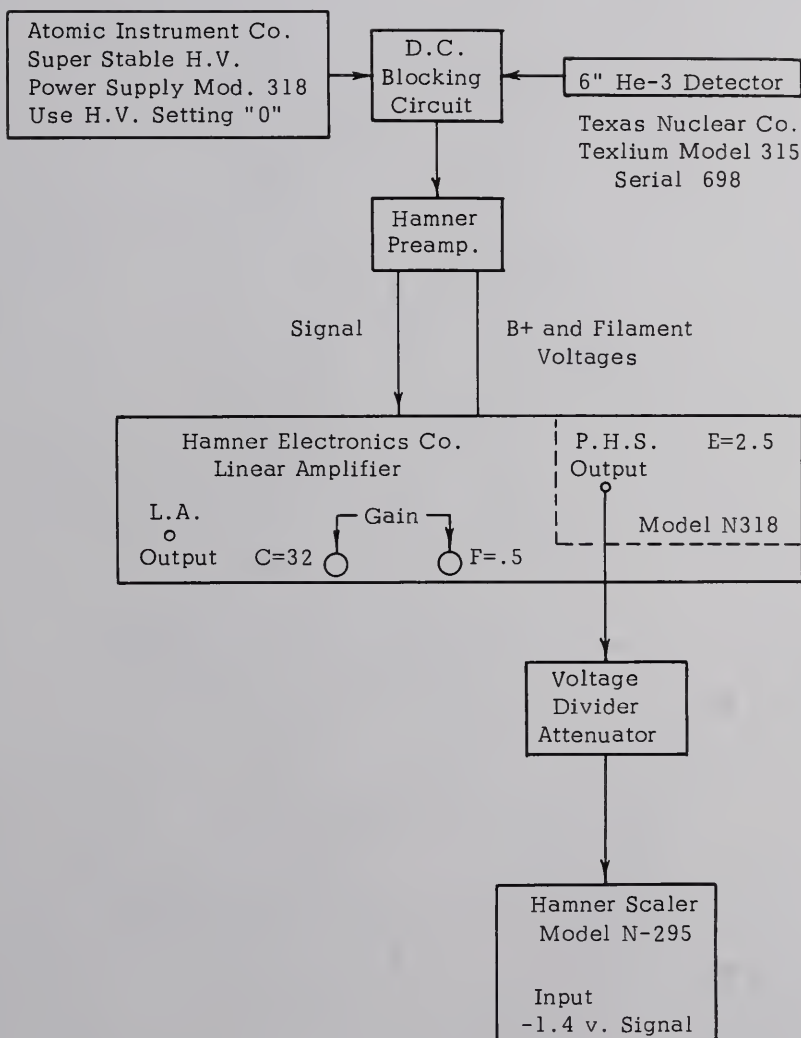
Fig. 4-7.   Diagram of the Reference Detector System.
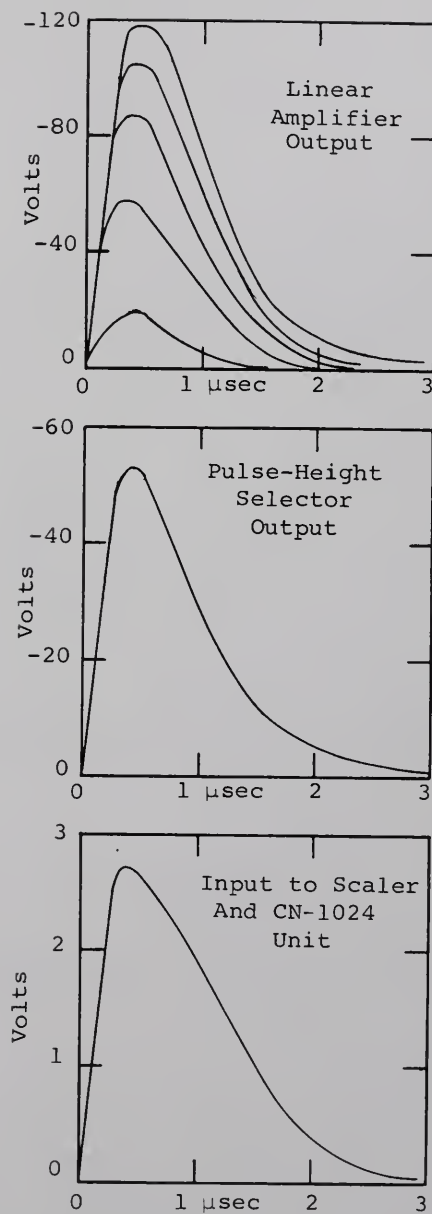
Fig. 4-8. Oscilloscope Display of Signal at Various
Points in the Principal Detector System.
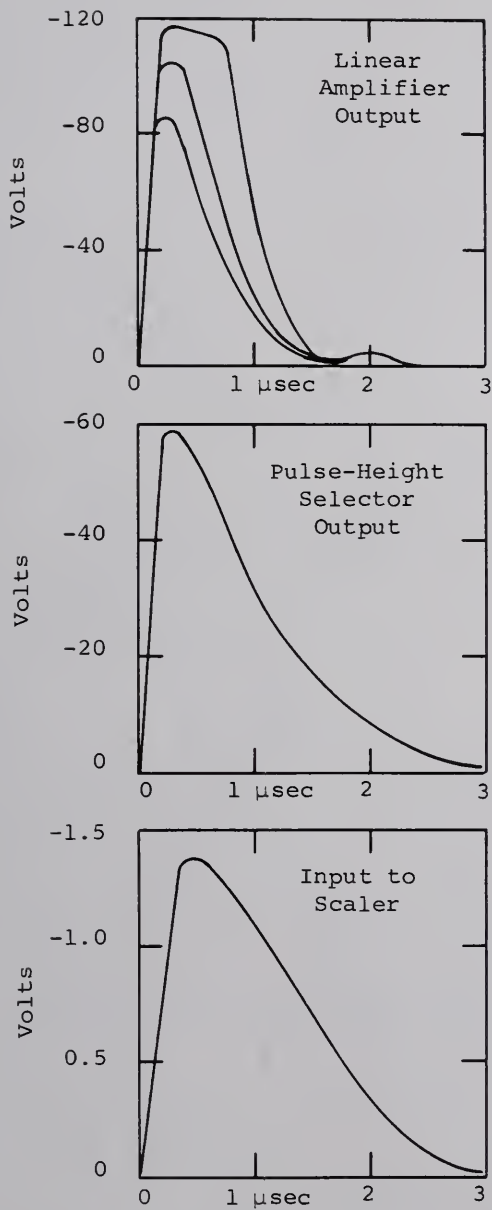
Fig. 4-9. Oscilloscope Display of Signal at Various
Points in the Reference Detector System.
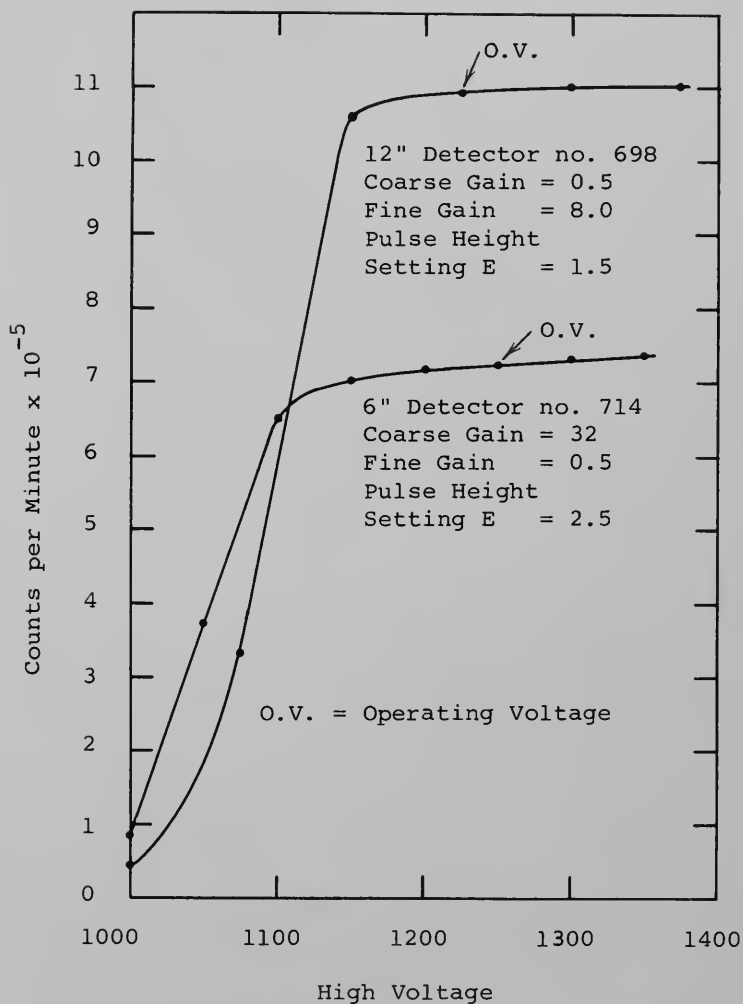
Fig. 4-10.   Plateau Curves for the Principal
            and Reference Detector Systems.

CHAPTER V

EXPERIMENTAL PROCEDURE AND DATA ANALYSIS

A.   Introduction

Throughout the experimental work, the temperature of the moderator was $23 \pm 2°C$, and the purity was 99.5 ± 0.1 per cent D_2O.

For measurements with the loaded assembly, a full lattice of 121 fuel tubes was used, with a moderator depth of 47.8". The same full water level was used during the measurements with the moderator only. Also, when the thermalizing apparatus was used, the H_2O level in the thermalizing tank was maintained at the normal full level of approximately 48".

Certain necessary preliminary measurements related to the construction, adjustment, and performance of the thermalizing apparatus and the detector systems are not described in this chapter, but the results of the more important of these are given in several of the appendices. Tables 5-1 and 5-2 divide the remaining experimental measurements into six major parts. In Parts 1, 2, 5, and 6,

TABLE 5-1

OUTLINE OF EXPERIMENTAL MEASUREMENTS ON D_2O MODERATOR WITHOUT FUEL

Part Number	Neutron Generator Mode of Operation	Detector Position (Axis Studied)	Principal Purposes of Measurement
1	Continuous source, with thermalizing apparatus in use.	A horizontal transverse line near the source boundary. $Y=0$ and $Z=5$ cm.	To study the transverse spatial distribution of neutrons near the source boundary, for comparison with the fundamental spatial mode.
		The Z axis	To find the portion of the tank best suited for measurements, and to determine α for the zero frequency case.
2	Pulsed source, with thermalizing apparatus in use.	A horizontal transverse line near source boundary. $Y=0$, and $Z=5$ cm.	To examine the extent to which the source neutrons constitute a plane wave and to study the transverse spatial distribution of the source neutrons as a function of frequency.
		The Z axis	To determine α and ζ as functions of frequency.
3	Pulsed source, without use of the thermalizing apparatus.	Several positions along the Z axis, near center of tank.	To obtain the neutron pulse decay constant by the conventional pulse die-away method.

TABLE 5-2

OUTLINE OF EXPERIMENTAL MEASUREMENTS WITH LOADED SUBCRITICAL ASSEMBLY

Part Number	Neutron Generator Mode of Operation	Detector Position (Axis Studied)	Principal Purposes Of Measurement
4	Pulsed source, without use of the thermalizing apparatus.	Near the center of the assembly	The decay time constant for the fundamental spatial mode was determined for several different water levels while the loaded assembly was being filled with moderator in order to foresee and avoid accidental criticality during the first loading of the assembly.
5	Continuous source, with thermalizing apparatus in use.	The Z axis	To find the portion of the tank best suited for measurements, and to determine α for the zero frequency case.
6	Pulsed source, with thermalizing apparatus in use.	The Z axis	To determine α and ξ as functions of frequency.

the relative positions of the neutron generator, thermal-
izing apparatus, and subcritical assembly were æ described
in Fig. 4-1 of the previous chapter. Because the behavior
of thermal neutrons was of primary interest, the effect of
the epicadmium neutrons entering the core tank from the
thermalizing apparatus was largely removed from considera-
tion by performing one set of measurements with the cadmium
shutter down (thus permitting only epicadmium neutrons to
enter the core tank), and a second, otherwise identical set
of measurements with the shutter up, permitting both fast and
slow neutrons to enter. After corrections had been applied
to both sets of data for resolution losses, background and
variations in source strength and run times, the shutter-down
counts were subtracted from the shutter-up counts, leaving
counts related to the subcadmium content of the source.

    The reflection of neutrons across the boundary between
the thermalizing apparatus and the assembly has an undesir-
able effect in the experiment, which now will be pointed out.
The experiment is one in which a purely thermal neutron
source is desirable, but since none is available, the thermal-
izing apparatus and cadmium shutter are used to permit a sub-
traction of the effect of the epicadmium content in the
source from the effect of the subcadmium plus epicadmium con-
tent of the source to obtain the effect of only the neutrons

of subcadmium energies. This subtraction may be written:

$$(A + B) - B = A$$

The problem in this is that the two B's are not equal in the actual experiment, because the flux in the assembly caused by epicadmium neutrons entering the assembly from the thermalizing apparatus is greater when the shutter is up than it is for the same source strength of epicadmium neutrons when the shutter is down. This is true because when the shutter is down, it establishes a boundary condition on the thermal neutrons in the assembly, but when it is up, thermal neutrons are free to employ the thermalizing apparatus as a reflector, thus increasing the flux in the assembly, especially in the vicinity of the shutter position. The subtraction of shutter-down counts from shutter-up counts is more accurately represented by the equation,

$$(A + B) - B' = A' \quad \text{or} \quad A' = A + (B - B')$$

Since $B > B'$, as explained above, the subtraction yields an A', which though supposed to be the response of the detector to the subcadmium content of the source with the shutter up, is actually the sum of that quantity plus the difference between the response to the epicadmium content with shutter up minus the response to the epicadmium content with shutter down. Therefore, not all of the detector response to the epicadmium content in the source is

subtracted in the data analysis procedure followed in this work. No real remedy for this problem was found, but by using data from only the middle third of the core tank, when possible, for the determination of α, the error in the results is expected to be small, since the quantity B - B' is small at distances far from the shutter. More will be said about this matter in connection with some of the graphs in the next two chapters.

Corrections for background counts were made in different ways, depending upon whether the assembly had fuel in it or not, and upon the mode of operation of the neutron generator. For the continuous source measurements, the background rate was determined with the neutron generator turned off and was found to be negligible (about 2 to 5 cps) for the unloaded assembly. With fuel, however, the background was a maximum of approximately 5,000 cpm in the center of the assembly as measured with the 12" detector system. Therefore for continuous source measurements on the loaded assembly, the appropriate background rate corresponding to the correct detector position and shutter position was taken from Fig. 7-1 for each run. These corrections were applied to the shutter-up and shutter-down data after the resolution loss corrections were made.

With the generator operated as a pulsed source the situation concerning background was somewhat more complicated because the data were handled by the computer and because the neutron generator was not completely "off" between pulses. During the "off" part of the pulsing sequence, the beam was deflected away from the target, but stray ions caused a few neutrons to be emitted. The "on-off" neutron yield ratio for the generator was sometimes as good as 3000 to 1. This ratio was not constant, and was dependent upon many largely uncontrollable factors associated with the adjustment and condition of the generator and target. With the pulsed source measurements, the MOORE MOMENTS code performed corrections for resolution loss, and variations in source strength first, then subtracted the shutter-down data (which included the background for the shutter-down data) from the shutter-up data plus background. In the subtraction the background tended to cancel out, but some residual error usually remained. As a later step, the code called for the subtraction of a residual background correction which had to be calculated by hand and entered as input information for each detector position.

In practice, it was found that the background in the pulse runs on D_2O was about 10 counts per channel, and the residual background was approximately 2 or 3 counts per

channel in some test data for which it was computed. There-
fore, for the measurements on D_2O without fuel, no correction
was made for the residual background, because of its small
magnitude. With the loaded assembly, however, the raw back-
ground and residual background were of sufficient magnitude
to warrant the full correction procedure. The hand calcu-
lations of the residual corrections were based on the average
channel content of the last 100 channels for both the shutter-
up and shutter-down runs.

Section B, which follows, describes the measurements
in Parts 3 and 4 of the tables, in which some conventional
die-away techniques were performed using a source pulse of
fast neutrons. Parts 1 and 5 pertain to continuous source
experiments along the Z axis, and are described in Section C
of this chapter. Section D describes the measurements in
Parts 2 and 6, which constitute the heart of the experi-
mental work, as these lead to the determination of the
dispersion law and various parameters for the assembly both
with and without uranium.

B.   Conventional Pulse Decay Measurements

For the conventional pulse die-away measurements out-
lined in Parts 3 and 4 of Tables 5-1 and 5-2, the equipment
was arranged to admit during the pulse a large number of
fast neutrons which would become thermalized throughout the
tank, providing a distributed source of thermal neutrons
whose decay would then be studied. For these measurements
the thermalizing apparatus was rolled aside and the target
end of the neutron generator was placed very near the sur-
face of the core tank, at $Z = 0$. The cadmium shutter was
in place, covering the input surface of the core tank.

For Part 3 of Table 5-1, the decay constant for the
heavy water moderator was determined with no fuel present.
Appendix F describes this measurement in greater detail.

In the measurements outlined in Part 4 of Table 5-2,
the decay of the neutron population was observed for several
different moderator levels during the initial filling of
the subcritical with moderator after the full load of fuel
had been loaded into the dry core tank. These measurements
were performed principally for safety reasons during the
initial loading in order to foresee and avoid any possible
criticality accident.

C. Zero Frequency Measurements

Parts 1 and 5 of Tables 5-1 and 5-2 were continuous source measurements performed with moderator only and with the loaded assembly, respectively. Only the experimental procedure will be described here. The graphs and other results from these measurements are given in Chapter VI for the moderator only, and in Chapter VII for the loaded assembly.

For the zero frequency measurements, the neutron generator was operated in the continuous mode (without pulsing) and at a nearly constant beam current while counts were accumulated for a particular detector position. The beam current was increased for detector positions away from the source boundary in order to maintain a satisfactory counting rate from the 12" detector system.

Normally, a counting time of 5 minutes at each detector position was sufficient to accumulate several million counts, making the statistical error in the initial count data approximately 0.1 per cent or less. (Since the resolution error was usually several times this amount, corrections for resolution loss were necessary for both of the detector systems.) The counting time was short enough to permit a set of data to be gathered in a period of several hours or less; a fact which later proved to be especially useful

because these data were found to be largely free of error due to drift in the detector systems, and were used as a basis for a drift correction to the pulse data obtained later over a period of several days. The detector system setup for these measurements was as shown in Figs. 4-6 through 4-10 in Chapter IV. Note, however, that the time analyzer and data output equipment with the 12" detector system were not in use because only integral count data were needed in continuous source measurements. Data recorded included detector position, run time, and scaler counts for both 12" and 6" detector systems for both shutter-up and shutter-down runs. A full list of the column headings on the data and calculation sheets used is given below, along with explanatory remarks.

1. Detector Position.

2. Shutter Position. (Designate up or down.)

3. Neutron Generator Beam Current in μamp. (The beam current used was from 5 to 80 μamp. For Z positions greater than 70 cm, a stronger source would have been useful to increase the count rate of the 12" detector, but would have exceeded a practical limit of 1.5×10^6 cpm for the 6" system monitoring the source strength.)

4. Run Time in Minutes. (Usually 5 minutes for either shutter-up or shutter-down run at each position.)

5. Observed 12" Detector Counts on Scaler. (From 5×10^5 for Z = 125 cm to 6×10^6 cpm. Less for shutter-down runs.)

6.   Observed 12" Detector Count Rate. (Calculated,
      in cpm. Typically approximately 1×10^6, but
      less for large Z and shutter-down runs.)

7.   12" Detector Resolution Correction Factor, 1-F.
      (This is read from a graph prepared for the
      purpose, and is based on the observed count rate.)

8.   Observed 12" Detector Count Rate Divided by 1-F.
      (This gives the resolution-corrected count rate.)

9.   Background Count Rate for 12" Detector. (This was
      determined in a separate measurement, and was very
      small for the moderator only, but quite significant
      in the loaded assembly.)

10.   Resolution-Corrected Count Rate for 12" Detector
      Minus Background. (Background was a function of
      detector position and of the position of the cad-
      mium shutter. This quantity will be referred to
      simply as the corrected 12" count rate.)

11.   Observed 6" Detector Counts on Scaler.

12.   Observed 6" Detector Count Rate. (Calculated, in
      cpm. From 10^5 cpm for low beam current to 1.5×10^6
      cpm at 80 μamp.)

13.   6" Detector Resolution Correction Factor, 1-F.

14.   Observed 6" Detector Count Rate Divided by 1-F.

15.   Background Count Rate for 6" Detector. (This quan-
      tity was always found to be negligible, and is
      listed here only for clarity. The result in item
      14 above will be referred to as the corrected 6"
      detector count rate.)

16.   Corrected 12" Count Rate Divided by Corrected 6"
      Count Rate. (This quantity is in a sense output
      divided by input. Recall that the 6" detection
      monitors the source strength.)

17.   Thermal Flux. (This quantity is found by sub-
         tracting item 16 above for the shutter-down run
         from item 16 for the shutter-up run. For a
         particular detector position, this quantity is
         the corrected and normalized response to sub-
         cadmium neutrons entering the source boundary
         of the core tank. The inverse relaxation length
         for this quantity as a function of Z position is
         the value of α for zero frequency. In Part 1,
         for the transverse flux mapping, this quantity
         is to be compared with the fundamental cosine
         distribution.)

D.   Procedure and Data Analysis for the
     Neutron Wave Propagation Experiments

For Parts 2 and 6 of Tables 5-1 and 5-2, the place-
ment of apparatus was as illustrated in Fig. 4-1 and the
detector systems were as described in Figs. 4-6 through 4-10.
The neutron generator was operated as a pulsed source of the
subcritical assembly after passing through the thermalizing
apparatus.

Binary and digital data from the 1024 channel analyzer
described the time behavior of the pulse as detected at the
position occupied by the 12" detector placed in the sub-
critical assembly. This pulse at each detector position
was Fourier analyzed to yield phase and amplitude informa-
tion as a function of frequency and position. For the Z
axis measurements, this information was further analyzed to
give α and ξ as functions of frequency. Thus, in a sense,

a thermal pulse propagation experiment was used to obtain wave propagation information.

The procedure for the data accumulation and analysis for the wave propagation experiments is outlined in a flow diagram in Fig. 5-1. The complete diagram (on three pages) describes the procedure for the Z axis D_2O measurements of Part 2. All but the last two blocks of the diagram also apply to the analysis of Z axis measurements on the loaded assembly in Part 6. The analysis of the transverse data for the moderator in Part 2 ends with the output from the MOORE MOMENTS code and some hand calculations necessary to put the code output in a form to be graphed. This FORTRAN code is the principal tool in the data analysis. Based on a method suggested by M. N. Moore, and written by R. S. Booth (16), it was used here to perform the Fourier transform of the time analyzer data descriptive of the thermal neutron pulse in order to yield as output the amplitude and phase of frequencies present in the pulse.

A list of column headings on the data and calculation sheets used for the wave propagation experiments is given below, along with explanatory remarks. Some of these quantities were obtained as preliminary information for input into the MOORE MOMENTS code for background and resolution correction of the count data, and for initial plotting of graphs

Fig. 5-1. Flow Diagram for the Data Accumulation and Analysis for the Wave Propagation Experiments.

MOORE MOMENTS code performs Fourier analysis of pulse.

An Extensive Print-out Containing:

Graphs of pulse versus time for each detector position.

Useful for revealing gross features of the pulse, and as an early check for errors in code input or operation.

Tabulated content of 1024 channel analyzer at various stages of correction, subtraction, and normalization.

Leads to graphs showing:
(1) Propagation speed of the pulse,
(2) Spatial flux distribution at chosen times after trigger,
(3) Time-dependent flux at any detector position.

Tabulated amplitude and phase information as functions of position and frequency analyzed. (Same information as on punched data card output.)

Graphs of amplitude versus position and phase versus position for each frequency analyzed may be plotted by hand. These yield good estimates of intercepts and slopes for input into next code, and also help in decision of which data to chop for the linear fits.

Punched Data Cards:

To be used as input to the next code. Cards contain amplitude and phase information for each position and frequency analyzed.

Hand calculation of final correction factors to normalize zero frequency Fourier analysis results to the results of the independent continuous mode experiment. This removes errors caused by day-to-day variations in the electronics.

ALPHA AND XI code (Go to Part 3 of this figure.)

Fig. 5-1. (Continued)

ALPHA AND XI code performs a least squares linear fit for: (1) The logarithm of the amplitude versus Z, yielding the intercept at $Z = 0$, and the slope, α cm^{-1}. (2) The phase angle versus Z, yielding the intercept at $Z = 0$, and the slope, ξ radians/cm. Both fits are made for each frequency analyzed.

α (ω) and ξ (ω) information may be plotted to produce three useful graphs:

ξ (ω) versus α (ω)
α (ω) versus ω
ξ (ω) versus ω

The amplitude and phase at Z=0 as functions of frequency describe the effective source for the experiment.

ω, α (ω), and ξ (ω) serve as input for the ALPHA AND XI COMBINATION code, which computes ω^2, $\alpha^2 - \xi^2$, and $2\alpha\xi$.

Listed output of the same information as on the punched output. Useful for plotting graphs of $2\alpha\xi$ versus ω and of $\alpha^2 - \xi^2$ versus ω^2. Estimates of coefficients needed for the next code may be made from these graphs.

Punched card output of two types: (1) Cards bearing $\alpha^2 - \xi^2$ and ω^2, and (2) Cards bearing $2\alpha\xi$ and ω . These data cards are of correct format for use in the MULTIPLE REGRESSION code, or may be used as a guide for punching the same information in a different format for use as input for the NLLS code.

Continue analysis of data for D2O only:

Either the STEPWISE MULTIPLE REGRESSION code or the UF-NLLS code may be used to perform a least squares, multiparameter fit to determine the $P^{(n)}$ coefficients of the two expansions: $2\alpha\xi = P^{(1)}_{\omega} + P^{(3)}_{\omega}{}^3$ and $\alpha^2 - \xi^2 = P^{(0)} + P^{(2)}_{\omega}{}^2 + P^{(4)}_{\omega}{}^4$.

From the $P^{(n)}$ coefficients, one may calculate the $Q^{(n)}$ coefficients, and D_0, C_0, and F_0 .

Fig. 5-1. (Continued)

to see if the data were worth putting through the Fourier analysis.

1.   Run Identification Number.

2.   Detector Position.

3.   Shutter Position.   (Designate up or down.)

4.   Neutron Generator Beam Current in μamp.   (This is the time-averaged current of deuterium ions received by the target of the Cockcroft Walton accelerator and was recorded principally as a guide during experimentation.   It was not relied upon for use in calculations.)

5.   Run Time.   (Generally the time necessary to complete some chosen number of sweeps of the analyzer.)

6.   TRIG or TRIGC.   (TRIG is the number of triggers or sweeps for the shutter-up run.   TRIGC is the number of triggers for the shutter-down run.   These were usually equal.)

7.   Observed 12" Detector Counts on Scaler.

8.   12" Detector Integral Counts From Analyzer.   (Read from the digital print-out from the analyzer.)

9.   Item 8 Divided by Item 7.   (This was calculated as a running check on the electronics.   Since the resolution times for the scaler and the analyzer were about the same, and since the signal from the linear amplifier and discriminator for the 12" system went to both the scaler and the analyzer, any drift in the value of this constant indicated a drift in the trigger frequency, in the channel width, in the pulse shape or resolution time of the scaler or of the analyzer, or almost any other mal-function of either the scaler or the analyzer and its digital print-out system.)

10.   Background Counts Per Channel. (This quantity was the average counts per channel for the last 100 channels, calculated from the digital print-out. Note that the channel width used must be long enough for the pulse to decay to background in the first 900 channels.)

11.   Observed 6" Detector Counts on Scaler.

12.   Observed 6" Detector Count Rate. (Calculated, in cpm, by dividing total counts by run time. Note that the 6" detector accumulates nearly all its counts in the duration of the target pulse. This count rate therefore is a time-averaged quantity and is far less than the actual count rate during the pulse. See Appendix C.)

13.   Bunching Factor for 6" Detector. (This is that factor by which one must multiply the average count rate in item 12 in order to obtain the effective count rate upon which the resolution correction for the 6" system can be based. See Appendix C.)

14.   Effective Count Rate for 6" Detector. (Item 12 x item 13).

15.   Resolution Correction Factor, 1-F. (Taken from Fig. B-2 in Appendix B for the effective count rate in item 14).

16.   Observed 6" Detector Counts on Scaler Divided by 1-F. (This resolution loss correction was usually less than 2 per cent.)

17.   RATIO. (For input to code. RATIO is item 16 for the shutter-up run divided by item 16 for the shutter-down run.)

18.   CORFAC. (For input to code. CORFAC is the factor
        which takes into account the different source
        strengths used for runs at different Z positions,
        and is item 16 for the shutter-up run at Z = 5 cm
        divided by item 16 for the shutter-up run at the
        detector position for which CORFAC is being calcu-
        lated. Note that 5 cm is the first, or smallest
        Z position at which the detector could be placed.)

19.   12" Detector Integral Counts From Analyzer Divided
        by Observed 6" Detector Scaler Counts. (This is
        item 8 divided by item 11, and is in a sense,
        output divided by input. Although neither quantity
        is corrected for background or resolution loss,
        the logarithm of the quotient may be plotted versus
        detector position to reveal any large errors in the
        integral data prior to performing the Fourier
        analysis.)

20.   Item 19 for the Shutter-up Run Minus Item 19 for the
        Shutter-down Run at the Same Detector Position.
        (Although this quantity contains resolution and
        background errors, the logarithm versus position
        may be plotted to reveal bad data or mistakes prior
        to further analysis. The slope of this graph must
        agree closely with that from the zero frequency
        measurements described earlier.)

        In the analysis procedure outlined above, no provision

has been made for applying an end-effects correction to take

into account the fact that the medium is not of infinite

extent in the Z direction. The possibility of taking end-

effects into account in this work was studied, but it was

concluded that to do so correctly would add considerable com-

plication to the analysis, and, furthermore, no suitable

approximate method was found. It was concluded that, if

possible, the end-effects would be made negligible through

the simple expediency of not using data taken too close to

the end of the tank. Some of the findings concerning the
nature of the end-effects error will now be presented,
however, in the event that some reader may be interested
in tackling the problem. The end-effects correction spoken
of here is that complex quantity (having amplitude and phase)
which one would have to add vectorially to the experimentally
determined Fourier component from the MOORE MOMENTS code for
each detector position and frequency analyzed in order to
obtain the same amplitude and phase at that detector position
and frequency that could be obtained from measurements in a
tank of infinite length. The only case that is easy to
calculate is the zero frequency correction wherein the cor-
rection has the same phase angle as the experimentally
measured quantity. For other frequencies, transcendental
equations are encountered because the correction needed is
a function of the inverse relaxation length, which in turn
is dependent upon the experimental quantity and the correction
term. It was found that the amplitude of the end-effects
correction term at a given distance from the end of the
assembly is a maximum for the zero frequency case, and
decreases with increasing frequency, because the relaxation
length decreases with frequency. Therefore, if the cor-
rection is negligible for the zero frequency case at, say,
55 cm from the end of the tank, the correction is surely

negligible for all other frequencies. This statement is further upheld by the fact that the correction term is usually out of phase with the measured quantity, and this reduces its effect upon the amplitude data. For higher frequencies, the correction sometimes adds, and sometimes subtracts from the measured amplitude, tending to show up as point-scatter rather than as a recognizable, systematic error.

Before data were taken for the wave propagation experiment, it was clear that good results from the Fourier analysis of the thermal pulse would be impossible without the accumulation of a large number of counts. Also it was desirable that the time spent in accumulating counts at a particular detector position with cadmium shutter up or down be less than an hour on the average to permit 40 runs for obtaining shutter-up and shutter-down pulse data at some 20 detector positions in a period of three or four working days, assuming no equipment failures in that interval.

The relationships among run time, counts accumulated, count rates, and resolution errors received further attention. Preliminary measurements showed that a 20 μsec channel counting width and a pulse repetition rate of 25 cps were appropriate settings of the 1024 channel analyzer for studying neutron propagation in the assembly filled with

heavy water without fuel. With this pulse repetition rate, one pulse and one sweep of the analyzer would occur every 40 msec. Therefore, with a 20 μsec channel width, each channel would be open to receive counts only one second out of every 2000 seconds of run time. Furthermore, if from statistical considerations, 30,000 counts is taken to be a reasonable and desirable number to accumulate per channel in the peak of the pulse, one finds that for a count rate of 10^6 cpm in the peak, each channel must be open a total of 1.8 sec during a run, and the run time required would be exactly one hour. To meet the same statistical accuracy with run times shorter than an hour would require short-term counting rates exceeding 10^6 cpm during the pulse peak. Table 5-3 presents information concerning run time, counts accumulated, beam current, pulse width, pulse rates, and channel widths used for the wave propagation experiments.

A calculation of the counts lost because of the finite resolution time of the counting equipment yields an error of 2.83 per cent based on 10^6 cpm and a resolution time of 1.7 μsec per neutron counted. If this error were ignored, it would likely be the largest source of experimental error in the initial data for the wave propagation experiments. If the experimenter does not plan resolution corrections,

TABLE 5-3

EQUIPMENT SETTINGS AND TYPICAL
INTEGRAL COUNT INFORMATION FOR THE WAVE PROPAGATION EXPERIMENTS

Quantity (*Determined for each detector position, and for both shutter-up and shutter-down runs.)	For Moderator Only (Table 5-1, Part 2)	For Loaded Subcritical Assembly (Table 5-2, Part 6)
No. of Triggers *	From 40,000 to 200,000	From 30,000 to 50,000
Beam Current at Target	From 1.5 to 17 µamp	From 1 to 5.3 µamp
Run Time in Minutes *	41.5 for 60,000 triggers	35.2 for 40,000 triggers
Pulse Width (At target)	2 msec	2 msec
Pulse Repetition Rate (Same as triggers per sec)	24.2 cps. (This gives 41.4 msec/trigger.)	19.0 cps. (This gives 52.6 msec/trigger.)
Channel Counting Width (Does not include 10 µsec storage time)	20 µsec	40 µsec
Total Counts Accumulated in 1024 Channels *	From 5 to 11 million for shutter-up runs. From 0.5 to 3 million for shutter-down runs.	From 3 to 6 million for shutter-up runs. From 0.2 to 1 million for shutter-down runs.
Counts in Peak Channel	Usually 30,000 to 40,000	Usually 30,000 to 40,000
Background per Channel	From 1 to 5 counts for shutter up. Less than one for shutter down.	Maximum of 350 counts near the center of the core, with the shutter up.

he should use lower count rates and compromise between sta-
tistical errors and resolution errors.

The effect of uncorrected resolution errors in the
sort of data encountered in this work is worthy of comment.
The fractional error in the counts stored in each channel of
the analyzer is proportional to the instantaneous channel
count rate, and hence proportional to the channel content.
This error would reach a maximum of 2.83 per cent in the
peak channels for the resolution time and count rate assumed
in the above example, but is proportionately less in the
channels describing the rise or the fall of the pulse in
time. Thus the raw data from the analyzer give a distorted,
somewhat flattened picture of the pulse. Without resolution
corrections, the flattened pulse would contain a somewhat
smaller amount of the higher frequency Fourier components
than the true pulse, and this error, being itself a smooth
function of frequency, would probably propagate through all
the ensuing calculations without giving warning through
point-scatter.

The analyzer data require the application of a differ-
ent correction factor for each channel. Such a correction
would be tedious to do with manual calculators, but was
easily built into the MOORE MOMENTS code by R. S. Booth, in
the following manner: For each channel, F was computed first

and then the channel content was divided by 1-F.

$$F = \frac{\text{observed channel counts} \times \tau}{(\text{channel counting width})(\text{number of sweeps})}$$

$$\text{Corrected channel counts} = \frac{\text{observed channel counts}}{1 - F}$$

τ is the resolution time in μsec per observed count. The channel counting width is also expressed in μsec and does not include the 10 μsec that the TMC logic unit uses as storage time between channels. Note that F is the fraction of counting time lost because of finite resolution time, and is proportional to the average count rate during the counting time at each particular channel. The correction is quite simple and straightforward.

The resolution time of the detector system beginning with the 12" detector and ending with the analyzer as shown in Fig. 4-6 was found to be 1.7 ± 0.1 μsec for count rates up to 2.3 x 10^6 cpm. Also the resolution time of that portion of the system in Fig. 4-6 beginning with the 12" detector and ending with the scaler was 1.6 ± 0.1 μsec for count rates up to 2.3 x 10^6 cpm. The resolution time of this second combination of components was needed because count data from this scaler were used during constant source flux

mapping, for which the time analyzer was not needed. For
the monitor detector system in Fig. 4-7, from 6" detector
through scaler, the resolving time was 1.47 ± 0.1 μsec for
observed count rates up to 4.8×10^6 cpm. The method em-
ployed to determine the resolution times mentioned above
is explained in Appendix C.

CHAPTER VI

EXPERIMENTAL RESULTS FOR HEAVY WATER

A. Continuous Source Measurements in Transverse Direction

In this chapter the results of the measurements outlined in Parts 1 and 2 of Table 5-1 in Chapter V are presented. The geometry for the transverse flux measurements is shown in Fig. 6-1, where the 10 detector positions shown lie in the 10 planes described in Chapter IV under "Positioning apparatus for detector." Note that the cadmium shutter was not placed around the detector, or even located at the detector position, but was lowered into the moderator adjacent to the end of the tank, near $Z = 0$.

Graphs of the transverse flux in the core tank along a horizontal line at mid-height and in the plane $Z = 5$ cm are given in Figs. 6-2, 6-3, and 6-4. Figure 6-2 was obtained with the cadmium shutter raised. Figure 6-3 is the shutter-down curve, and Fig. 6-4 presents the difference between the shutter-up and the shutter-down flux. The graphs are normalized to unity at the center line to
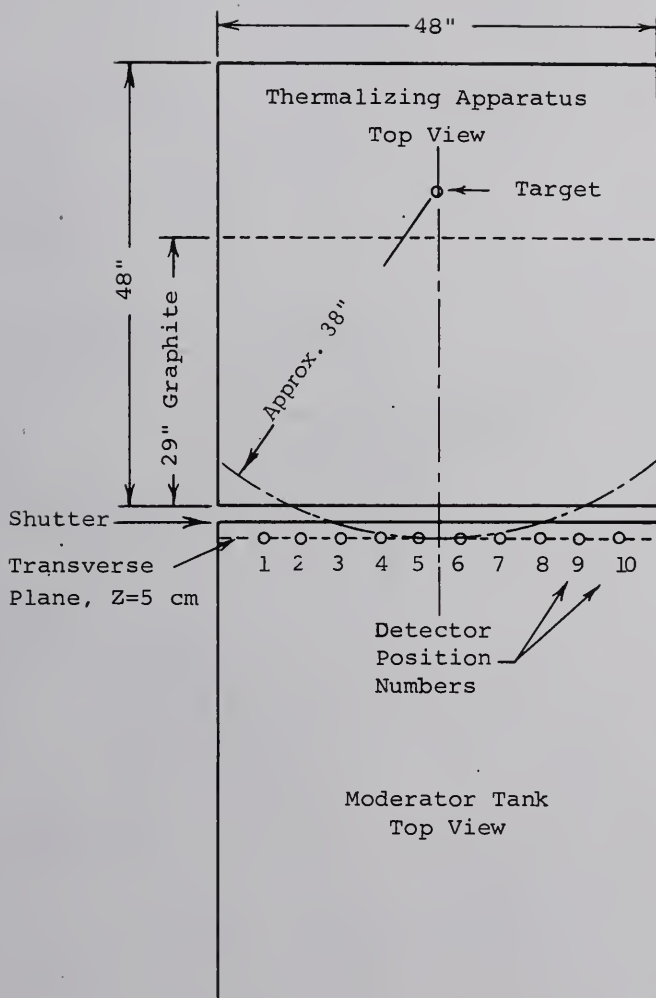
Fig. 6-1. Geometry for Transverse Flux Measurements.
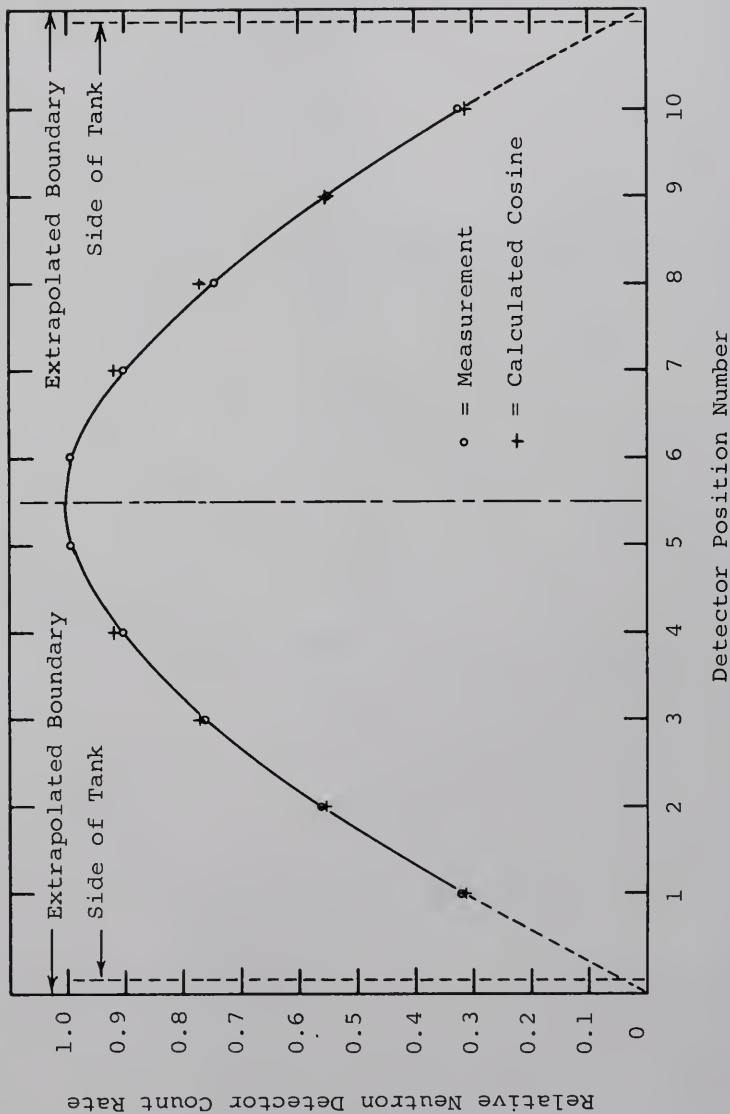
Fig. 6-2. Transverse Flux in Heavy Water at Z = 5 cm Measured with Cadmium Shutter up.
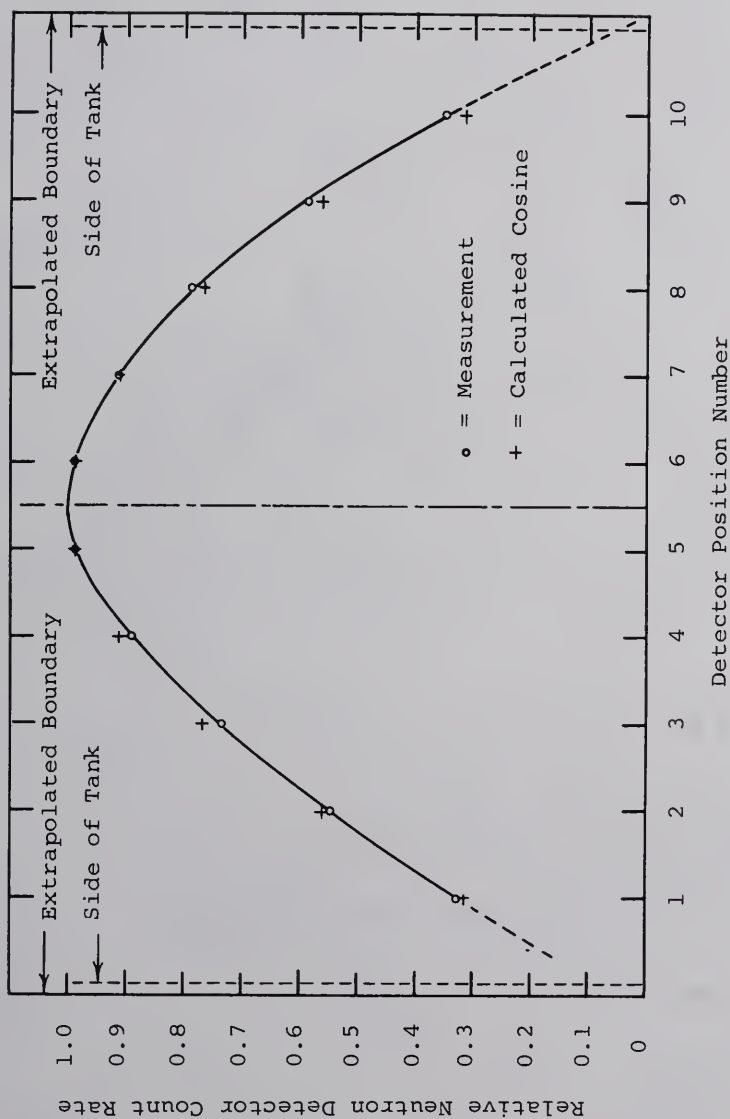
Fig. 6-3. Transverse Flux in Heavy Water at Z = 5 cm
Measured with Cadmium Shutter Down.
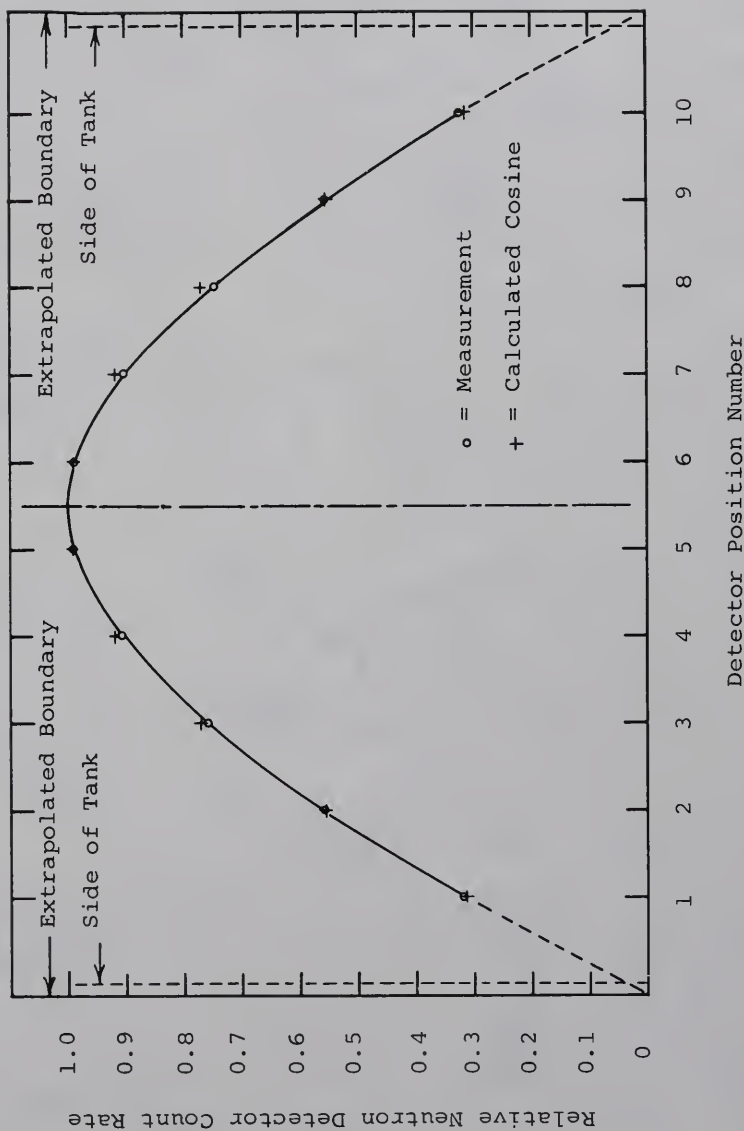
Fig. 6-4. Subtracted Transverse Flux in Heavy Water at Z = 5 cm Obtained by Subtracting Shutter-down Flux from Shutter-up Flux.

facilitate comparison with the cosine shape for the funda-
mental spatial flux distribution. In all three figures,
the spatial distribution is very nearly cosine in shape;
especially so for the shutter-up and difference curves,
which depart from the plotted cosine by 3 per cent or less.
It is clear that the fundamental spatial mode is well estab-
lished especially for the lower energy neutrons, even at
the short distance of 5 cm into the tank.

One finds that the curves here agree more closely
with the cosine shape than do the curves in Appendix A for
the output of the thermalizing apparatus. The explanation
for this difference seems to lie in the fact that for the
measurements in Appendix A, the thermalizing apparatus was
not adjacent to the assembly, and the neutrons were detected
immediately after emerging from the graphite face of the
thermalizing apparatus without further diffusion or reflec-
tion back into the graphite. The situation is quite differ-
ent when the thermalizing apparatus and the subcritical
assembly are placed adjacent to each other. Then neutrons
originating at the target and emerging from the face of the
graphite may diffuse across the boundary between the two a
number of times before being absorbed, leaking out, or being
detected. This additional diffusion causes the spatial dis-
tribution to approach the fundamental mode more closely than
the initial source current from the thermalizing apparatus.

B.   Continuous Source Measurements Along the Z Axis

Figure 6-5 presents the results of the continuous source
(zero frequency) measurements along the Z axis as outlined
in Part 1 of Table 5-1.   (Actually, since fuel occupies the
Z axis, the detector was placed in the plane, $X = 2.175"$, as
explained in Chapter IV.)   The corrected and normalized
detector response is plotted as a function of position for
the measurements with shutter up, and with shutter down.
The difference between these two curves is plotted, and the
ratio of shutter-up results divided by shutter-down results
is also shown in the same figure.   Sufficient counts were
accumulated with both the 12" and 6" detector systems to
maintain a standard deviation of 0.1 per cent or less in
the most important measurements.   The table below gives
additional information concerning the counting errors.

TABLE 6-1

STANDARD DEVIATION FOR FIGURE 6-5

Detector	Standard Deviation of Points Plotted	
Position	For Shutter-up Curve And Difference Curve	For Shutter-Down Curve
5 to 100 cm	0.1%	0.2%
105 to 125 cm	0.2%	0.4%
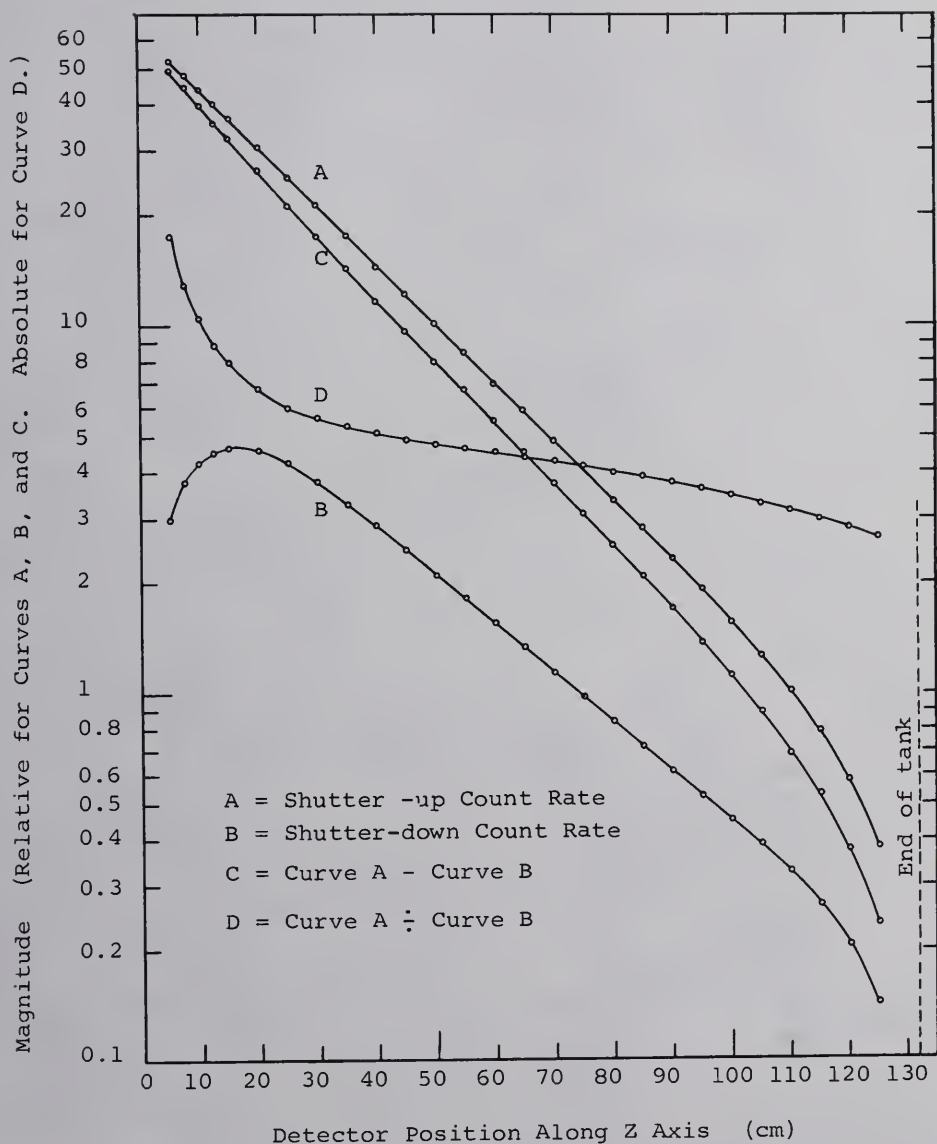
Fig. 6-5. Continuous Source Flux Distribution
in Heavy Water Along the Z Axis.

The peak of the shutter-down curve at 17 cm is due to the thermalization of the epicadmium neutrons, and to the increased sensitivity of the He-3 detector for neutrons of lower energy. After the peak, the slope of this curve becomes remarkably constant from 45 cm to 90 cm. The slope does not approach that of the shutter-up curve. It appears that there is a significant number of epithermal neutrons which travel considerable distances into the moderator before becoming thermalized, thus giving the shutter-up curve a longer relaxation length than that of the subcadmium neutrons. That the slopes of the three flux curves show little if any tendency to approach the same value indicates that the neutron energy distribution even at distances of 90 cm from the shutter remains dependent upon the initial energy distribution permitted to enter the assembly. The downward turn of the three flux curves is an effect of the finite length of the tank.

The slope of the difference curve appears to be constant from approximately 30 cm to approximately 75 cm. The gradually changing slope over the first 30 cm may be explained by the presence of transverse spatial modes in addition to the fundamental, or by the presence of higher energy modes in the end of the tank facing the source. However, the flux maps presented above show so little deviation from the

fundamental spatial mode that the changing slope mentioned must be principally due to higher energy modes. This conclusion is strengthened by the shape of the shutter-down curve, where the slope changes markedly over the first 30 cm. A third effect which may contribute to the nonlinearity of the difference curve is the flaw in the experimental method pointed out in the previous chapter. In the subtraction of the shutter-down curve from the shutter-up curve, the contribution due to epicadmium source neutrons is not fully subtracted, especially for detector positions near the shutter position. This error would result in a difference curve in which the first portion would lie above a straight line drawn tangent to the later portion. Therefore, this error would result in a difference curve resembling the experimental curve, at least in character if not in magnitude. Although the relative magnitudes of the three effects discussed here are difficult to estimate, it seems that the energy mode contamination is the major effect, that the spatial mode contamination is quite small, and that the inherent error in the experimental method is probably in between these two in magnitude. All three disturbances decrease with increasing moderator thickness and seem to be negligible for detector positions 30 cm or more from the shutter.

Since the end-effects become significant at about 50 cm from the other end of the tank, approximately 80 cm of the available 125 cm of tank are not suitable for good determinations of relaxation lengths. Fortunately, this assembly was of such a size as to leave a middle region of about 45 cm suitable for amplitude measurements in D_2O. (That region would be much larger if H_2O were used.) With detector positions spaced 5 cm apart, 10 data points are available in this region. It will be seen later that for the higher frequency Fourier components, the amplitude of the signal was so small that data at 40, 50, 60, or 70 cm from the shutter were not as good as those closer to the shutter. In such cases, data taken closer to the shutter were used in the analysis. It will also be seen later that for phase measurements, the phase shift per centimeter of path was found to be essentially constant over a portion of the tank considerably larger than 45 cm. Hence, if an assembly is large enough for good amplitude measurements, it is surely of sufficient size for phase measurements. One fairly obvious conclusion which may be drawn from the above is that if the assembly had been only 80 cm long, there would have been no middle region suitable for the intended amplitude measurements.

C.   Pulse Propagation in the Transverse Direction

In this section, the results of measurements outlined in Part 2 of Table 5-1 will be presented. The detector placement was along a horizontal line at Z = 5 cm, as shown in Fig. 6-1 for the continuous source transverse measurements in Section A of this chapter. In these measurements, the neutron generator provided a pulsed source and the data were accumulated and Fourier analyzed as described in Chapter V. These pulsed measurements were conducted to study the spatial and temporal distribution of neutrons on a transverse plane near the shutter position in order to view the extent of the deviation from plane wave conditions and to determine the extent of higher spatial mode contamination as a function of frequency content of the source pulse. Both studies are important in that the theory employed assumed a source pulse consisting of only the fundamental spatial mode propagating down the Z axis as a plane wave. It was needful to obtain the information necessary to evaluate the validity of these assumptions. To accomplish this, the output of the MOORE MOMENTS code for the various detector positions was normalized to the same source strength by hand calculations, and two kinds of graphs were produced. The graphs will be presented later.

Comparison with plane wave

The perfect theoretical source needed for this work would be a plane source of dimensions 48" x 48", lying in the XY plane, and having an emission strength per unit area which varies in the shape of the fundamental cosine in both X and Y directions. With such a source, the pulse front would propagate as an XY plane moving down the Z axis, and having the fundamental cosine flux distribution in both X and Y directions. In this theoretical case, therefore, the transverse flux distribution at any time would have the same shape, though not the same magnitude. And in this case, the shape would be that of the fundamental cosine. These are exactly the conditions assumed when one writes the flux as a product of one factor defining a constant transverse cosine shape times other factors carrying the dependence upon Z, time, and frequency.

However, since the target of the neutron generator is only about an inch in diameter, the pulse front and the wave front of each of the Fourier components would travel from the target in a nearly spherical fashion. The wave front passing from the thermalizing apparatus and entering the 48" square end of the heavy water tank would approximate a plane wave front if the solid angle measured at the target and subtended by the end of the tank were reasonably small. In the

experiment, however, this angle can hardly be said to be small, because the thickness of thermalizing materials between the target and the heavy water tank is only about three feet. Therefore, one may expect the wave fronts entering the heavy water to deviate from plane waves by a demonstrable amount. Figure 6-6 presents evidence of this deviation.

Figure 6-6 gives the transverse flux distribution at several different time intervals after the beginning of the target pulse. The data for this figure were essentially the difference between the shutter-up counts and the shutter-down counts in the same channel. The subtraction was performed after appropriate corrections had been made for resolution loss and differences in source strength. In viewing this figure, one may make use of the physical symmetry of the experimental apparatus, and assume that the curves are symmetrical about the center. Each curve is somewhat peaked about the center, especially for short delay times. This peakedness is consistent with the postulated curvature of the traveling pulse front, because of which the pulse reaches the detector positions near the tank center line first. For the higher channel numbers (or longer times after the pulse trigger), the flux shape becomes more nearly like the cosine. This may be explained in part by the fact
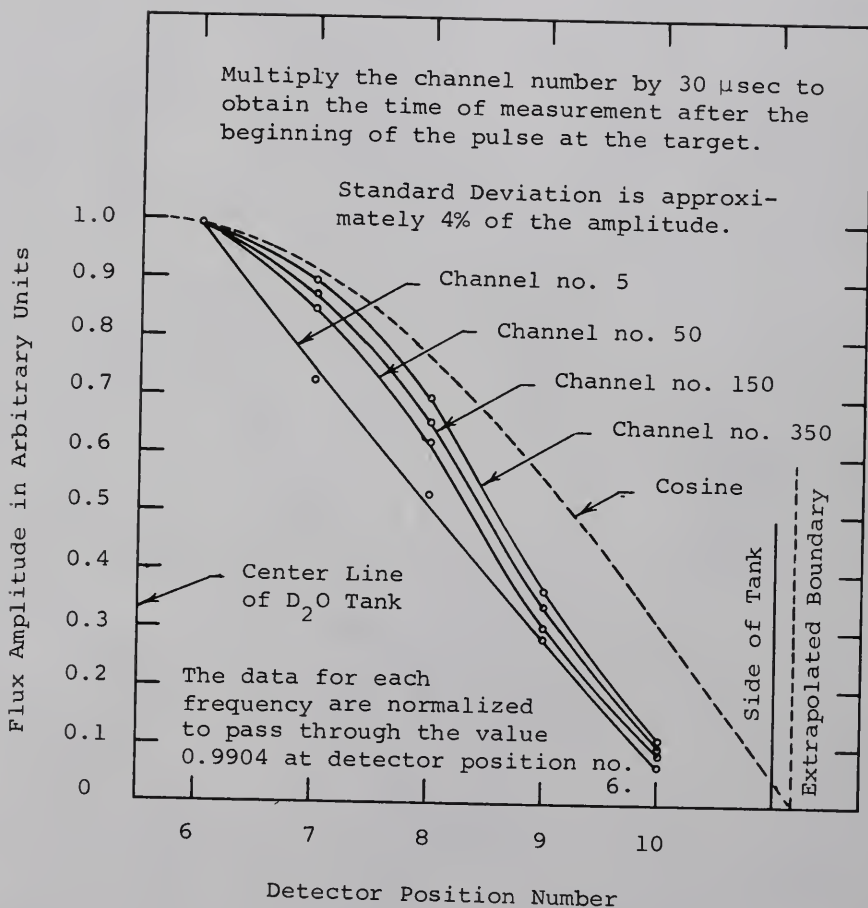
Fig. 6-6. Transverse Flux Distribution at
Various Time Intervals After the
Beginning of the Target Pulse.

that the pulse decays less quickly than it rises. The curves would be more dramatic if the pulse retained the abrupt rise and fall of its original rectangular shape before passing through the thermalizing apparatus. Note that a different scaling factor was used for each curve to cause each to pass through the same magnitude at position 6, for ease of comparison. The deviation from plane wave conditions is evidenced by two features of Figure 6-6: the fact that the transverse flux shape is a function of time, and the fact that each curve is more peaked than the nearly cosine-shaped result obtained from the continuous source transverse measurements.

A cross check between the pulse data and the continuous source measurements was performed by plotting the integral counts from the analyzer for both shutter-up and shutter-down runs (corrected for resolution losses and variation in source strength) in the set of data that yielded Figure 6-6. The integral count curve was very nearly cosine in shape, agreeing well with the continuous source measurements, as it should when the time dependence is integrated out.

The effect that the somewhat nonplanar source pulse is expected to have upon the principal experimental measurements in this work is that the relaxation length would tend to increase as the curved pulse front progresses down the Z axis,

becoming more nearly planar with increasing Z coordinate.
No correction was made for this error, and none is proposed,
but it is reasonable to expect that the departure from plane
geometry is less in that portion of the tank in which the
principal measurements were made than that found on the 5 cm
plane.

Spatial mode contamination as a function of frequency

Figure 6-7 presents the amplitude distribution along
the transverse plane at Z = 5 cm as a function of frequency
for several different Fourier components. (Table 6-2 gives
the same information in greater detail.) These graphs are
therefore transverse flux maps for various frequency values.
They are not, however, flux maps for any particular time
after the pulse trigger, because the content of all 1024
channels of the analyzer entered into the numerical Fourier
analysis, and the entire pulse was taken into account in
the integration. It also follows that the non-planar nature
of the source neutrons is not revealed in the shape of the
graphs because the data are not sensitive to the time of
arrival of the pulse or wave in the detector position. The
amount by which the curve for a particular frequency deviates
from the fundamental cosine is due to higher spatial modes
for that Fourier component as evaluated over the entire pulse;
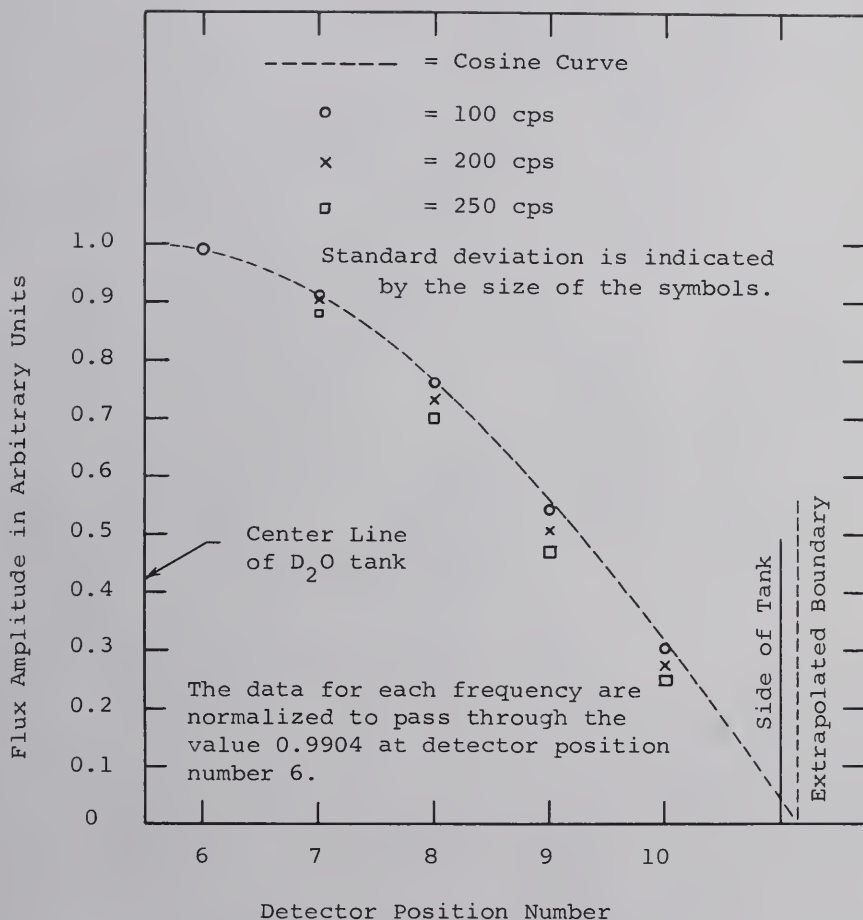
Fig. 6-7. Amplitude of Fourier Components Versus
Detector Position Along a Transverse
Axis for Several Frequencies.

TABLE 6-2

AMPLITUDE VERSUS POSITION IN TRANSVERSE PLANE AT Z = 5 CM FOR CERTAIN FREQUENCIES

Detector Position Number	Angle of Detector Position (degrees)	Cosine of Position Angle	Amplitude of Fourier Component					
			0 cps	50 cps	100 cps	150 cps	200 cps	250 cps
6	7.97	0.9904	0.9904	0.9904	0.9904	0.9904	0.9904	0.9904
7	23.9	0.914	0.919	0.918	0.917	0.913	0.904	0.881
8	39.8	0.768	0.771	0.768	0.762	0.750	0.731	0.701
9	55.8	0.562	0.554	0.550	0.542	0.528	0.505	0.472
10	71.7	0.314	0.313	0.310	0.304	0.294	0.275	0.248

not for some instant in time. The curves are normalized
such that the amplitude of the zero frequency Fourier com-
ponent at each detector position agrees with the continuous
source measurements at the corresponding detector positions.
The amplitude distribution is peaked about the center line,
departing from the fundamental cosine shape in progressively
larger amounts as the frequency increases. This result was
expected, and can be explained as follows. Consider first
the geometry of the detector and source. Since detector
positions 6, 7, 8, 9, and 10 are not equidistant from the
target, the neutrons that are detected at position 10, for
example, have diffused further on the average than those
which are detected at position 6. There is some average
frequency-dependent attenuation factor associated with
traveling that extra distance, and this attenuation fac-
tor increases with frequency, as will be seen in Section D
to follow. Therefore, when the curves for various fre-
quencies are normalized to the same magnitude at position
6, one finds that the amplitude at detector positions away
from the center line drops off by increasingly larger amounts
as the frequency increases, producing the peaked shape, and
revealing a higher mode content that increases with in-
creasing frequency.

From the above results, one would expect the shape of

the pulse seen by the detector to become wider (in time) as the detector is moved from position 6 toward position 10. Such is the case. Graphs of the normalized output of the analyzer for several detector positions were plotted, and a progressive widening was observed to take place as the distance from the tank center line increased. It is un-desirable, of course, for there to be any difference in the pulse shape as detected along a transverse path, but since this widening is present, it is of interest to evaluate its severity. A useful way to do so is to compare the widening of the pulse as one moves transversely, with the widening that is seen as one moves the detector down the Z axis. It was found from such a comparison that the pulse shape and width seen at position 10 in the $Z = 5$ cm plane is slightly narrower than that observed with the detector in position 6 in the $Z = 10$ cm plane. In other words, the undesirable distortion of the pulse shape which is seen as one moves the detector transversely from near the center line of the tank to a position near the side wall of the tank (a distance of approximately 44.2 cm) is approximately equivalent to the change in shape which accompanies only 4 cm of travel down the Z axis. (Note that a broadening of the pulse with in-creasing Z coordinate is desirable, as without such, we could not observe the dispersion law.) If the same study were

made of the pulse shapes on a transverse plane at, say, Z = 50 cm, one would probably see less distortion than this, since the Z = 5 cm plane is much nearer the source plane.

One may conclude from these results that plane wave conditions are very nearly obtained, and that the plane wave approximation should introduce only negligible errors, especially if the measurements are performed near the center line of the tank.

D. Pulse Propagation Measurements Along the Z Axis

At the outset, the reader is reminded that the measurements "along the Z axis" were actually made in a plane parallel to the Z axis and approximately 2.175" from it, for reasons given in Chapter IV. These measurements were made in detector position row number 6, as illustrated in Fig. 6-1 in Section A above. The offset is not harmful to the results, and was a matter of necessity when the assembly was fueled; and a convenience when unloaded.

The results to be presented here came from measurements outlined in the second half of Part 2 in Table 5-1. The data analysis was conducted in accordance with the flow diagrams in Fig. 5-1.

Figures 6-8, 6-9, and 6-10 show the shapes of the shutter-up, shutter-down, and difference pulses as seen at
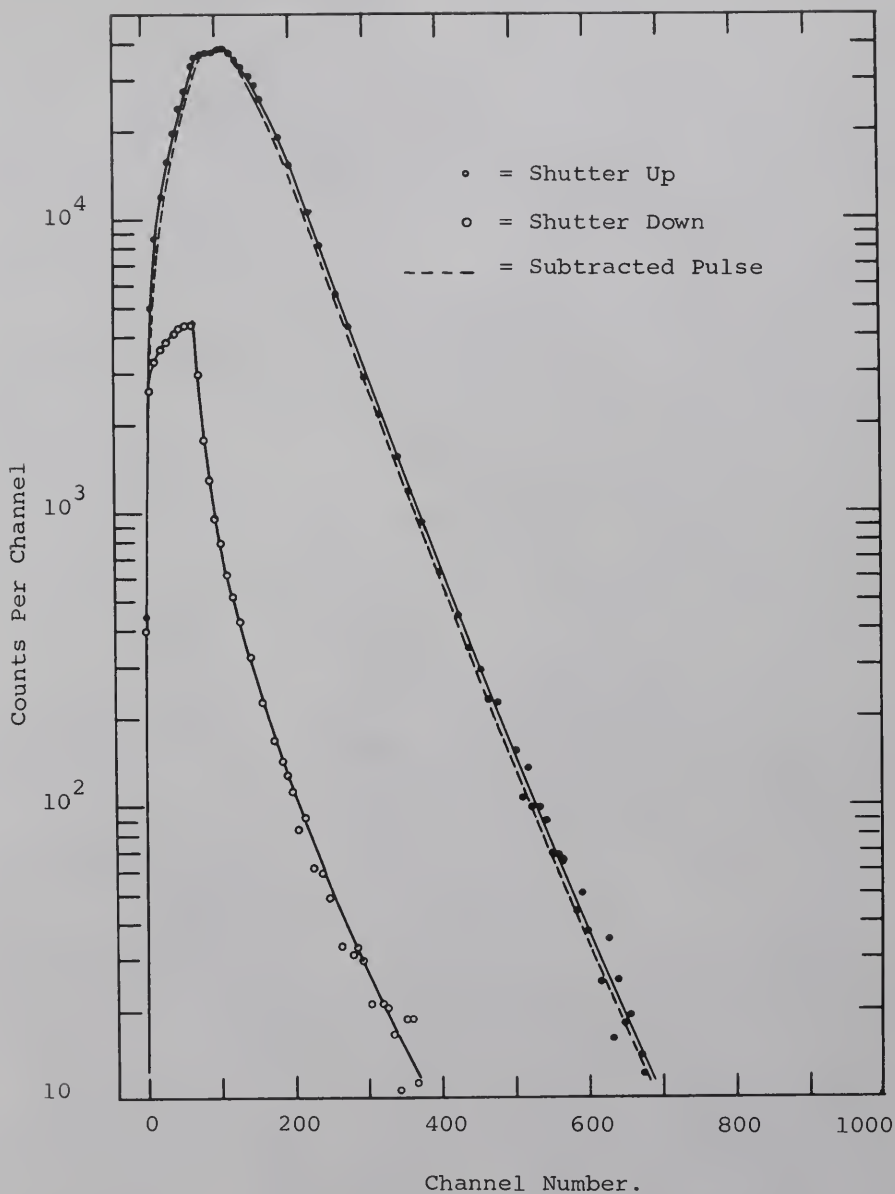
Fig. 6-8. Shutter-up, Shutter-down, and Subtracted Pulse
Versus Time in Heavy Water at Z = 5 cm.
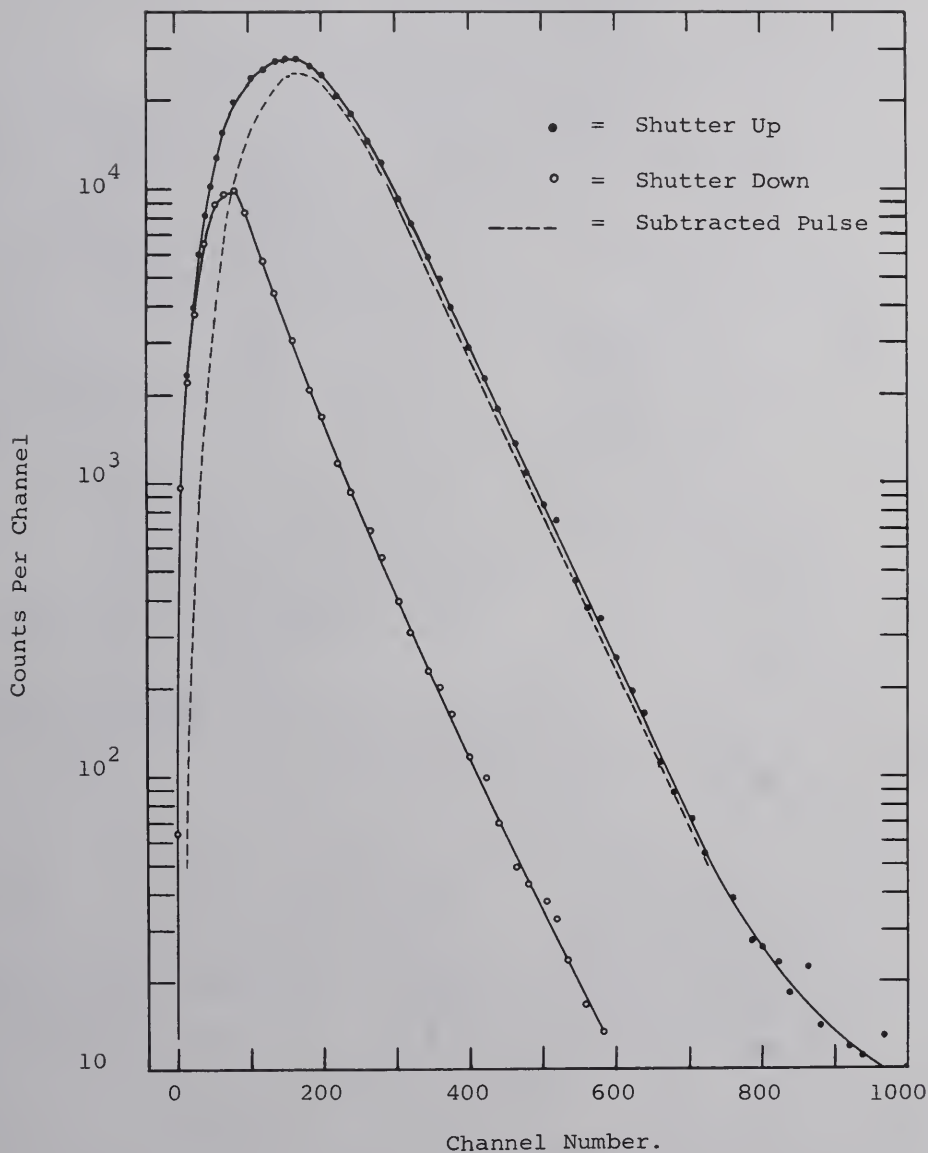
Fig. 6-9.   Shutter-up, Shutter-down, and Subtracted Pulse
            Versus Time in Heavy Water at Z = 40 cm.
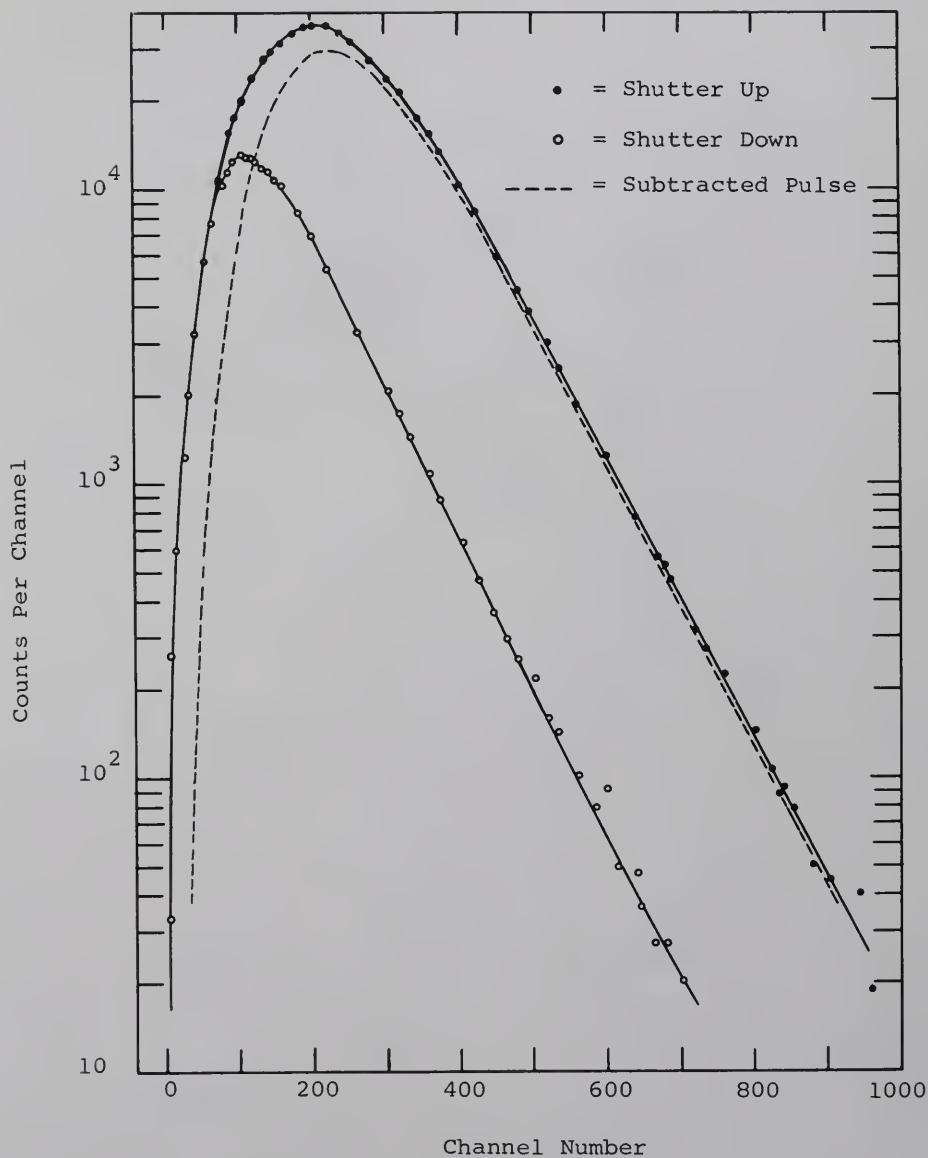
Fig. 6-10.   Shutter-up, Shutter-down, and Subtracted Pulse
Versus Time in Heavy Water at Z = 70 cm.

three different detector positions along the Z axis. and as
plotted from the analyzer data after corrections for reso-
lution loss and variations in source strength had been made.

Figure 6-11 shows the shape of the difference pulse
at several detector positions along the Z axis. These
graphs are normalized to 30,000 counts in the peak channels
to facilitate a comparison of the shapes. Note that the
width of the pulse and the delay of the peak both increase
with distance along the axis. In the Fourier analysis of the
pulse, this delay and the dispersion give rise to frequency-
dependent quantities describing the phase shift and the
amplitude attenuation of waves traveling down the Z axis.

Another interesting feature of Fig. 6-11 is that it
shows a different decay rate for each detector position.
The pulse decays more slowly as the detector is moved
further down the Z axis. (This is true at least for Z
values of 70 cm or less. It appears that the decay con-
stant at 90 cm is approximately equal to that at 70 cm.
Analyzer data were not taken beyond the 90 cm position.)
One reason for this dependency upon position is that al-
though the fundamental transverse spatial mode in the source
neutrons entering the end of the tank is well established
from the outset, the fundamental flux distribution along
the length of the tank is much slower in being established;
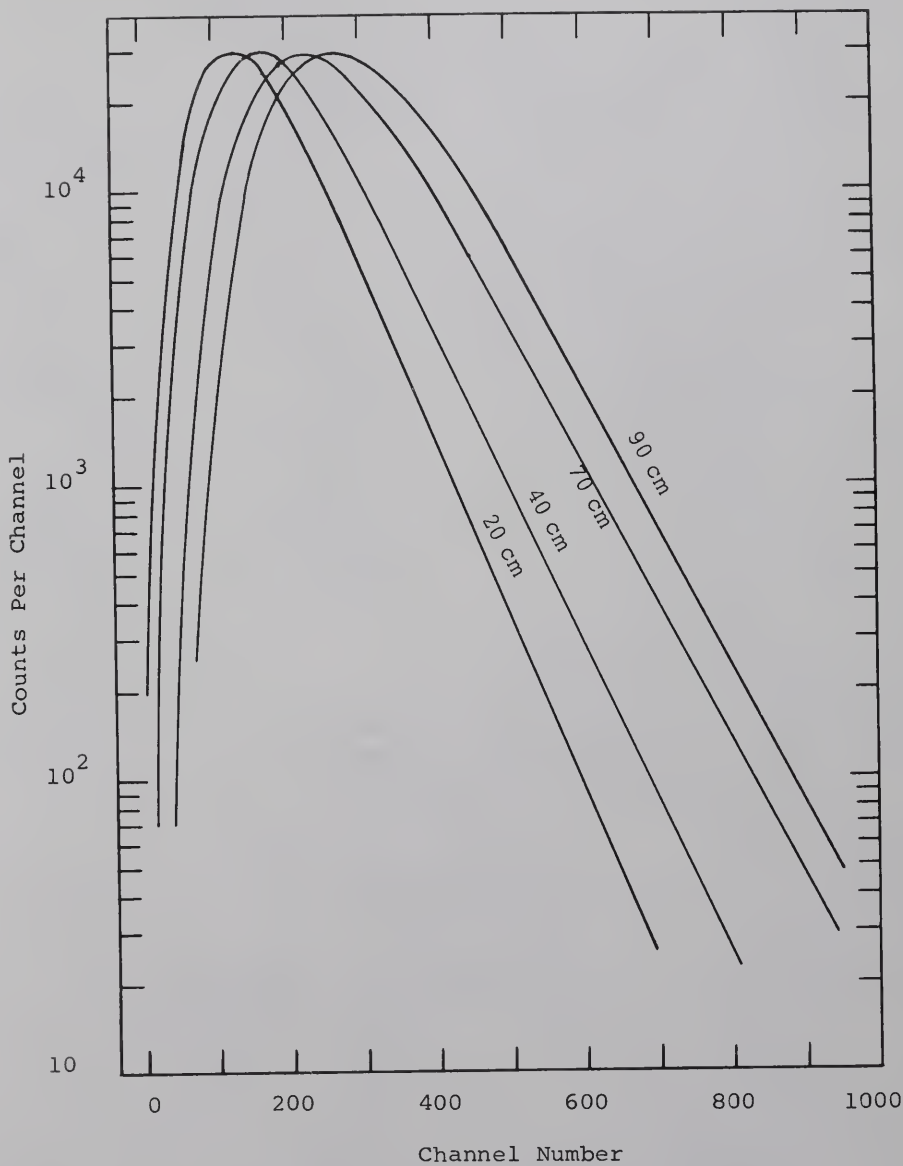
Fig. 6-11. Normalized Subtracted Pulse Versus Time at
Several Detector Positions Along the Z Axis.

especially so because of the size of the medium, and the
use of a thermal source at a boundary of the tank. These
findings are not new to those who are familiar with con-
ventional pulsing techniques, in which a fast neutron
source is used to minimize the problems touched on above,
but perhaps the quantitative findings are of interest. If
one assumes that the time required for the axial fundamental
mode to be established is several times the length of time
required for the thermal pulse to travel the length of the
assembly, one finds that at least 20 or 30 msec is required.
(With a propagation speed of 177 m/sec, obtained later in
this section, the pulse requires over 7 msec to travel down
the length of the tank.) Since the pulse as observed near
the middle of the tank decays a decade in approximately 6
msec, one finds that 4 or 5 decades or more of amplitude
would be lost before the fundamental mode would be adequately
established for decay measurements to begin. In Fig. 6-11,
there is little observable tendency for the decay slopes
to reach a common value in over two decades of decay. No
use is made of the decay time constants in this work.

The width of each pulse in Fig. 6-11 after the ampli-
tude has fallen to 10 per cent and to 1 per cent of the peak
value is plotted as two curves in Fig. 6-12. These curves
extrapolate to values of 8 and 13 msec, respectively, giving
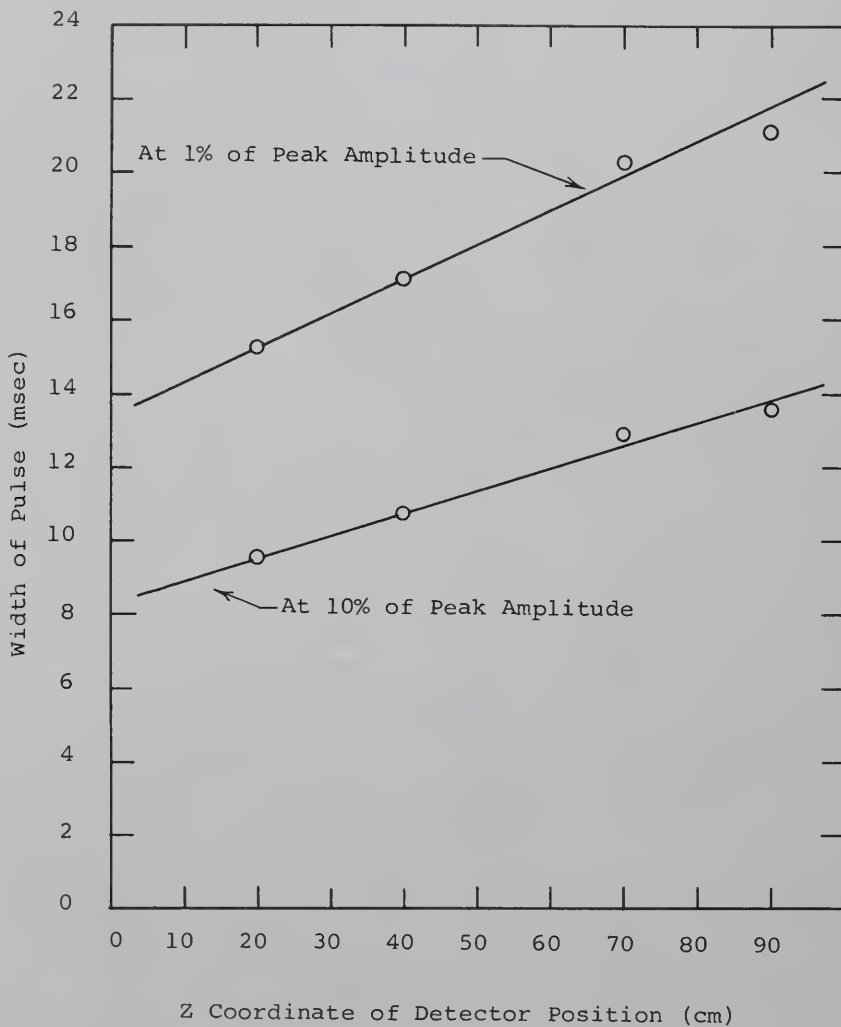
Fig. 6-12. Width of the Subtracted Pulse at 10 per
cent and 1 per cent of the Peak Value as
a Function of Z Position in Heavy Water.

an estimate of the width of the source pulse at the position
Z = 0. Comparing these results with the 2 msec pulse width
at the target, one might conclude that the thermalizing appa-
ratus has a marked dispersive effect upon the pulse. That
the thermalizing apparatus does broaden the pulse is doubt-
lessly true, but it would not be accurate to attribute all
the broadening of the pulse as seen at Z = 0 to the size,
geometry, or materials making up the thermalizing apparatus,
nor solely to the collision events that took place in the
thermalizing apparatus before the neutron made its first
trip across the graphite-D_2O boundary. One comes to think
of the pulse at Z = 0 as having come from the thermalizing
apparatus. But this is approximately half true, since the
presence of the D_2O adjacent to the thermalizing apparatus
acts as a reflector of high efficiency. From albedo con-
siderations, almost half of the thermal neutrons one detects
at Z = 0 have made their last collision in the D_2O, not in
the graphite. Furthermore, from albedo considerations, one
finds that the average neutron detected at Z = 0 has crossed
the boundary between the thermalizing apparatus and the D_2O
tank a number of times. In view of this, one may state that
even with a perfect thermalizing apparatus--one which could
deliver an output thermal pulse with exactly the same shape
and width as the target burst--once this apparatus is placed

adjacent to a tank of D_2O, the true or effective source
pulse for the experiment as defined by a detector at the
interface would have a new shape and a greater width than
that of the target burst.

The time required for the pulse peak to reach various
detector positions is shown in greater detail in Fig. 6-13,
which gives graphs of the channel number in which the pulse
peak occurs for each detector position along the Z axis.[1]
Since the channel number can be converted to time by multi-
plying by 30 μsec/channel, the inverse of the slope of the
curves in Fig. 6-13 gives the velocity of the pulse peaks.
For the difference curve, the velocity is nearly constant.
(The velocity should be constant if the pulse is traveling
as a plane wave, with the fundamental spatial distribution,
and with a constant energy distribution. All three of these
conditions are very nearly met.)

By extrapolating this curve back to zero cm, the peak
is found to pass through the thermalizing apparatus 2.88

---

[1] The point-scatter in this graph is largely due to the
fact that an abbreviated output from the MOORE MOMENTS code
was used in these runs, with a print-out of the corrected
and subtracted analyzer data for only every eighth channel.
Hence, the location of the pulse peaks involved judgment
based on the shape of the peak as described by the available
information in the vicinity of the peak. The abbreviated
output was elected in order to reduce the volume and time of
a complete print-out for all 1024 channels.
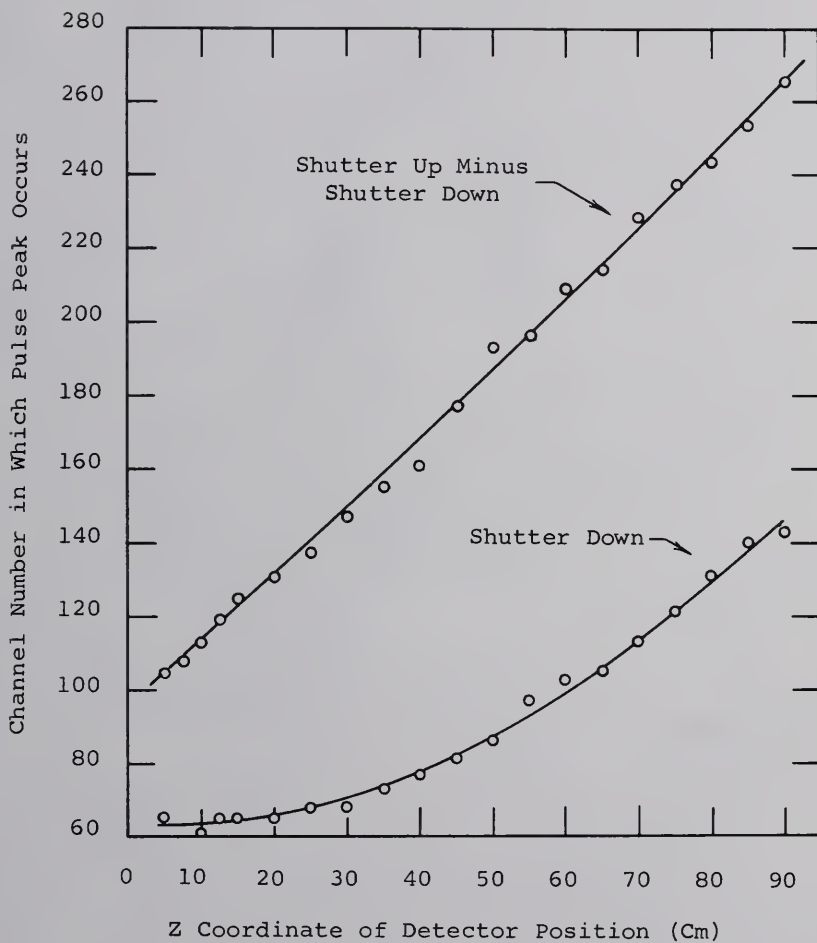
Fig. 6-13. Propagation of the Pulse Peak
in Heavy Water.

msec or 96 channel widths after the trigger of the target
pulse. Assuming that the peak corresponds approximately to
the middle of the original 2 msec pulse, the time required
to pass through the thermalizing apparatus is approximately
1.9 msec. Once in the heavy water, the peak required 4.8
msec to travel 85 cm, giving an average speed of 177 m/sec.
The temperature was approximately 23° C. It is of interest
to note that 177 is only 8 per cent of 2200 m/sec.

The shutter-down curve is not at all linear. It is
practically constant for about 20 or 30 cm into the heavy
water. This may be understood in view of the fact that with
the cadmium shutter down, and for detector positions not too
far from the cadmium, the detector response is principally
to epicadmium neutrons. On the oscilloscope display of
the analyzer memory, one could see a sharp peak which fell
rapidly at a time corresponding almost exactly to the end
of the target pulse. Although the initial delay of the
shutter-down curve appears to be 63 channels, or 1.89 msec,
note that this peak corresponds to the cut-off of the
nominal 2 msec target pulse. For greater distances from
the shutter, the detector response continues to increase
even after the cut-off of the target pulse, the peak becomes
more rounded, and the fall is delayed and not so sharp. For
detector positions exceeding 30 or 40 cm, a significant

amount of thermalization occurs, and the pulse begins to move more slowly. The slope of the shutter-down curve increases with increasing moderator thickness, but remains significantly less than that of the difference curve, even at the 90 cm position. The dependence upon the initial energy distribution is again quite evident, as it was with Fig. 6-5, given earlier with the continuous source results.

Since the propagation of the shutter-down pulse is so strongly dependent upon thermalization effects, it suggests that a careful study of this pulse as a function of position and frequency could yield information on the slowing-down process in heavy water. In the present study, however, attention is given to thermal neutron behavior.

Figure 6-14 shows the relative amplitude of the Fourier components of the pulse as a function of frequency for three different detector positions. This graph may be regarded as the signal strength in relative units per unit frequency plotted as a function of frequency.

The analysis was performed for 50 different frequencies in the range from 0 to 500 cps, in steps of 2 cps from 0 to 10 cps, and in steps of 10 cps from 10 to 500 cps. The numerical Fourier analysis method was capable of handling an amplitude range of 3 decades in D_2O before the statistical error in the analyzer data became too large relative to the
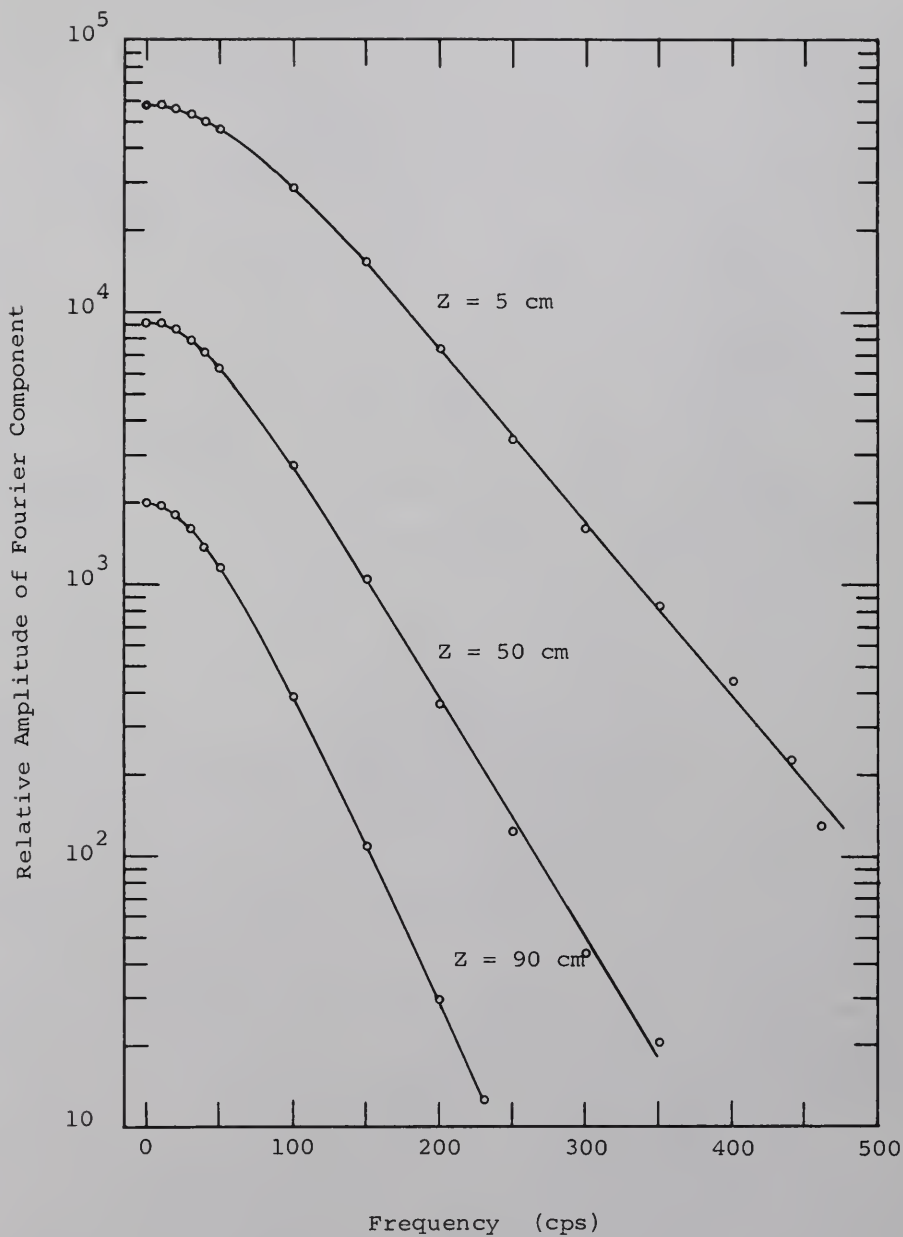
Fig. 6-14. Amplitude of Fourier Components of the Subtracted
Pulse Versus Frequency for Several Positions.

amplitude of the signal. The amplitude results from the analysis appear to be useful up to 490 cps for the 5 cm position, up to 400 cps for the 50 cm position, and up to 350 cps for the 90 cm position. However, further analysis of the data will reveal that the frequency ranges over which truly useful results were obtained are narrower than these by about 100 cps.

Of course, since the statistical error in the results from the Fourier analysis is dependent upon the number of counts accumulated to describe the pulse, one could increase the sensitivity of the method and extend the frequency range somewhat by accumulating more count data. For these measurements in D_2O, from 4 to 12 million counts were accumulated by the analyzer for the shutter-up run at each detector position. Further comments on how the experiment might be improved are presented in Chapter IX.

Figure 6-15 is a plot of the logarithm of the amplitude of the Fourier components as a function of detector position for several frequencies. (Sufficient information was obtained for plotting such graphs for 50 different frequencies, but only 8 are shown here to illustrate the results.) Note that the amplitude falls somewhat more quickly in the first 25 cm of the tank than it does in the central portion. This same effect was observed for the
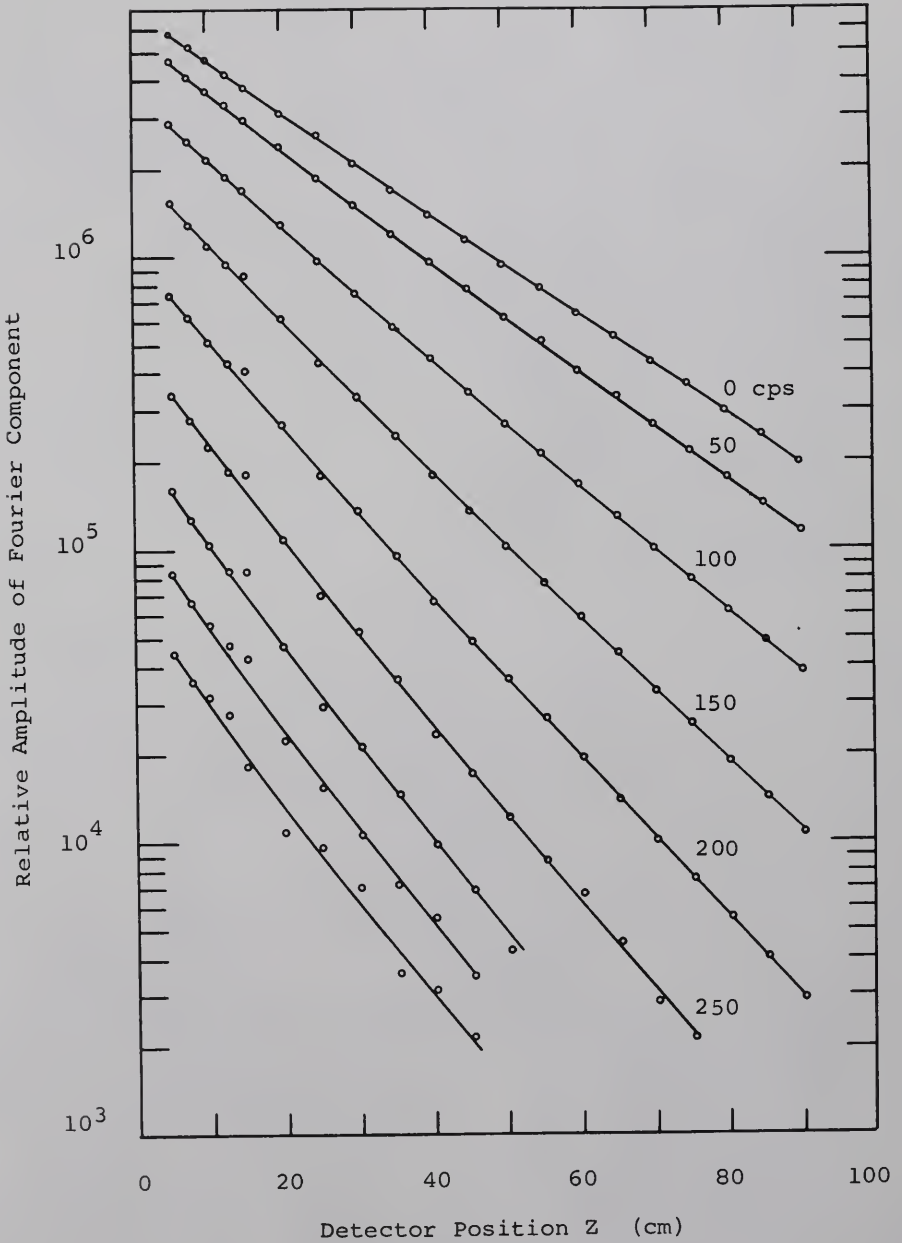
Fig. 6-15. Amplitude of Fourier Components of the Subtracted Pulse Versus Position for Several Frequencies.

continuous source results presented earlier.

The phase angle versus position for a number of fre-
quencies is shown in Fig. 6-16. These graphs show almost no
variation in slope over the full range of detector positions.

The ALPHA AND XI code was used to obtain linear least
squares fits of the logarithm of the amplitude for each fre-
quency as a function of position, and of the phase angle for
each frequency as a function of position, to obtain the real
and imaginary parts, respectively, of the inverse relaxation
length as functions of frequency. The resulting values of
α and ξ and other quantities of interest are given in Tables
6-3 and 6-4. Notice in Table 6-3 that the least squares fit
was performed twice on the amplitude data; once including
data from the portion of the tank close to the source, and
later with the first 4 data points omitted except as noted.
(A careful examination of detailed graphs of the amplitude
data showed that the first 4 data points should be dropped
because the slopes of the graphs did not become constant
until after about 25 cm of penetration into the heavy water.)
The fit to the reduced data yielded values for α which are
smaller than the values based on the larger range of detector
positions, as would be expected from inspection of the curves
in Fig. 6-15. The systematic difference in the results of
the two computations is a maximum of approximately 3 per cent
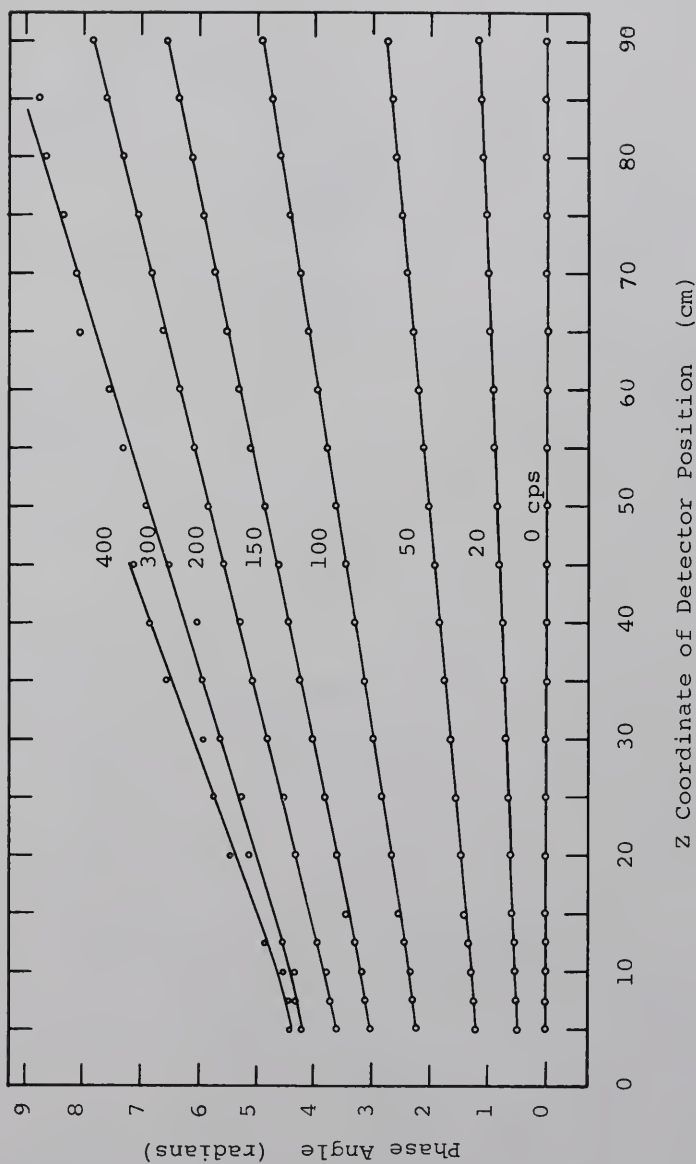
Fig. 6-16. Phase Angle of Fourier Components Versus
Position for Several Frequencies in Heavy Water.

TABLE 6-3

EXPERIMENTAL VALUES OF α IN D_2O AS A FUNCTION OF FREQUENCY

Frequency of Fourier Component (cps)	First Least Squares Determination			Second Least Squares Determination		
	Range of Data Points Used (cm)	Amplitude at Z=0 cm	α (cm^{-1})	Range of Data Points Used (cm)	Amplitude at Z=0 cm	α (cm^{-1})
0	5 – 75	8.8298	0.03961	25 – 75	8.7690	0.03853
2	5 – 75	8.8295	0.03962	25 – 75	8.7686	0.03854
4	5 – 75	8.8284	0.03965	25 – 75	8.7675	0.03856
6	5 – 75	8.8265	0.03969	25 – 75	8.7656	0.03860
8	5 – 75	8.8240	0.03974	25 – 75	8.7630	0.03865
10	5 – 75	8.821	0.0398	25 – 75	8.760	0.0387
20	5 – 75	8.794	0.0404	25 – 75	8.733	0.0393
30	5 – 75	8.753	0.0413	25 – 75	8.690	0.0402
40	5 – 75	8.697	0.0424	25 – 75	8.635	0.0413
50	5 – 75	8.631	0.0437	25 – 75	8.568	0.0426
60	5 – 75	8.554	0.0451	25 – 75	8.492	0.0440
70	5 – 75	8.469	0.0466	25 – 75	8.407	0.0455
80	5 – 75	8.377	0.0481	25 – 75	8.315	0.0470
90	5 – 75	8.277	0.0496	25 – 75	8.216	0.0485
100	5 – 75	8.171	0.0511	25 – 75	8.110	0.0500

TABLE 6-3 (Continued)

Frequency of Fourier Component (cps)	First Least Squares Determination			Second Least Squares Determination		
	Range of Data Points Used (cm)	Amplitude at Z=0 cm	α (cm^{-1})	Range of Data Points Used	Amplitude at Z=0	α (cm^{-1})
110	5 - 75	8.06	0.0525	25 - 75	7.99	0.0513
120	5 - 75	7.95	0.0541	25 - 75	7.88	0.0529
130	5 - 75	7.82	0.0555	25 - 75	7.76	0.0544
140	5 - 75	7.70	0.0570	25 - 75	7.63	0.0558
150	5 - 75	7.57	0.0584	25 - 75	7.50	0.0572
160	5 - 75	7.44	0.0599	25 - 75	7.37	0.0586
170	5 - 75	7.30	0.0613	25 - 75	7.23	0.0599
180	5 - 75	7.17	0.0627	25 - 75	7.10	0.0614
190	5 - 75	7.03	0.0641	25 - 75	6.95	0.0628
200	5 - 75	6.88	0.0655	25 - 75	6.80	0.0641
210	5 - 75	6.73	0.0668	25 - 75	6.65	0.0653
220	5 - 75	6.58	0.0682	25 - 75	6.50	0.0666
230	5 - 75	6.43	0.0695	25 - 75	6.34	0.0680
240	5 - 75	6.28	0.0707	25 - 75	6.18	0.0690
250	5 - 75	6.13	0.0719	25 - 75	6.03	0.0701

TABLE 6-3 (Continued)

Frequency of Fourier Component (cps)	First Least Squares Determination			Second Least Squares Determination		
	Range of Data Points Used (cm)	Amplitude at Z=0	α (cm^{-1})	Range of Data Points Used (cm)	Amplitude at Z=0 cm	α (cm^{-1})
260	5 – 75	5.98	0.0730	25 – 75	5.00	0.0714
270	5 – 75	5.82	0.0738	25 – 75	5.73	0.0721
280	5 – 75	5.67	0.0747	25 – 75	5.58	0.0730
290	5 – 75	5.54	0.0761	25 – 75	5.47	0.0749
300	5 – 75	5.41	0.0775	25 – 75	5.37	0.0766
310	5 – 70	5.30	0.0788	25 – 70	5.28	0.0785
320	5 – 70	5.19	0.0804	25 – 70	5.21	0.0808
330	5 – 65	5.05	0.0805	25 – 65	5.05	0.0803
340	5 – 65	4.94	0.0811	25 – 65	4.95	0.0812
350	5 – 60	4.84	0.0819	25 – 60	4.89	0.0829
360	5 – 55	4.76	0.0838			
370	5 – 50	4.64	0.0829			
380	5 – 45	4.43	0.0772			
390	5 – 40	4.30	0.0766			
400	5 – 40	4.19	0.0781			

Note: In the range from 360 to 400 cps, no determination of α was performed with omission of data near the source boundary.

TABLE 6-4

EXPERIMENTAL VALUES OF ξ
IN D_2O AS A FUNCTION OF FREQUENCY

Frequency of Fourier Component	Range of Data Points Used (cm)	Phase at $Z=0$ cm (Radians)	ξ (Rad cm^{-1})
0	5 - 90	0	0
2	5 - 90	0.04715	0.0008024
4	5 - 90	0.09427	0.001604
6	5 - 90	0.1413	0.002402
8	5 - 90	0.1883	0.003202
10	5 - 90	0.2351	0.003998
20	5 - 90	0.4663	0.007905
30	5 - 90	0.6912	0.01164
40	5 - 90	0.9087	0.01516
50	5 - 90	1.118	0.01844
60	5 - 90	1.319	0.02151
70	5 - 90	1.511	0.02437
80	5 - 90	1.695	0.02702
90	5 - 90	1.872	0.02951
100	5 - 90	2.040	0.03186
110	5 - 90	2.201	0.03408
120	5 - 90	2.354	0.03617
130	5 - 90	2.500	0.03816
140	5 - 90	2.640	0.04008
150	5 - 90	2.771	0.04190
160	5 - 90	2.90	0.0436
170	5 - 90	3.02	0.0452
180	5 - 90	3.13	0.0469
190	5 - 90	3.23	0.0484
200	5 - 90	3.32	0.0499

TABLE 6-4 (Continued)

Frequency of Fourier Component	Range of Data Points Used (cm)	Phase at Z=0 cm (Radians)	ξ (Rad cm^{-1})
210	5 - 90	3.41	0.0513
220	5 - 90	3.49	0.0527
230	5 - 90	3.56	0.0539
240	5 - 90	3.63	0.0549
250	5 - 85	3.66	0.0566
260	5 - 85	3.70	0.0579
270	5 - 80	3.74	0.0588
280	5 - 80	3.76	0.0601
290	5 - 75	3.78	0.0611
300	5 - 75	3.79	0.0619
310	5 - 70	3.79	0.0634
320	5 - 70	3.79	0.0645
330	5 - 65	3.79	0.0653
340	5 - 65	3.78	0.0667
350	5 - 60	3.78	0.0678
360	5 - 60	3.82	0.0672
370	5 - 60	3.86	0.0676
380	5 - 60	3.86	0.0703
390	5 - 60	3.85	0.0738
400	5 - 60	3.85	0.0770

for the low frequencies, and becomes somewhat less as the frequency increases. For the higher frequencies, data from detector positions far from the source were omitted as noted in the table. For frequencies exceeding 350 cps, the analysis of the amplitude data included the first 4 data points of necessity because of the rapid attenuation of the high frequency wave, and its small representation in the source neutrons for the experiment.

The error in the values of α given in Table 6-3 ranges from somewhat less than 1 per cent for the lower frequencies to approximately 5 per cent at 400 cps. However, in some columns, a large number of digits was used to report the results in order to show clearly the change in the results for each change in the frequency of analysis. The error in the values of ξ in Table 6-4 ranges from approximately 0.2 per cent for low frequencies to approximately 2 per cent at 400 cps.

Of course, the least squares fit of data to a straight line yields both the slope of the line and its intercept at the origin. Tables 6-3 and 6-4 give these quantities for the amplitude and the phase data as functions of frequency. These quantities define the effective source for the experiment. By regarding the results of the Fourier analysis at each position and frequency as the output, and the appropriate

effective source as the input, one can determine the transfer function for the system. Transfer function graphs of gain and phase shift versus frequency for several detector positions are given in Figs. 6-17 and 6-18.

The best values for α and ξ from Tables 6-3 and 6-4 are plotted as functions of frequency to 350 cps in Figs. 6-19 and 6-20. One may observe that the point-scatter in both curves increases with frequency.

The two quantities, $2\alpha\xi$ and $\alpha^2 - \xi^2$, are of special interest in that from the frequency dependence of these quantities, one can determine certain diffusion and thermalization parameters of the moderator.

Figure 6-21 is a graph of $2\alpha\xi$ as a function of frequency, and Fig. 6-22 is a graph of $\alpha^2 - \xi^2$ as a function of the square of the frequency. Note that the graph of $2\alpha\xi$ is almost linear, and passes through the origin. The point-scatter in this graph becomes severe at frequencies in excess of 350 cps.

There is considerable point-scatter in the graph of $\alpha^2 - \xi^2$, and most of it is due to errors in α. By comparing Fig. 6-22 with Fig. 6-17, one can see that when the value of α is slightly low for a particular frequency, the quantity $\alpha^2 - \xi^2$ is greatly affected. This sensitivity of $\alpha^2 - \xi^2$ to errors in either α or ξ increases with increasing frequency since α and ξ become more nearly equal in magnitude as the
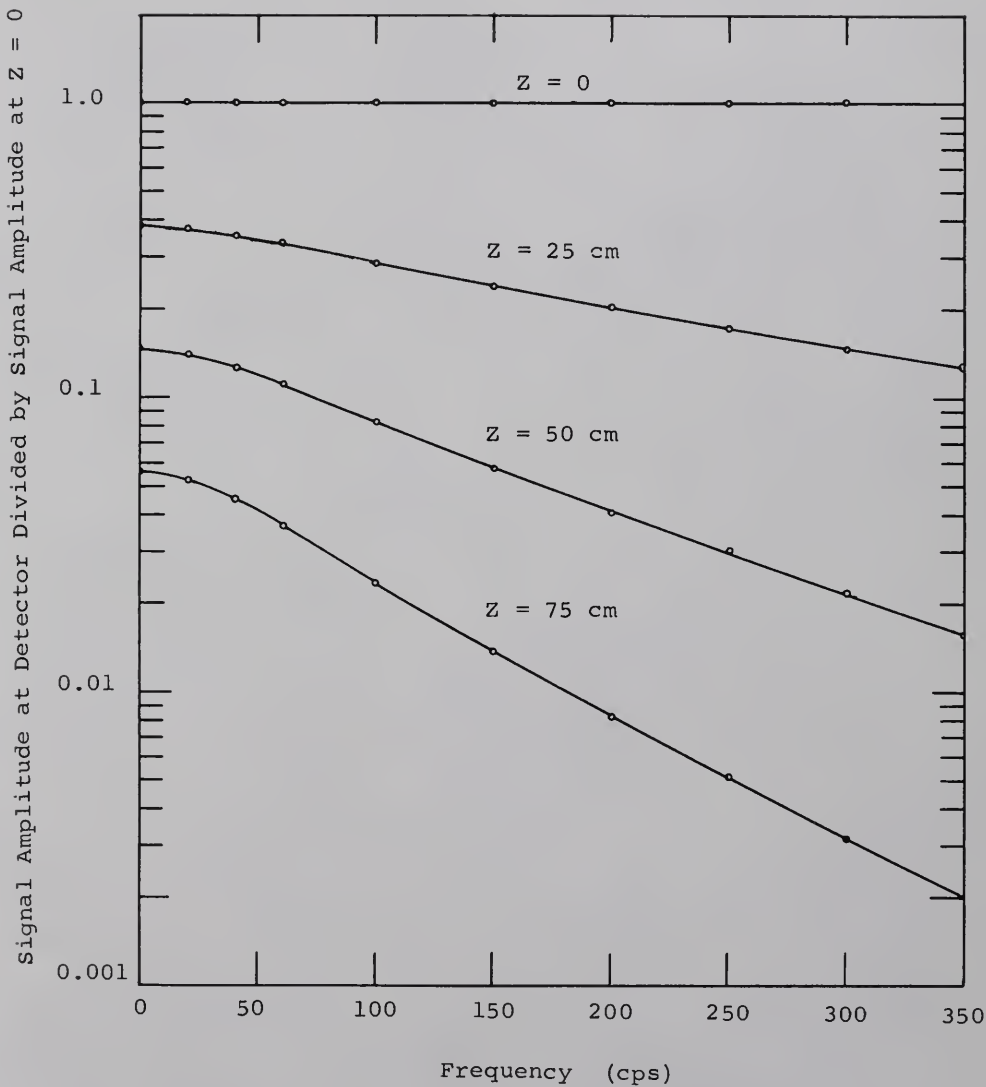
Fig. 6-17. Gain Versus Frequency in Heavy Water
for Several Detector Positions.
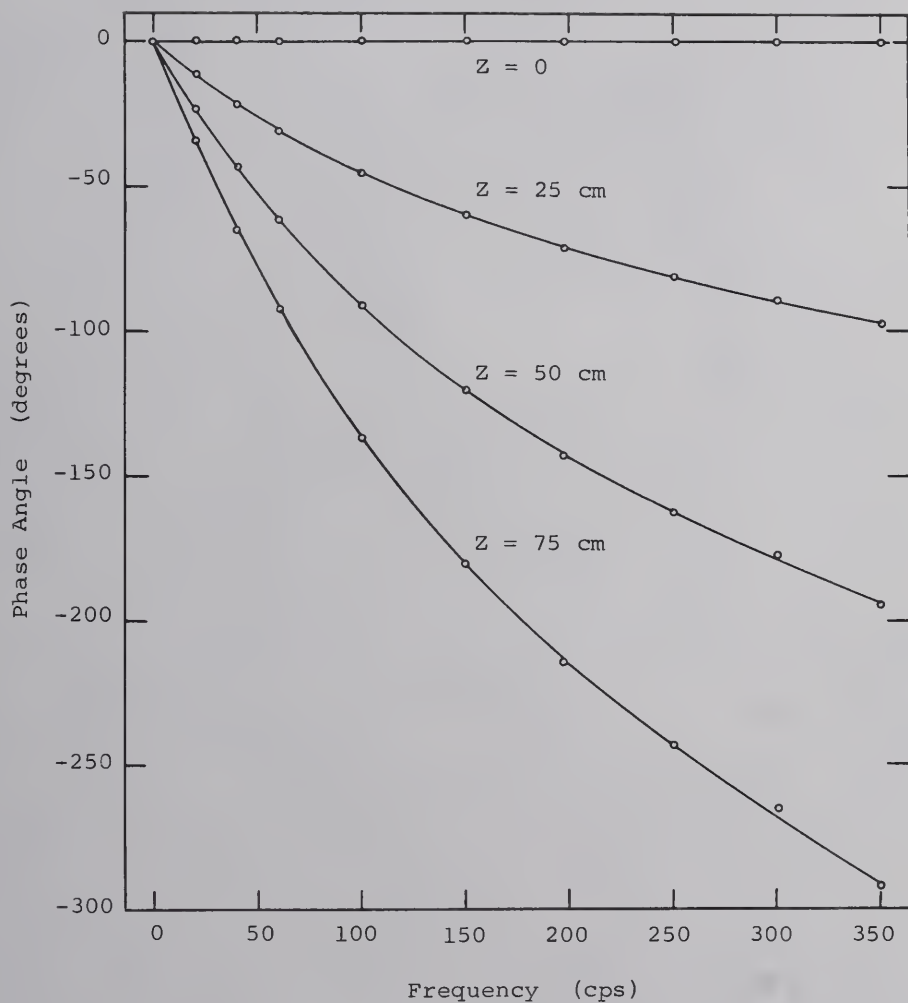
Fig. 6-18.   Phase Versus Frequency in Heavy Water
for Several Detector Positions.
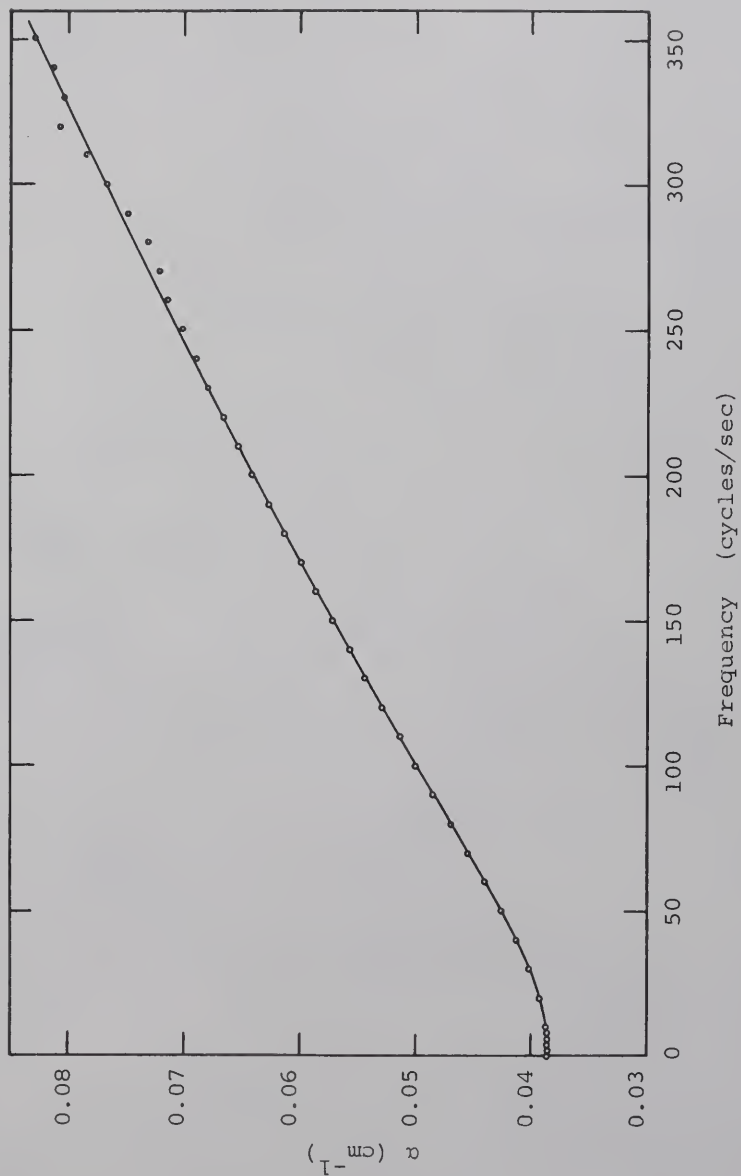
Fig. 6-19. Graph of α Versus Frequency for Thermal Neutron Wave Propagation in Heavy Water.
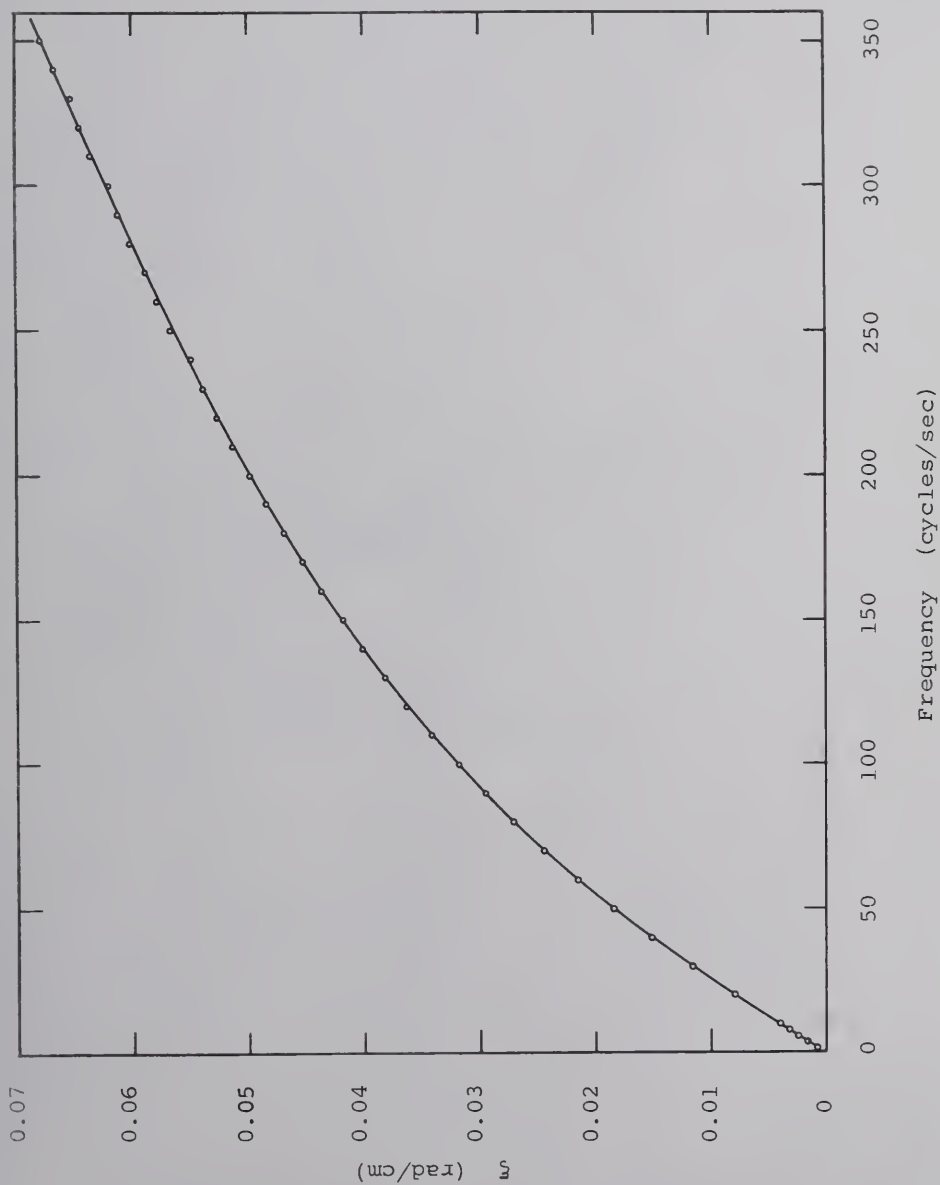
Fig. 6-20. Graph of ξ Versus Frequency for Thermal Neutron Wave Propagation in Heavy Water.
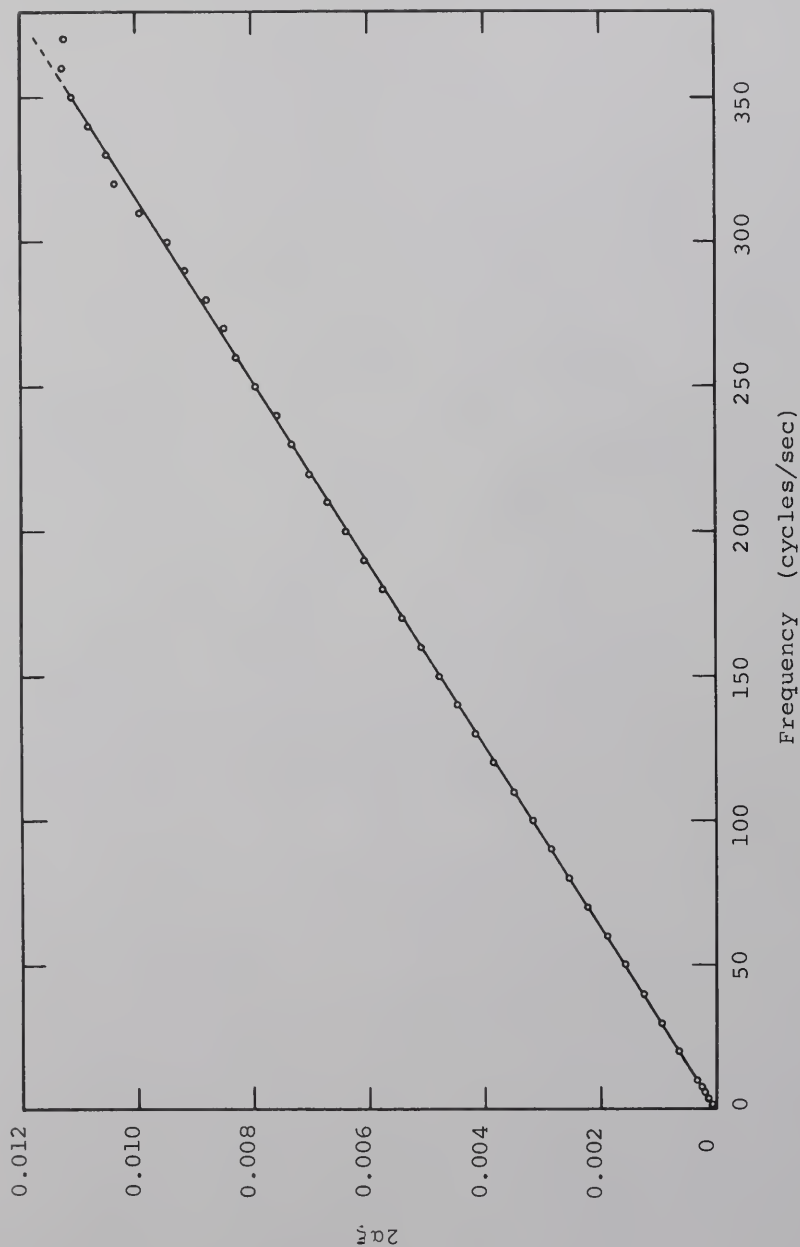
Fig. 6-21. The Function $2\alpha\xi$ Versus Frequency for Thermal Neutron Wave Propagation in Heavy Water.
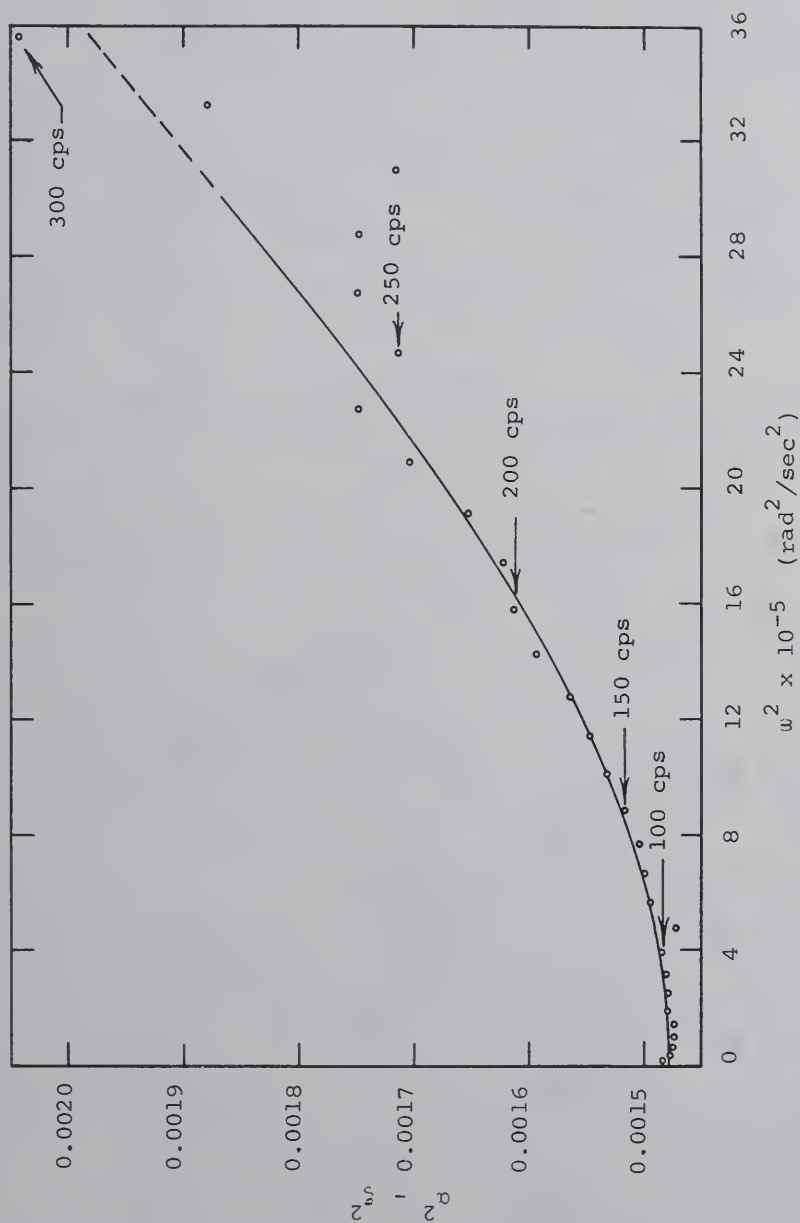
Fig. 6-22. The Function $\alpha^2 - \xi^2$ Versus Frequency Squared for Thermal Neutron Wave Propagation in Heavy Water.

frequency increases. (See Table 6-5.) This is unfortunate, because the experimental errors in both α and ξ also increase with increasing frequency, and the overall result is that a good quantitative determination of the frequency dependence of the function $\alpha^2 - \xi^2$ is rather difficult to obtain.

Next, certain diffusion and thermalization parameters will be obtained by a procedure used by Booth (16). His symbolism will be adopted, as well. Beginning with a relationship due to Perez and Uhrig (9),

$$\rho^2 = B_\perp^2 + \sum_{n=1}^{N} Q^{(n)} \left(\frac{\alpha_o + j\omega}{v_o} \right)^n \tag{6-1}$$

and substituting the relationships,

$$j\omega = -\lambda$$

and

$$-\rho = jB_z$$

one obtains:

$$-B^2 = -(B_z^2 + B_\perp^2) = \sum_{n=1}^{N} Q^{(n)} \left(\frac{\alpha_o - \lambda}{v_o} \right)^n$$

The above can be written as a series in powers of B^2:

$$\lambda = \alpha_o + D_o B^2 - C_o B^4 + F_o B^6$$

Thus one has an expression which will permit comparison with coefficients from die-away measurements. The coefficients are functions of the $Q^{(n)}$ coefficients, as follows:

TABLE 6-5

SENSITIVITY OF THE FUNCTION $\alpha^2 - \xi^2$
TO EXPERIMENTAL ERRORS IN THE VALUE OF α IN D_2O

Frequency (cps)	Per Cent Error in the Quantity $\alpha^2 - \xi^2$ for an Error of 1 Per Cent in the Value of ξ
0	2 %
100	4 %
200	5 %
300	6 %

$$\alpha_o = v_o \sum a_o$$

$$D_o = v_o / Q^{(1)}$$

$$C = -v_o Q^{(2)} / (Q^{(1)})^3$$

$$F_o = \left[v_o / (Q^{(1)})^5 \right] \left[2(Q^{(2)})^2 - Q^{(1)} Q^{(3)} \right]$$

Therefore, one can calculate the D_o, C_o, and F_o if v_o and the $Q^{(n)}$ coefficients are known.

The $Q^{(n)}$ coefficients can be determined as follows: Note that Eq. 6-1 is an expression of the squared complex relaxation length in a power series in w, and can be written in the following form, keeping terms up to the fourth power of w:

$$\rho^2 = P^{(0)} + P^{(2)} w^2 + P^{(4)} w^4 + j \left[P^{(1)} w^1 + P^{(3)} w^3 \right] \qquad (6-2)$$

Where

$$P^{(0)} = B_\perp^2 + \sum_{n=1}^{4} Q^{(n)} \left(\frac{\alpha_o}{v_o} \right)^n$$

$$P^{(1)} = \frac{1}{v_o} \left\{ Q^{(1)} + 2 \left(\frac{\alpha_o}{v_o} \right) Q^{(2)} + 3 \left(\frac{\alpha_o}{v_o} \right)^2 Q^{(3)} + 4 \left(\frac{\alpha_o}{v_o} \right)^3 Q^{(4)} \right\}$$

$$P^{(2)} = -\frac{1}{(v_o)^2} \left\{ + Q^{(2)} + 3 \left(\frac{\alpha_o}{v_o} \right) Q^{(3)} + 6 \left(\frac{\alpha_o}{v_o} \right)^2 Q^{(4)} \right\}$$

$$P^{(3)} = -\frac{1}{(v_o)^3} \left\{ Q^{(3)} + 4 \left(\frac{\alpha_o}{v_o} \right) Q^{(4)} \right\}$$

$$P^{(4)} = \frac{1}{(v_o)^4} \left\{ Q^{(4)} \right\}$$

Note from Eq. 6-2 that the real part of ρ^2 is described by terms in the series with even values of n, and that the imaginary part involves terms with the odd n coefficients. Recalling next that:

$$\rho = \alpha + j\xi \quad \text{and} \quad \rho^2 = (\alpha^2 - \xi^2) + j(2\alpha\xi),$$

one finds that the coefficients $P^{(0)}$, $P^{(2)}$, and $P^{(4)}$ can be obtained by fitting the function $\alpha^2 - \xi^2$ to the form:

$$\alpha^2 - \xi^2 = P^{(0)} + P^{(2)} w^2 + P^{(4)} w^4.$$

Likewise, values for $P^{(1)}$ and $P^{(3)}$ may be obtained by least squares fitting of the experimentally determined values of the quantity $2\alpha\xi$ to the form:

$$2\alpha\xi = P^{(1)} w + P^{(3)} w^3$$

The above procedure of (1) least squares fitting the experimental data to obtain the $P^{(n)}$ coefficients, (2) calculating the $Q^{(n)}$ coefficients from the $P^{(n)}$ coefficients, and (3) calculating the diffusion and thermalization parameters from the $Q^{(n)}$ coefficients was carried out, and the results are given in Table 6-6. In the fitting, the weight factor

TABLE 6-6

EXPERIMENTAL VALUES FOR $P^{(n)}$, $Q^{(n)}$, D_o, AND C_o FOR D_2O

Quantity*	With the Even $P^{(n)}$ Coefficients Computed by a Least Squares Fit to 36 Data Points on the $\alpha^2 - \xi^2$ Curve from 0 to 350 cps	With the Even $P^{(n)}$ Coefficients Computed by a Least Squared Fit to 31 Data Points on the $\alpha^2 - \xi^2$ Curve from 0 to 300 cps	With the Even $P^{(n)}$ Coefficients Computed by a Least Squares Fit to 26 Data Points on the $\alpha^2 - \xi^2$ Curve from 0 to 250 cps
$P^{(0)}$ cm^{-2}	1.4673×10^{-3}	1.4713×10^{-3}	1.474×10^{-3}
$P^{(1)}$ sec cm^{-2}	5.0083×10^{-6}	5.0083×10^{-6}	5.0083×10^{-6}
$P^{(2)}$ sec^2 cm^{-2}	4.7843×10^{-11}	3.9684×10^{-11}	1.9027×10^{-11}
$P^{(3)}$ sec^3 cm^{-2}	1.8026×10^{-14}	1.8026×10^{-14}	1.8026×10^{-14}
$P^{(4)}$ sec^4 cm^{-2}	2.4513×10^{-17}	2.5045×10^{-17}	5.3653×10^{-18}
$Q^{(1)}$	1.0020	1.0019	1.0018
$Q^{(2)}$ cm^2	-1.875	-1.549	-0.7205
$Q^{(3)}$ cm^4	-1.576×10^2	-1.578×10^2	-1.735×10^2
$Q^{(4)}$ cm^6	3.92×10^4	4.01×10^4	8.58×10^4
D_o cm^2 sec^{-1}	1.996×10^5	1.996×10^5	1.996×10^5
C_o cm^4 sec^{-1}	3.73×10^5	3.08×10^5	1.43×10^5

* For these calculations, $\alpha_o = 17$ sec^{-1}, and $v_o = 2 \times 10^5$ cm/sec.

assigned to each data point was $1/(\gamma_o)^2$, thus giving more weight to the better data.

The values of 5.0083 x 10^{-6} for $P^{(1)}$ and 1.8026 x 10^{-14} for $P^{(3)}$ in Table 6-6 were obtained from a two-parameter fit of $2\alpha\xi$ data through 350 cps. The $2\alpha\xi$ function is nearly linear. As a matter of interest, it was fitted to a straight line in a one-parameter least square determination, and the resulting value of $P^{(1)}$ was 5.0352 x 10^{-6}. Since 5.0352 differs from 5.0083 by less than 1 per cent, it is clear that the ω^3 term has little representation in the $2\alpha\xi$ function from zero to 350 cps in heavy water.

Because of the large amount of point-scatter in the results for $\alpha^2 - \xi^2$, least squares fits were made to this function over several different portions of the available data in order to provide a basis for estimating the experimental error in the P coefficients and in the values calculated from these coefficients.

In Table 6-6, the results of calculations based on three different frequency ranges of the $\alpha^2 - \xi^2$ curve are presented. Although the variation in $P^{(0)}$ for the three computations is less than 1 per cent, values for $P^{(2)}$ vary by a factor of 2.5, and the values of $P^{(4)}$ vary by a factor of 4.6.

The effect of errors in the $P^{(n)}$ coefficients upon the values of $Q^{(n)}$, C_O, D_O, and F_O will now be considered. The value of $Q^{(1)}$ is determined principally by $P^{(1)}$. Since $P^{(1)}$ is known with a relatively high degree of accuracy in this experiment, the value obtained for $Q^{(1)}$ is also reliable. And, one finds that the error in D_O is small since D_O is determined principally by $Q^{(1)}$.

The effect of errors in $P^{(2)}$ can be followed in a similar fashion. This error carries through to C_O, propagating through $Q^{(2)}$.

The value of F_O is dependent upon all four of the $Q^{(n)}$ coefficients. Although the expression for F_O contains $Q^{(1)}$ to the fifth power, this is not the principal source of error in F_O because $Q^{(1)}$ is known so much more accurately than some of the other coefficients. $Q^{(2)}$ appears in the expression as a squared term, and although it reflects the errors in $P^{(2)}$, it does not appear to be the principal source of error in F_O either. Using the values in Table 6-6, one finds that the term $Q^{(1)}Q^{(3)}$ is the principal quantity that lends uncertainty to the value of F_O. This is so because this product is both large (using the values of the table) compared with the other terms in F_O, and because this product is subject to large errors since $Q^{(3)}$ is directly sensitive to errors in $P^{(3)}$, and indirectly sensitive to $P^{(4)}$ through

the secondary dependence of $Q^{(3)}$ upon $Q^{(4)}$. A trial calculation of F_o based on the values in the table gave a result which was considered to be large and too uncertain to be included in this work. It appears that the point-scatter in the experimental determination of $\alpha^2 - \xi^2$ limits the determination of parameters to D_o and C_o.

Final values of C_o and D_o from the experiment are shown in Table 6-7, along with other published results for these parameters in heavy water, determined largely by the die-away technique. In view of the wide spread in the values of α_o chosen by various workers, it is fortunate that these parameters are not very sensitive to the value of α_o.

TABLE 6-7

COMPARISON OF EXPERIMENTALLY DETERMINED VALUES
OF C_o AND D_o FROM THIS WORK WITH PUBLISHED VALUES

Reference	α_o (sec^{-1})	D_o $(10^5 cm^2 sec^{-1})$	C_o $(10^5 cm^4 sec^{-1})$
Ganguly and Waltner (19)	15	2.039 ± .013	3.72 ± .5
Westfall and Waltner (20)	15	2.039 ± .013	4.18 ± .18
Kussmaul and Meister (21)	19	2.01	5.15
Malaviya and Profio (22)	10	2.045 ± .044	4.706 ± .381
Parkinson and Diaz (23)	17	1.99 ± .02	5.35
Parks and Baumann (24)	18	2.12 ± .02	8.1 ± .3
This Work (Neutron Waves)	17	1.996 ± .002	3.0 ± 1.0

CHAPTER VII

EXPERIMENTAL RESULTS FOR THE SUBCRITICAL ASSEMBLY

A.   Introduction

In this chapter, the results of the measurements out-
lined in Parts 5 and 6 of Table 5-2 are presented.

The neutron generator, thermalizing apparatus, sub-
critical assembly, and detection systems were as described
in Chapter IV. The full fuel loading was employed. The
reader is referred to Table 3-1 for the calculated neutron
parameters for the assembly, and to Appendix E for details
concerning the core calculations. The temperature and
purity of the moderator were as given in Section A of
Chapter V.

The experimental work with the loaded assembly was
performed after the measurements of Chapter VI were made
in the moderator without fuel. Since in Chapter VI, the
transverse flux studies as a function of time and frequency
had checked out the performance of the thermalizing appa-
ratus and had verified the fundamental mode and plane wave

assumptions, it was not necessary to do a transverse flux analysis in the loaded assembly. Other than the conventional pulse die-away measurements in Appendix G, only Z axis (in position 6, offset 2.175" as explained in Chapter IV) measurements were performed with the loaded assembly. As indicated in Table 5-2, the Z axis was explored first with the neutron generator operated as a continuous source; then pulse propagation measurements were performed for the determination of the dispersion law in a multiplying system.

B. Background Measurements in the Subcritical Assembly

In the loaded assembly, the background rate was too large to be ignored. Figure 7-1 shows a background flux map along the Z axis of the assembly with the cadmium shutter up, and again with the shutter down. No extra neutron source was used, and the neutron generator was off. With the shutter down, the heavy water assembly was effectively isolated from the thermalizing apparatus, and the background curve is quite symmetrical, having a nearly cosine shape. With the shutter up, the graphite of the thermalizing apparatus at one end of the assembly acts as a reflector causing an increase in the background rate at that end of the assembly.
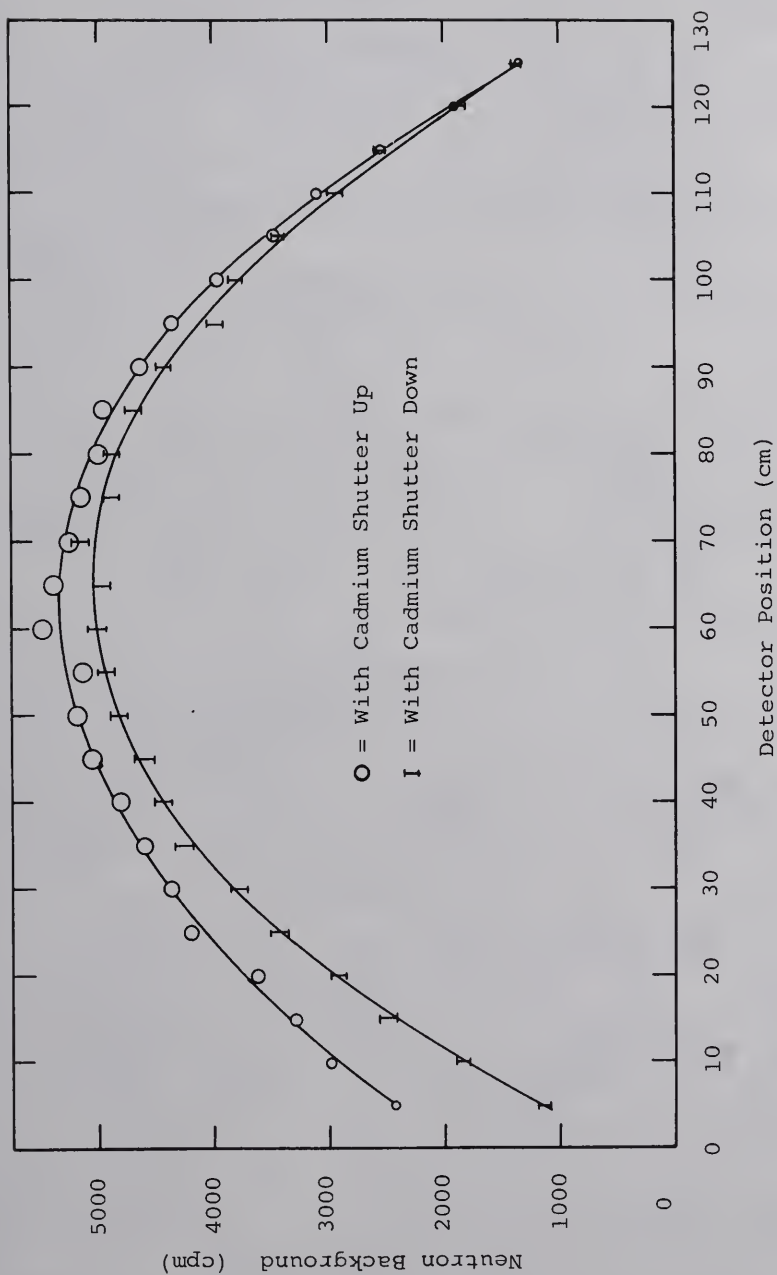
Fig. 7-1. Background Flux Distribution Along the Z Axis in the Subcritical Assembly.

O = With Cadmium Shutter Up

I = With Cadmium Shutter Down

Because the background rate seemed unusually large, a test was performed to determine if the background was caused by sensitivity to gamma radiation of the core. A graph of count rate versus detector voltage was obtained with the detector near a moderated Pu-Be source, and this curve agreed well with a similar characteristic curve obtained with the background as a source, indicating that the radiation being detected was of the same type in both cases. Further direct confirmation was obtained when the detector showed very little response to a Co-60 source at close range. The background was evidently due to neutrons released primarily by spontaneous fission in the fuel, along with some contribution from the (γ, n) reaction in D_2O.

C. Continuous Source Measurements Along the Z Axis

The procedure for these measurements has been described in Chapter V. Figure 7-2 gives the results of continuous source (zero frequency) measurements made with the cadmium shutter up, and with the shutter down. Curve B is related to the thermal neutron content of the source, and was obtained by subtraction of the shutter-down data from those obtained with the shutter up. Measurements in the range from about 30 cm to 75 cm appear to be free of
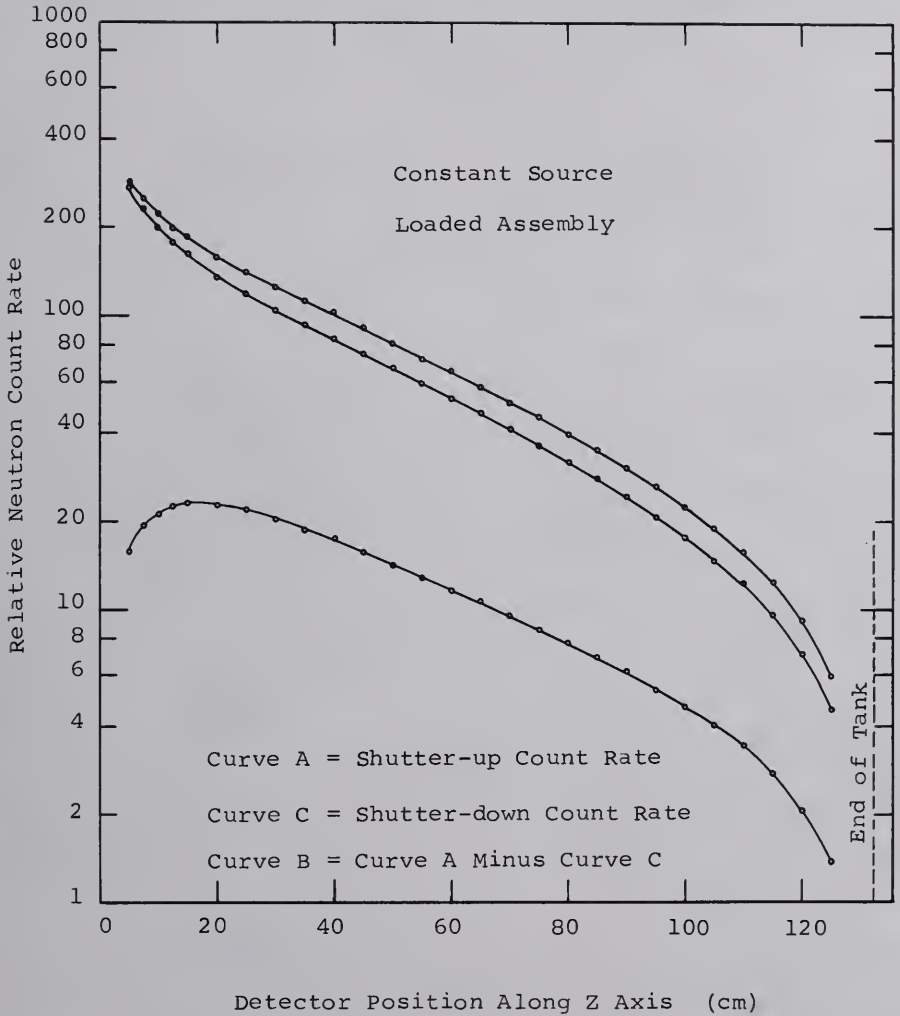
Fig. 7-2.   Continuous Source Flux Distribution Along the
Z axis in the Subcritical Assembly.

the effects of the finite length of the assembly and of
disturbances due to higher energy and spatial modes. The
shape of Curve C, with its peak at about 15 cm, reveals the
effect of thermalization of epicadmium neutrons. The initial
curvature of Curve B may also be partially due to the imper-
fection in the procedure of using the shutter and subtracting
one run from another, as discussed in Chapter V and later in
Chapter VI concerning Fig. 6-5. Note that Curve C lies two
decades below A or B.

D. <u>Pulse Propagation Measurements</u> <u>Along the Z Axis</u>

The shape of the 2 msec target pulse after passing
through the thermalizing apparatus is shown at the plane
$Z = 5$ cm in Fig. 7-3. This figure may be compared with
Fig. 6-8 for moderator only. Here again the broadening of
the pulse is associated with a loss of amplitude of the
higher frequency components of the signal. The data for
this graph were corrected for resolution loss and variations
in source strength, but the background has not been sub-
tracted at this stage. Only every tenth channel was
plotted in this figure.
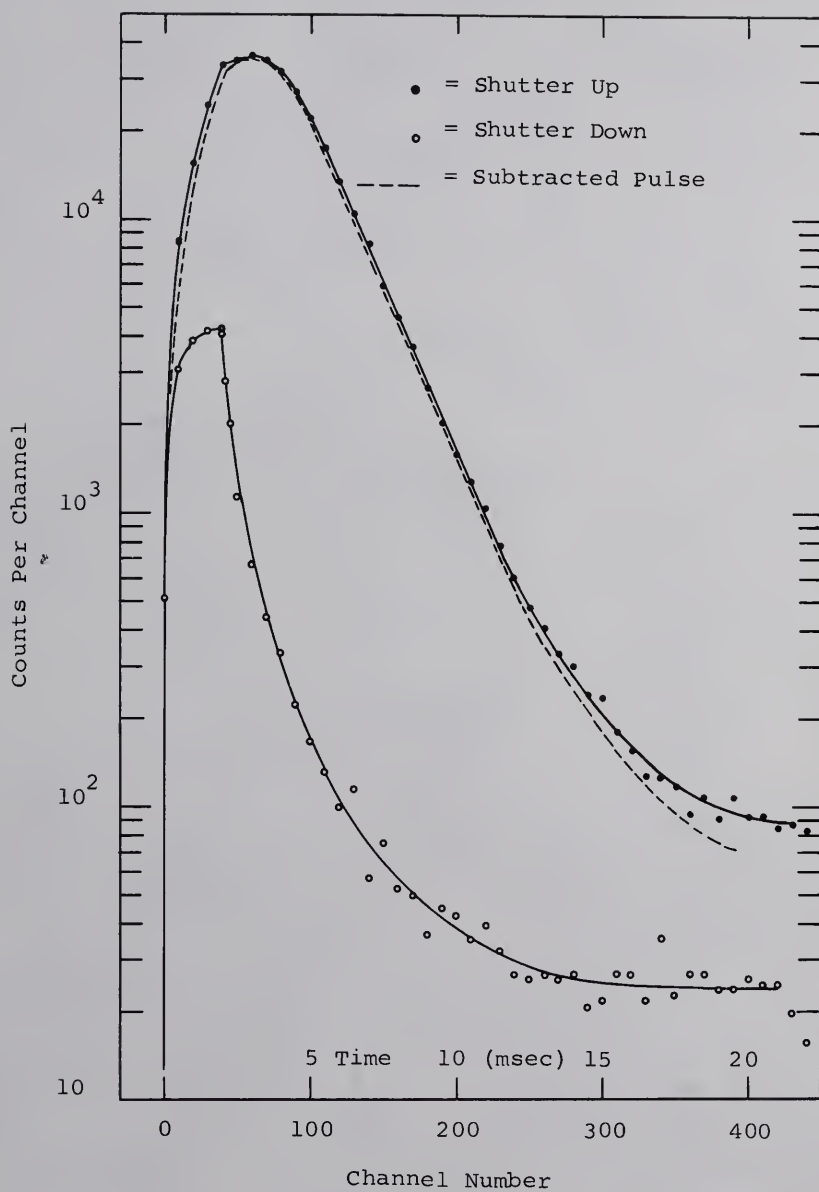
Fig. 7-3. Shutter-up, Shutter-down, and
           Subtracted Pulse at Z = 5 cm
           in the Subcritical Assembly.

As the pulse propagates down the assembly, it loses amplitude and continues to broaden, as the higher frequency content is lost more rapidly than the lower frequencies. This is seen in Fig. 7-4, in which the fully corrected, subtracted pulse is shown for three widely spaced detector positions. Note that a longer time is required for the peak to reach the more distant positions. The arrival time of the peak and the width of the pulse as a function of position are shown in greater detail in the next two figures.

In Fig. 7-5, the propagation velocity of the pulse peak is found to be essentially constant. The velocity as calculated from the slope of the straight line is 260 ± 10 m/sec. Therefore, approximately 5 msec is required for the peak to travel the full length of the loaded assembly. (Recall that in moderator only, the velocity of the peak was 177 m/sec, requiring 7.4 msec to travel the length of the tank.) Extrapolation of the graph shows that the pulse peak enters the source boundary about 3 msec after the beginning of the target pulse. If the peak is assumed to represent the middle of the 2 msec target pulse, one finds that the peak of those neutrons which arrive at the source boundary with energies less than the cadmium threshold require 2 msec travel time in the thermalizing apparatus.
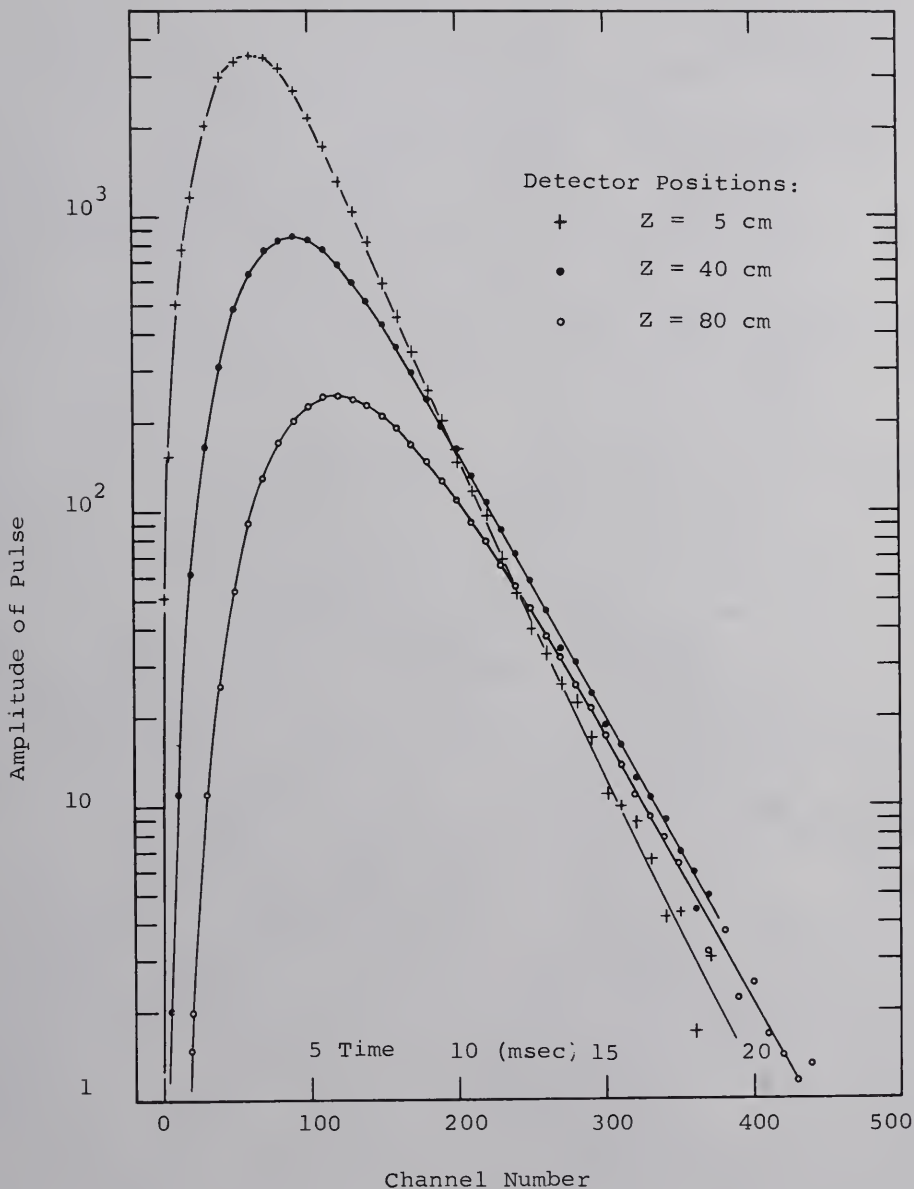
Fig. 7-4. Corrected Subtracted Pulse at Several
Detector Positions Along the Z Axis in
the Subcritical Assembly.
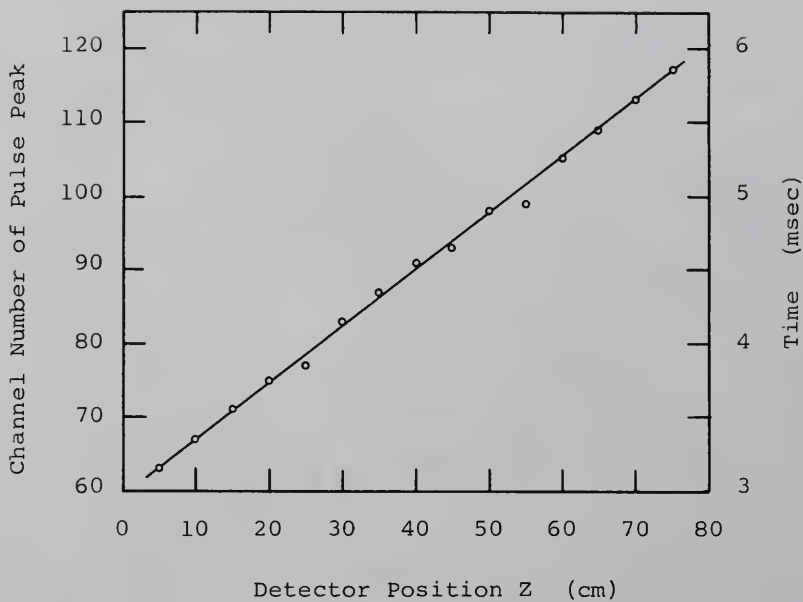
Fig. 7-5. Propagation of the Peak of
the Subtracted Pulse in the
Subcritical Assembly.

The width of the pulse as a function of position is shown in Fig. 7-6. Extrapolation of these curves to zero centimeters would yield widths descriptive of the pulse entering the assembly.

The relative amplitudes of the Fourier components of the fully corrected, subtracted pulse as a function of frequency for three widely separated detector positions are shown in Fig. 7-7. These graphs represent only a portion of the experimental results obtained. The analysis was performed for detector positions spaced 5 cm apart, and for frequencies at intervals of 10 cps from zero to 350 cps. Above 350 cps, and especially for large distances from the source, the amplitude of the signal became small relative to the statistical error in the content of each channel, and the point-scatter in both the amplitude and phase results from the analysis became excessive. (The moderator-only results in the previous chapter had less point-scatter, in general, than was encountered here. The higher background, greater absorption, and fissions in the loaded assembly all contribute to this difference in the appearance of the data points.) As would be expected, a comparison of the three curves shows that the high frequency content of the pulse received at distant positions is proportionately
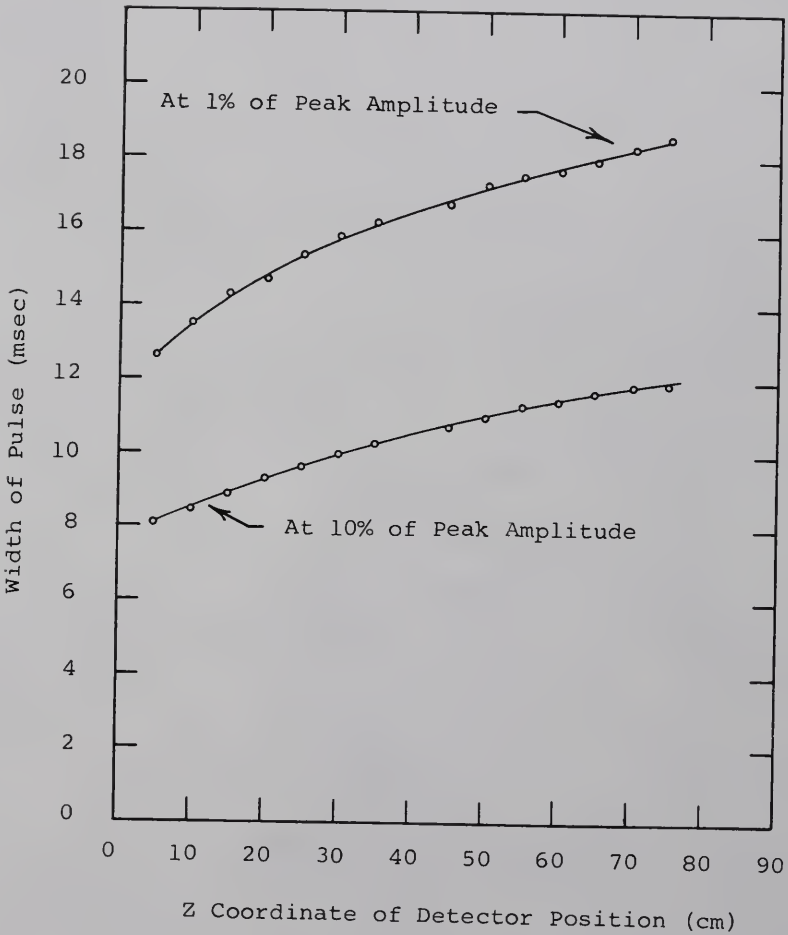
Fig. 7-6. Width of the Subtracted Pulse
as a Function of Position in
the Subcritical Assembly.
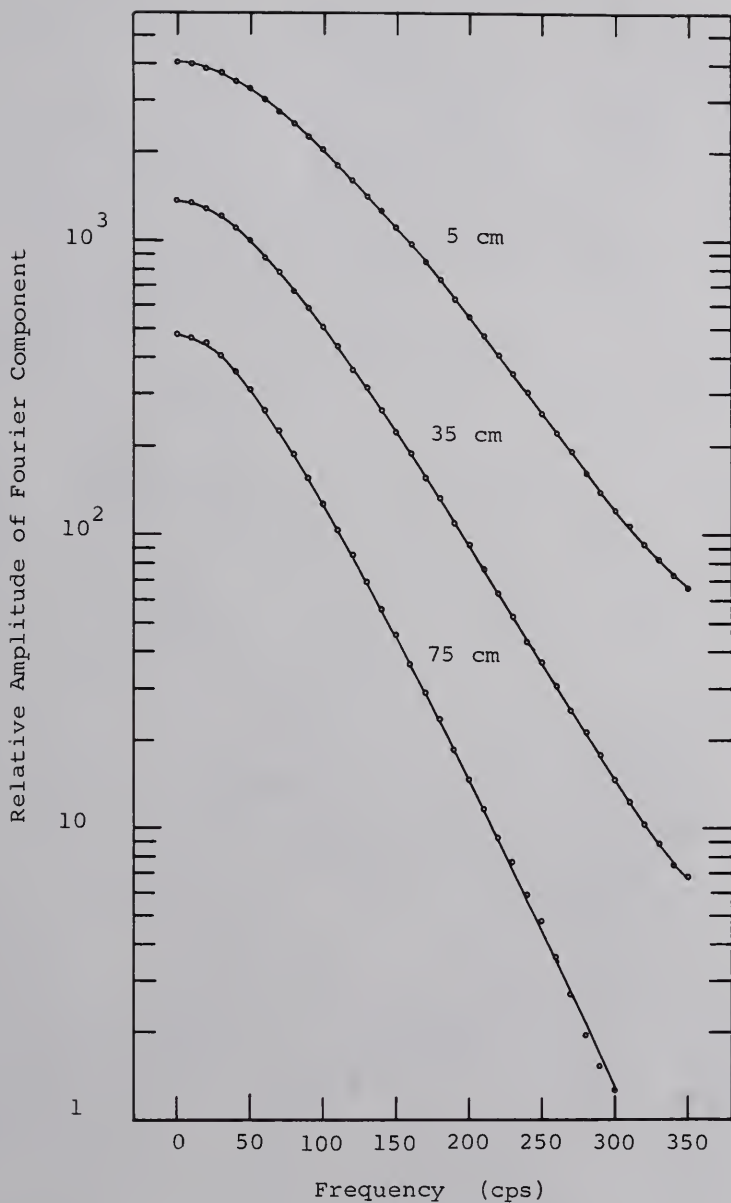
Fig. 7-7. Amplitude of Fourier Components Versus
Frequency for Several Positions in the
Subcritical Assembly.

less than at positions closer to the source. If the pulse were a delta function in time, these curves would be horizontal straight lines, indicating an equal representation for all frequencies. If a narrower pulse could be delivered by the thermalizing apparatus, the measurements could cover a wider frequency range than is the case here.

Amplitude and phase results for several frequencies are plotted as functions of position in Figs. 7-8 and 7-9. The zero frequency amplitude curve agrees with that obtained earlier in the continuous source measurement. (This agreement is essential, and constitutes a cross-check between the continuous source measurements and the pulse measurements.) The amplitude curve for each frequency is essentially a straight line on the semilog graph except for the positions nearest the source, where the effect of several factors named earlier is seen. Careful inspection of Fig. 7-9 reveals a steeper slope in the portion of the curve near the source. A break in the slope of the phase curves at about 25 to 30 cm was somewhat more distinct in another set of data not shown here. The departure from linearity in both graphs is more pronounced than that found in the moderator-only results, where no detectable breaks were seen in the slopes of the phase curves. In both the
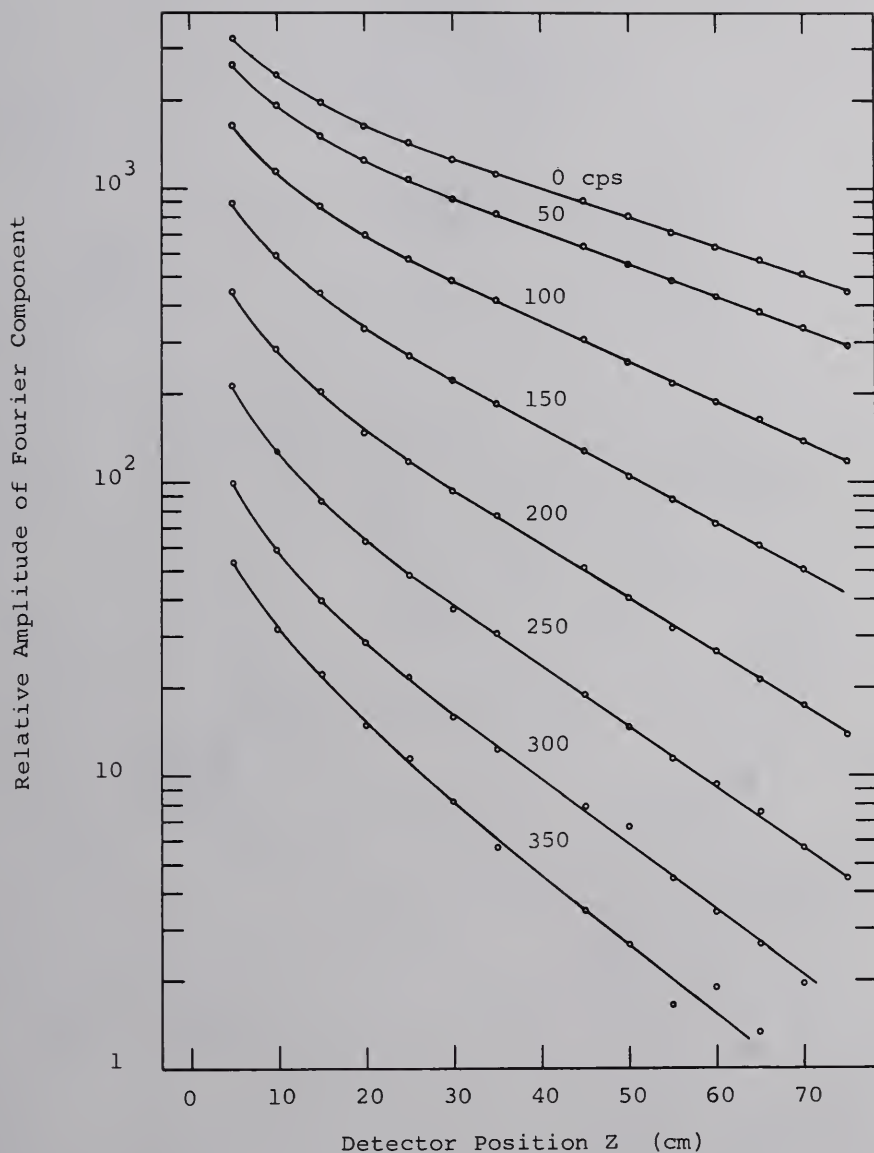
Fig. 7-8. Amplitude of Fourier Components Versus Position for Several Frequencies in the Subcritical Assembly.
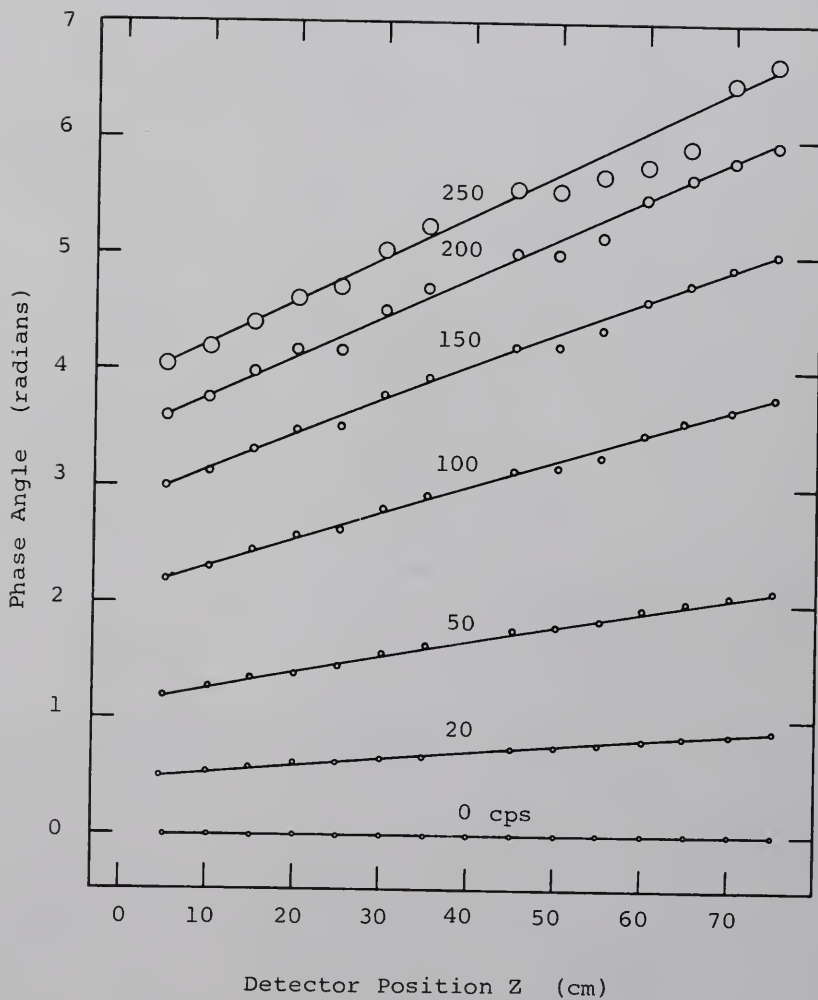
Fig. 7-9. Phase Angle of Fourier Components Versus
Position for Several Frequencies in the
Subcritical Assembly.

moderator results and the loaded assembly results, the
phase calculation is less affected by disturbances near
the source than the amplitude calculation. Of course, the
slopes of both the amplitude and phase curves become steeper
with increasing frequency, and both α and ξ therefore in-
crease with frequency.

The data analysis was performed as described in Fig.
5-1. The resulting values of α and ξ are plotted versus
frequency in Fig. 7-10, and listed in Table 7-1. The point-
scatter in the values of ξ was disappointing in that much
smoother phase results were obtained in an earlier analysis
which had to be discarded because of flaws in another area.
Ordinarily, the point-scatter in ξ has been found to be
considerably less than that in α. (Smoother results could
be obtained by including the data from detector positions
close to the source, but this would introduce a systematic
error even more objectionable than the more random point-
scatter.)

The error in the values of α and ξ presented in
Table 7-1 is estimated to range from approximately 1 per
cent for low frequencies to approximately 5 per cent for
330 cps. A sufficient number of digits is used to show
the change in the result for each frequency.
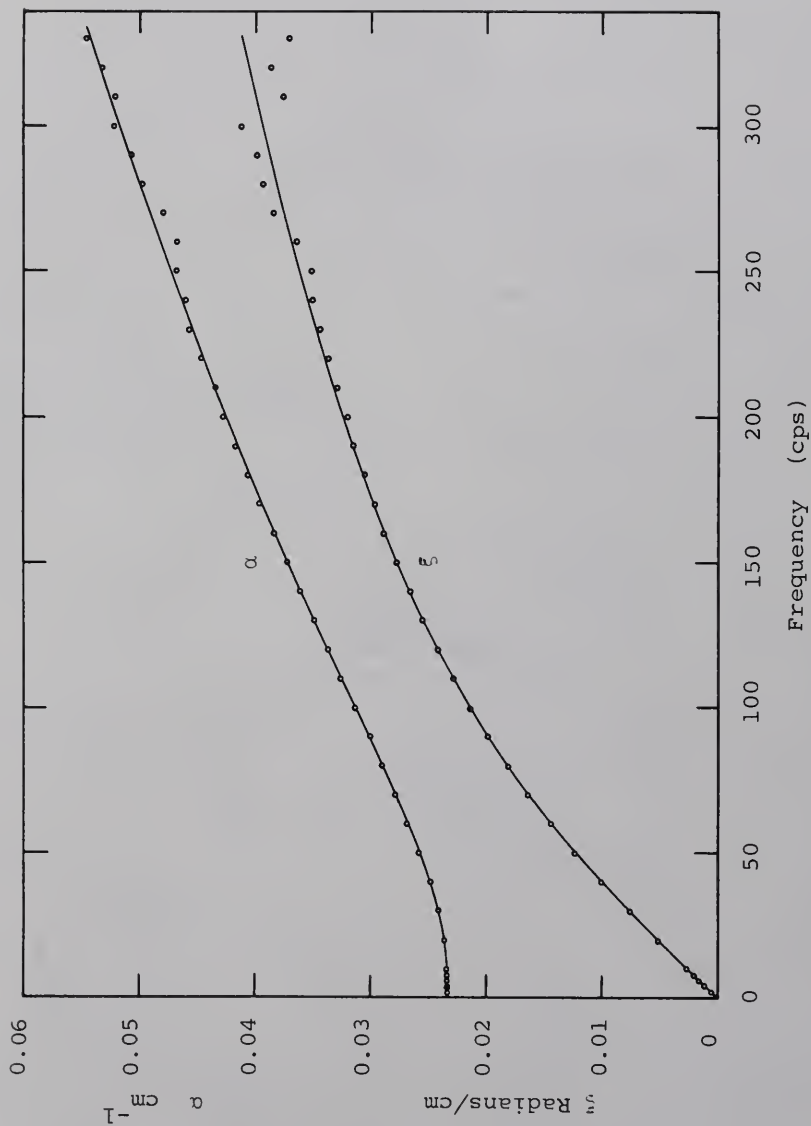
Fig. 7-10. The Functions α and ζ Versus Frequency
for the Subcritical Assembly.

TABLE 7-1

EXPERIMENTAL VALUES OF α
AND ξ IN THE SUBCRITICAL ASSEMBLY

Frequency Of Fourier Component	Amplitude at Z=0 cm	α (cm^{-1})	Phase at Z = 0 cm (Radians)	ξ $(Rad\ cm^{-1})$
0	7.8499	0.02330	0	0
2	7.8494	0.02330	0.05189	0.0005167
4	7.8478	0.02331	0.1037	0.001034
6	7.8452	0.02331	0.1552	0.001553
8	7.8416	0.02336	0.2065	0.002073
10	7.837	0.0234	0.2574	0.002595
20	7.805	0.0237	0.5075	0.005182
30	7.755	0.0243	0.7501	0.007667
40	7.690	0.0250	0.9778	0.01012
50	7.613	0.0259	1.203	0.01227
60	7.527	0.0268	1.409	0.01441
70	7.436	0.0279	1.611	0.01634
80	7.337	0.0290	1.802	0.01815
90	7.235	0.0302	1.983	0.01986
100	7.128	0.0314	2.158	0.02141
110	7.02	0.0326	2.32	0.0229
120	6.90	0.0337	2.49	0.0242
130	6.78	0.0349	2.64	0.0255
140	6.66	0.0361	2.78	0.0267
150	6.53	0.0372	2.92	0.0278
160	6.40	0.0385	3.05	0.0289
170	6.27	0.0396	3.18	0.0297
180	6.12	0.0406	3.30	0.0306
190	5.98	0.0418	3.41	0.0315
200	5.83	0.0428	3.53	0.0320

TABLE 7-1 (Continued)

Frequency Of Fourier Component	Amplitude at Z=0 cm	α (cm^{-1})	Phase at Z = 0 cm (Radians)	ξ $(Rad\ cm^{-1})$
210	5.67	0.0435	3.62	0.0330
220	5.53	0.0447	3.71	0.0337
230	5.35	0.0451	3.78	0.0344
240	5.19	0.0459	3.85	0.0351
250	5.04	0.0469	3.93	0.0352
260	4.83	0.0467	3.95	0.0364
270	4.70	0.0480	3.93	0.0385
280	4.59	0.0498	3.94	0.0393
290	4.45	0.0507	3.96	0.0398
300	4.36	0.0522	3.94	0.0413
310	4.17	0.0521	4.14	0.0376
320	4.05	0.0532	4.10	0.0386
330	3.96	0.0545	4.17	0.0370

Transfer function graphs of the gain and phase versus frequency for several detector positions were calculated from the experimental values of α and ξ , and are presented in Figs. 7-11 and 7-12.
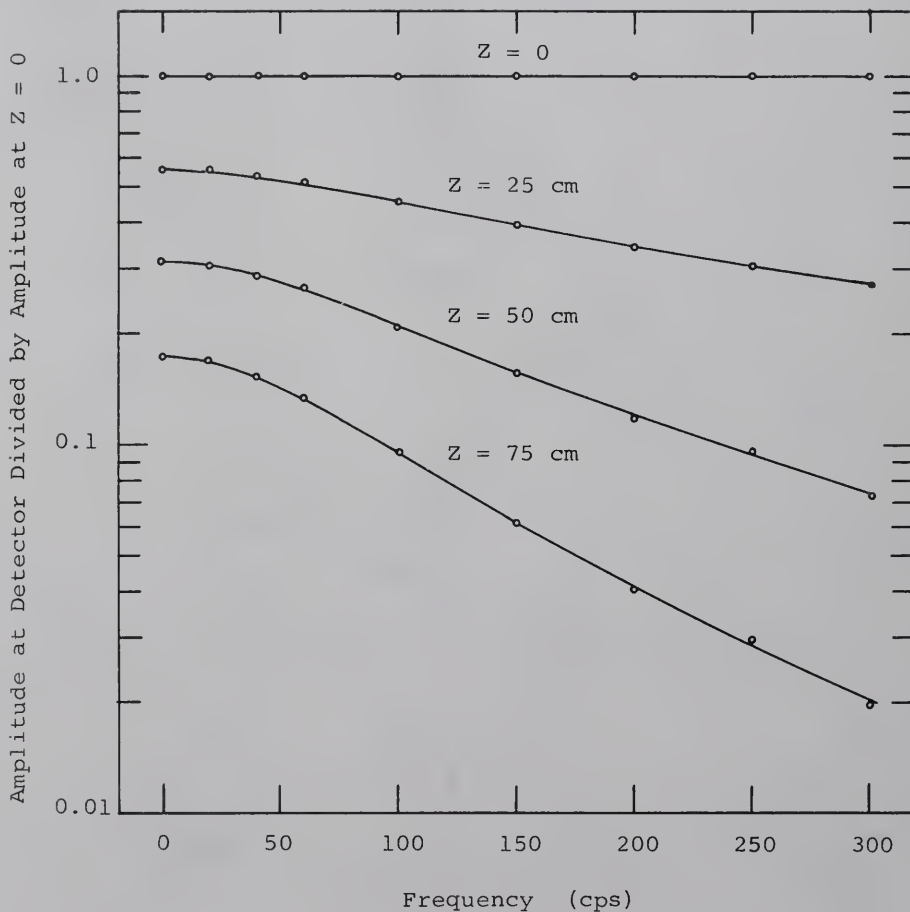
Fig. 7-11. Gain Versus Frequency for Several Detector
Positions in the Subcritical Assembly.
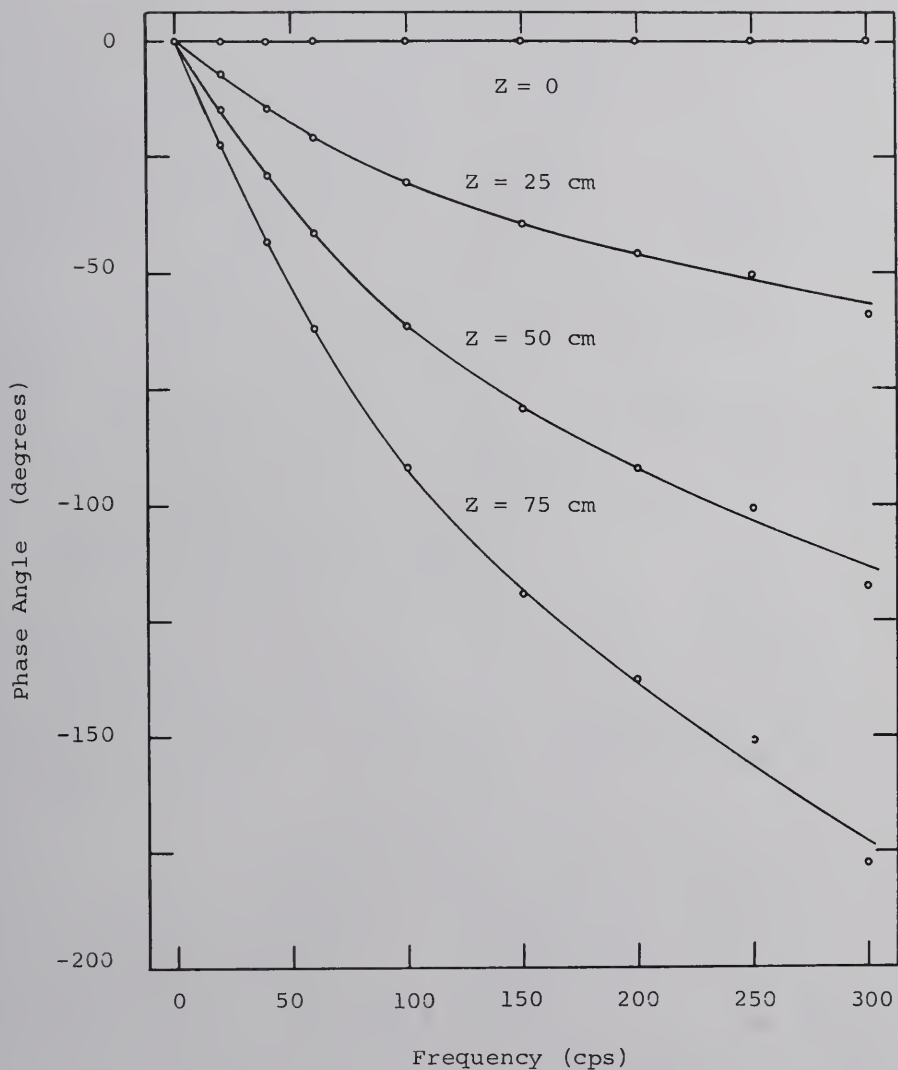
Fig. 7-12.   Phase Versus Frequency for Several Detector
Positions in the Subcritical Assembly.

CHAPTER VIII

COMPARISON OF THEORY AND EXPERIMENT

In this chapter the calculated results from the two-group model and from the age-theory model are presented for comparison with the experimental results for the subcritical assembly. Also, the power series in the angular frequency derived in Chapter III will be explored as a tool for obtaining lattice parameters directly.

A. Comparison of Experiment and the Results from Two-group Theory

The calculation based on two-group theory was carried out as outlined in Chapter II, using the parameters of Table 3-1. The resulting values of α and ξ are shown in Table 8-1 and in Figs. 8-1 and 8-2 along with the experimental results for comparison. Two-group theory yields values of α which generally lie within two per cent of the experimental values throughout the entire range of the experiment. The calculated curve for α falls below the experimental results by 1.5 per cent at zero frequency. One should not assume

163

TABLE 8-1

COMPARISON OF CALCULATED RESULTS FROM AGE THEORY AND
FROM TWO-GROUP THEORY WITH THE RESULTS FROM THE EXPERIMENT

Freq. (cps)	Experimental Results		Newton-Raphson Age-theory Calculation		Two-group Calculation	
	α cm^{-1}	ξ rad/cm	α cm^{-1}	ξ rad/cm	α cm^{-1}	ξ rad/cm
0	0.023300	0	0.02336	0	0.0229	0
2	0.023304	0.0005168	0.02337	0.000548		
5	0.023312	0.001334	0.02340	0.001367		
10	0.02339	0.002595	0.02353	0.002721		
20	0.0237	0.00518	0.0240	0.00534	0.0236	0.00507
30	0.0243	0.00767	0.0247	0.00778		
40	0.0250	0.0101	0.0255	0.0100	0.0251	0.00950
50	0.0258	0.0123	0.0265	0.0121		
60	0.0268	0.0144	0.0275	0.0140	0.0271	0.0132
70	0.0279	0.0163	0.0285	0.0157		
80	0.0290	0.0182	0.0295	0.0173	0.0292	0.0163
90	0.0302	0.0199	0.0305	0.0188		
100	0.0314	0.0214	0.0316	0.0202	0.0314	0.0190
200	0.0428	0.0320	0.0410	0.0311	0.0416	0.0285
300	0.0522	0.0413	0.0491	0.0387	0.0511	0.0344
400			0.0564	0.0446	0.0604	0.0381
500			0.0631	0.0492	0.0697	0.0400
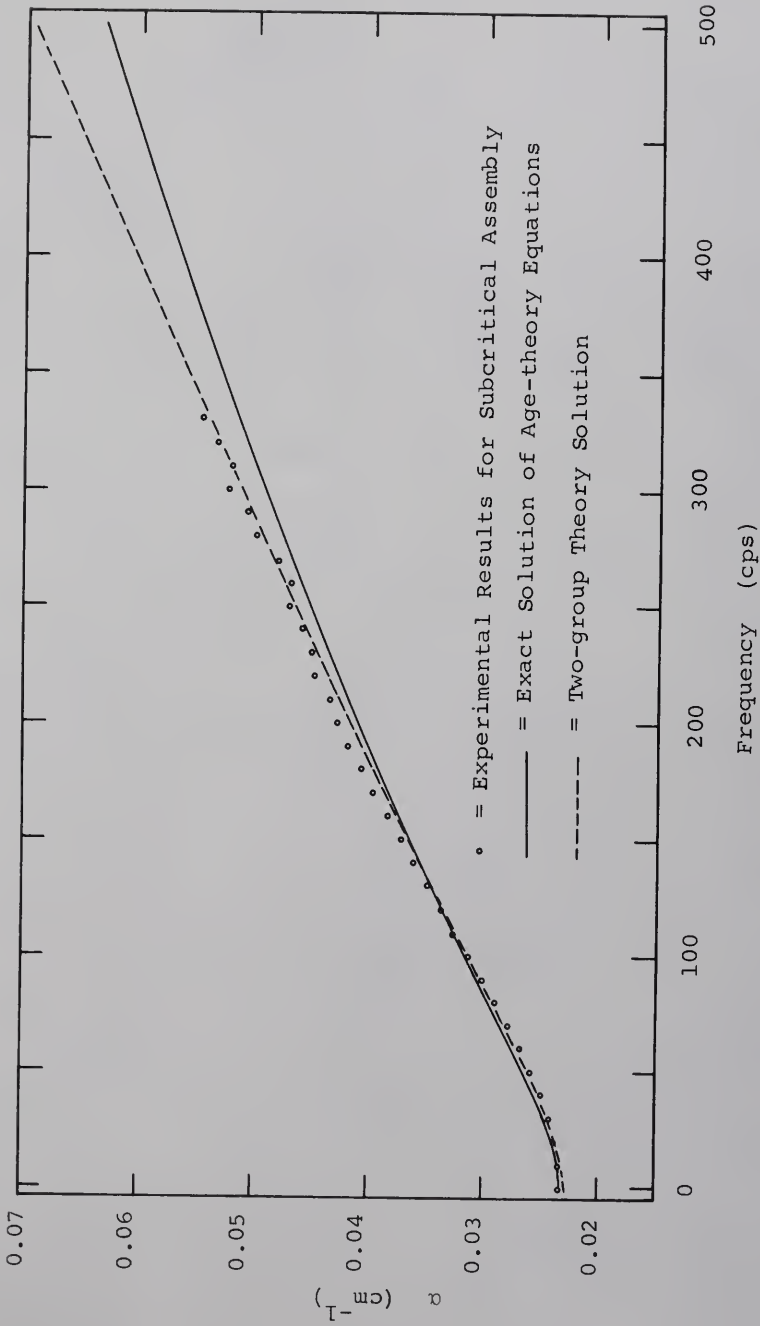
Fig. 8-1. Graph of α Versus Frequency for the Experiment, for Two-group Theory, and for Age Theory.

° = Experimental Results for Subcritical Assembly

— = Exact Solution of Age-theory Equations

----- = Two-group Theory Solution

Frequency (cps)

α (cm^{-1})
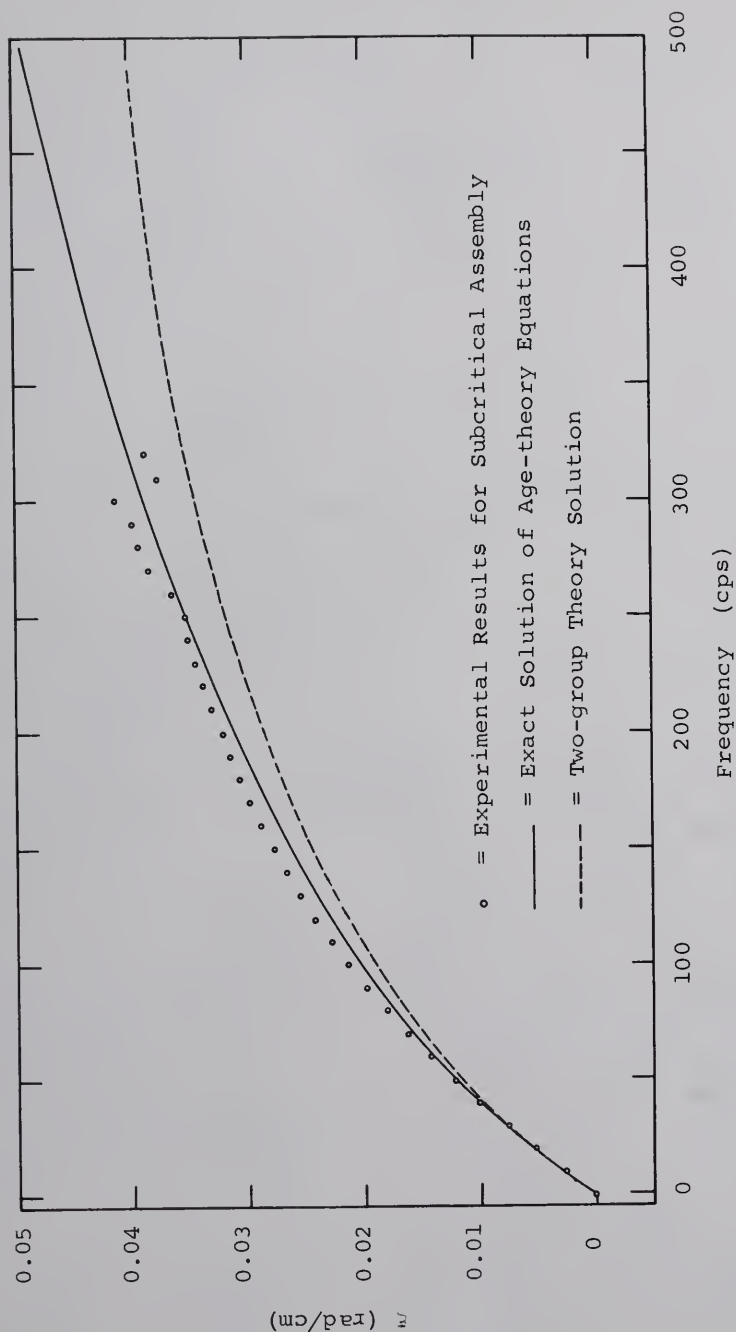
Fig. 8-2. Graph of ξ Versus Frequency for the Experiment, for Two-group Theory, and for Age Theory.

that this disagreement is inherent with the model used, as
the value of α is quite sensitive to errors in the param-
eters used in the computations. (For example, an error of
1 per cent in k_∞ was found to result in an error of approxi-
mately 5 per cent in α.)

Figure 8-2 shows that the two-group values for ξ agree
with the experimental results at low frequencies, but fall
below the experimental curve for frequencies above approxi-
mately 50 cps. Furthermore, Table 8-2 shows that the
calculated ξ reaches a maximum value at approximately 550
cps and decreases thereafter. Since there is no reason to
expect the phase shift to actually decrease with an increase
in frequency, this behavior is believed to be evidence of
the failure of the two-group model outside the low frequency
range. This failure appears to be of such a nature that it
could not be remedied by simple adjustment of the values of
the parameters used in the computation. It is possible that
the limitation of the model is a consequence of the lack of
provision for the neutron slowing-down time in the group-
diffusion model.

TABLE 8-2

RESULTS OF THE TWO-GROUP THEORY CALCU-
LATION USING THE PARAMETERS IN TABLE 3-1

Frequency (cps)	α_{-1} (cm^{-1})	ξ (rad/cm)
0	0.0229	0
20	0.0236	0.00507
40	0.0251	0.00950
60	0.0271	0.0132
80	0.0292	0.0163
100	0.0314	0.0190
150	0.0366	0.0244
200	0.0416	0.0285
250	0.0464	0.0318
300	0.0511	0.0344
350	0.0558	0.0365
400	0.0604	0.0381
450	0.0650	0.0393
500	0.0697	0.0400
550	0.0744	0.0401
600	0.0791	0.0395
650	0.0837	0.0380
700	0.0877	0.0354
750	0.0905	0.0323
800	0.0922	0.0293
850	0.0931	0.0267
900	0.0937	0.0246
950	0.0941	0.0228
1000	0.0943	0.0212
1050	0.0945	0.0199
1100	0.0946	0.0188
1150	0.0947	0.0178
1200	0.0948	0.0169
1250	0.0950	0.0161
1300	0.0950	0.0153

B. Comparison of Experiment and the Exact Solution of the Age-theory Equations

Table 8-1 lists values of α and ξ obtained from the experiment and from the Newton-Raphson computer solution of Eqs. 3-4 and 3-5, using the parameters listed in Table 3-1. Table 8-1 and Figs. 8-1 and 8-2 show that for both α and ξ, and for frequencies up to 330 cps, the agreement between the experimental results and the results from the exact solution of the age-theory equations is within approximately 6 per cent. In general, age theory appears to give good results for low frequencies. Between 150 cps and 330 cps, age theory tends to underestimate α by several per cent. It should be pointed out that the almost exact agreement in the values of α at zero frequency is not entirely accidental because after it was found that the age-theory results are sensitive to the value of the quantity, $k_\infty/\epsilon L^2$, the value of ϵ in the calculations was adjusted by trial from the original assumed value of 1.03 to 1.027 in order to normalize the curves at zero frequency. This change of only 0.3 per cent is well within the uncertainty of most of the parameters used, and this was the only value which was adjusted to facilitate the comparison.

The experimental results and the results from the exact

solution of the age-theory equations are further compared

in Figs. 8-3 and 8-4. In Fig. 8-3, the rather sensitive

quantity, $\alpha^2 - \xi^2$, is plotted versus frequency. Figure 8-4

shows $2\alpha\xi$ versus frequency. These quantities, as calcu-

lated from age theory, differ from the experimental values

by around 10 per cent for some frequencies.

In general, the agreement between age theory and the

experiment is quite good at low frequencies. For higher fre-

quencies, disagreement is to be expected for several reasons:

1. The model uses only one group of thermal neutrons.
    Hence thermalization phenomena are not included.
    These effects are significant in a well-thermalized
    medium such as that used, and should begin to affect
    the results at about 50 cps.

2. At still higher frequencies, the higher roots of the
    dispersion law (roots associated with higher slowing
    down modes) will influence the results. However,
    from the semigraphical study of the dispersion law
    (Appendix H), it appears that those roots are much
    larger than the roots associated with the fundamental
    mode. Therefore higher mode contamination is expected
    to be small.

3. The relatively large scatter of the experimental data
    around 300 cps is due to the fact that the frequency
    spectrum of the input pulse falls off for higher
    frequencies. The relatively small high frequency
    signal results in the poor statistical accuracy of
    the experimental values.
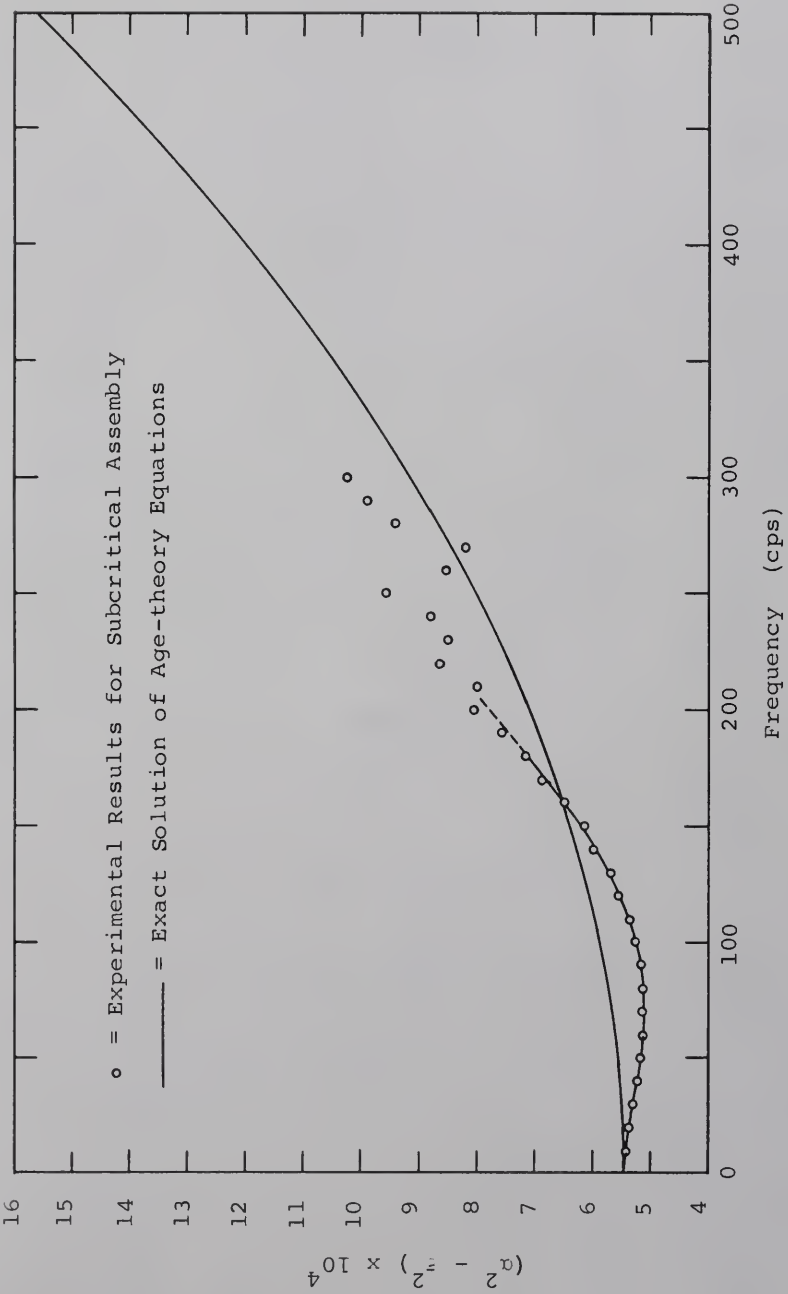
Fig. 8-3. Graph of $\alpha^2 - \zeta^2$ from Age Theory and from the Experiment.

o = Experimental Results for Subcritical Assembly

—— = Exact Solution of Age-theory Equations

172

Fig. 8-4. Graph of $2\alpha\xi$ from Age Theory and from the Experiment.

o = Experimental Results for Subcritical Assembly

—— = Exact Solution of Age-theory Equations

Frequency (cps)

$2\alpha\xi \times 10^5$
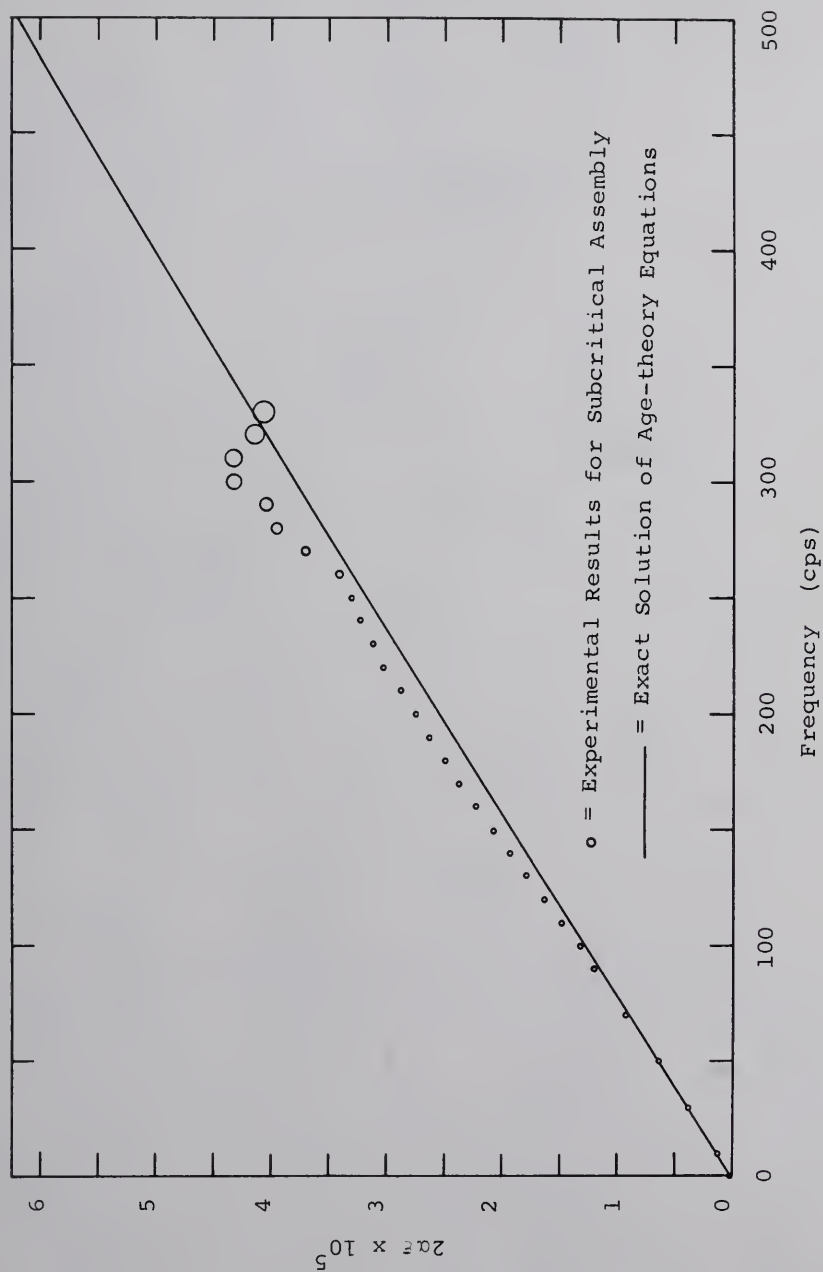
C. Determination of Lattice Parameters
from the Dispersion Law

Unless the reasonably good agreement between theory and experiment shown in the previous section is merely accidental, this agreement implies that the three basic ingredients of the comparison: (1) the theoretical model, (2) the numerical values for the nuclear parameters used in the calculation based on the model, and (3) the experimental results, are all reasonably correct. The view taken thus far has been that the nuclear parameters and the experimental measurements are both accurate enough for the comparison to be essentially a text of the theoretical models as a function of frequency. Now, since the validity and usefulness of especially the age-theory model in the appropriate frequency range has been demonstrated, consideration will be given to methods of determining nuclear parameters by making use of the experimentally determined dispersion law.

The direct comparison method

Suppose one wishes to determine the value of one of the parameters in the age-theory equations, already knowing all the other parameters, and having a reliable experimental determination of the dispersion law. The unknown parameter could be determined in trial-and-error fashion

by repeatedly calculating the dispersion law based on assumed values of the parameter, and comparing the resulting dispersion law with that from the experiment. Agreement would indicate that a good value for the parameter has been obtained. This direct comparison method could be applied to find values for two or more parameters at the same time, though probably with some loss of accuracy.

Use was made of this direct comparison method on one occasion in this work to improve the value of one parameter. Actually, in this work, three sets of lattice parameters were used in the calculations. Except for the instances explained below, the parameters were obtained through CEPTR and BUCKSHOT calculations as described in Appendix E. The three sets of parameters differ in the following way: In set A, the fast fission factor was taken as unity. The dispersion law based on this set had the usual overall shape in that both α and ξ increased with frequency, but the quantitative agreement with the experiment was poor, even for low frequencies. In set B, the average velocity of the thermal neutrons was slightly changed in accordance with some estimations derived from the work of Diaz (25) and Meister (26), and the fast fission factor was taken to be 1.03. With this set, agreement with experiment was improved. At this point the Newton-Raphson computer code was available, and the

sensitivity of the dispersion law to the ratio k_∞/ϵ was dis-
covered and investigated. It was found that agreement
(especially for α) with the experiment for low frequencies
is obtained for a value of $k_\infty/\epsilon = 1.1684$, as used in Set C,
given earlier in Table 3-1. (Actually, since k_∞ and ϵ appear
in the ratio, it does not matter which is varied for the pur-
pose of finding a satisfactory value of the ratio. By
leaving k_∞ constant, ϵ took on the value of 1.027, which
should not be regarded as the absolutely true value of this
parameter, but merely a value which when used with the other
parameters results in a set which describes the system
satisfactorily.) Set C therefore was taken as the set which
best describes the natural uranium, heavy water moderated
system for the static case and for a reasonable frequency
range as well. In this set, τ and L^2 are in very good agree-
ment with a wealth of results from static experiments per-
formed at the Savannah River National Laboratory (27), and
at the University of Florida (25,28) for lattices of natural
uranium and heavy water. See Table 8-3. The value
$D_o = 2.22 \times 10^5$ cm^2 sec^{-1} is also consistent with the
measured value found for heavy water in Chapter 5.

The power series expansion method

With the above method it is difficult, if not impossible,

TABLE 8-3

LATTICE CONSTANTS FOR TWO SUBCRITICAL CONFIGURATIONS*

Pitch (cm)	11.93	15.88
τ (cm^2)	129.6	124.5
L^2 (cm^2)	92.9	173.2
D_o $(cm^2 sec^{-1})$	2.22×10^5	2.17×10^5
k_∞	1.196	1.242

*From Reference 25.

to predict the influence of a given lattice parameter upon
the dispersion law without repeated numerical calculations.
Also, the transcendental equations descriptive of the dis-
persion law do not lend themselves to the extraction of
parameters. This difficulty is overcome through the use
of the power series expansion outlined in Chapter III.

For convenience in nomenclature, let $B^2(n)$ be defined
as the coefficient of the term containing w^n in Eqs. 3-8
and 3-9. These various $B^2(n)$ coefficients could be ob-
tained by least squares fitting the experimental results to
the appropriate power series in w. From the $B^2(n)$ coeffi-
cients so obtained, various parameters can be computed,
using the series expansions. Also, the effect of a given
parameter upon the dispersion law can be easily investigated
because the power series method yields combinations of
parameters (that is, the various $B^2(n)$ coefficients) which
impose restrictions on the values that can be assigned to
the lattice constants. In the event that enough constraints
of the above type can be extracted from the experiment the
question of self-consistency of a given set of constants
describing the nuclear systems may be examined. In the limit
with this procedure, a large number of $B^2(n)$ coefficients
are determined by fitting the experimental results, and all
the lattice constants are found, one by one. In practice,

of course, the number of $B^2(n)$ coefficients and the corresponding number of lattice constants which can be determined from the experimental results as outlined above are limited in number and accuracy by the reliability associated with the age-theory model and the accuracy and frequency range of the experimental work. It appears unlikely that one could obtain the experimental dispersion law with sufficient accuracy over a sufficiently wide frequency range to permit the determination of as many $B^2(n)$ coefficients as would be necessary to determine all of the nuclear parameters that appear in the age-theory representation. The practical limitation lies largely in the sensitivity of the quantity $\alpha^2 - \xi^2$ to errors in either α or ξ, especially for higher frequencies since the magnitudes of α and ξ become more nearly equal as the frequency increases. Since the function $2\alpha\xi$ is less sensitive to errors than the above, it appears that there may be less difficulty in obtaining the $B^2(n)$ coefficients for odd n's than for even n's.

The method proposed in this section was tried on the experimental results from the subcritical assembly. The practical limitations mentioned above permitted an accurate determination of only the zero frequency intercept, $B^2(0)$, and the slope, $B^2(1)$. Table 8-4 shows the experimental values of $B^2(0)$ and $B^2(1)$ from this work, along with similar

TABLE 8-4

THE DEPENDENCE OF THE $B^2(n)$ COEFFICIENTS UPON LATTICE PITCH
FOR ONE-INCH DIAMETER NATURAL URANIUM CYLINDRICAL SLUGS IN D_2O

Coefficient	11.88 cm pitch*	11.93 cm pitch**	15.88 cm pitch**
$B^2(0)$ cm^{-2}	7.17×10^{-4}	7.14×10^{-4}	13.25×10^{-4}
$B^2(1)$ $cm^2 sec$	2.03×10^{-6}	2.06×10^{-6}	2.60×10^{-6}
$B^2(2)$ $cm^2 sec^{-2}$		1.13×10^{-10}	1.68×10^{-10}

* From Reference 25. A triangular lattice with a pitch of 11.88 cm is
 equivalent to the square lattice of the assembly used in the present work.

** The values for 11.93 cm and 15.88 cm were obtained by private communication
 with N. J. Diaz, University of Florida.

results from another source for comparison. From the experi-

mental values in Table 8-4 and Eqs. 3-9 and 3-10, one obtains

the following two conditions:

$$\frac{k_\infty}{\epsilon L^2} e^{-B^2(0)\tau} - \frac{1}{L^2} = 7.17 \times 10^{-4} \tag{8-1}$$

$$\frac{\frac{1}{D_o} + L_s\,(1/L^2 + B^2(0))}{1 + B^2(0)\tau + \frac{\tau}{L^2}} = 2.03 \times 10^{-6} \tag{8-2}$$

If one is interested in determining some parameter from

each of the above equations (knowing the other parameters),

he can now do so. For example, suppose the ratio, k_∞/ϵ,

and the slowing-down time, L_s, are to be determined and

that the other parameters have been determined from some

independent measurement or calculation. Using parameters

from Set C in Eqs. 8-1 and 8-2, the ratio, k_∞/ϵ, and the

slowing-down time are found to be 1.169 and 48×10^{-6},

respectively. These results are in good agreement with

their corresponding values in Set C, and demonstrate the

internal consistency of the set of lattice parameters used

in the direct method.

CHAPTER IX

CONCLUSIONS AND RECOMMENDATIONS

A. <u>Conclusions</u>

The main goal of this dissertation, the measurement of the dispersion law for a subcritical reactor, has been achieved for the first time.

A considerable fraction of the time associated with the experiment was required for the construction of the subcritical assembly with its special features designed to protect the valuable investment of heavy water from evaporation and from contamination by atmospheric moisture. The end product has proven to be a versatile apparatus which is presently being used in a variety of neutron wave experiments.

The thermalizing apparatus also represents a significant achievement. It was designed and built as an integrated system optimized to provide thermal neutrons in the fundamental transverse spatial mode for delivery to the subcritical assembly as plane waves. The success of

the thermalizing apparatus made it possible to describe the

experimental results with reactor equations in which the

higher spatial modes are eliminated and the longitudinal and

transverse parts are separable.

Although the procedure for the data analysis followed

the general pattern developed for previous neutron wave

experiments at the University of Florida, significant refine-

ments were introduced, especially in the resolution correction,

which was applied to each channel of the analyzer data. The

method of determining resolution times (Appendix B), and the

method of making resolution corrections for the reference

detector in pulse work (Appendix C) were devised to meet

specific problems, but are of a sufficiently general nature

to have application in related work. The main conclusions

which may be drawn from this study are listed below.

1.   Both the real and the imaginary parts of the com-
        plex inverse relaxation length for thermal neutrons
        were found to increase smoothly with frequency in
        both the moderator without fuel present, and in
        the loaded subcritical assembly. No exceptional
        frequencies, pass bands, or stop bands were found
        by theory or experiment in the range of fre-
        quencies studied.

2.   Effects of the slowing-down process appear to be
        important at high frequencies. (That the Fermi
        age-diffusion theory describes the high frequency
        behavior in a more correct fashion than the two-
        group treatment is a consequence of the more accu-
        rate description of slowing down in the age theory.)

3.   Since neither model gives entirely satisfactory
      agreement with the experiment, it appears that
      thermalization effects should be included to
      describe the dispersion law of well-moderated
      systems.

4.   The corollary of the previous conclusion is that
      the neutron wave propagation technique imposes a
      stringent test on the theoretical model.

5.   An interesting discovery made in the parameter
      search performed in the process of fitting the
      age-diffusion model to the experimental results
      was the sensitivity of the dispersion law to the
      value of the infinite multiplication factor, K_∞.
      This property of the dispersion law could become
      in the future a powerful tool for the measurement
      of reactor shut-down margin. See Table 9-1.

6.   The age-diffusion model, using lattice parameters
      computed by the CEPTR and BUCKSHOT codes, describes
      well the low frequency behavior of the system
      investigated in this dissertation. Therefore, the
      lattice parameters (Set C, Table 3-1) constitute
      an accurate and consistent set of design parameters
      for heavy water natural uranium reactors. These
      results are in agreement with the results obtained
      by Parkinson and Diaz (23), using combined die-
      away and static measurements.

7.   The high frequency range of the dispersion law
      gives information on the fast transient behavior
      of the system at zero power. The fact that this
      region is not well described by our theoretical
      model points out the need for further research
      in this direction.

TABLE 9-1

SENSITIVITY OF THE $B^2(n)$ COEFFICIENTS TO SMALL
CHANGES IN THE INFINITE MULTIPLICATION FACTOR

Coefficient	Per Cent Change in Coefficient For a 1 Per Cent Change in k_∞
$B^2(0)$	+ 12.5 %
$B^2(1)$	+ 5.7 %
$B^2(2)$	+ 8.8 %

B.   Recommendations

Theoretical

To obtain a better description of the high frequency
range, the age-diffusion model should be refined to take
into account the higher slowing-down modes and thermaliza-
tion effects. It would be of interest to compare the
results from an improved age-theory model with those from
an improved multigroup model containing several thermal
neutron groups and various narrow groups in the epithermal
region.

There are areas which were touched upon but not ex-
plored in this work, such as the interesting shapes of the
shutter-down flux curves and the thermalization process
causing this. Also in this work, in order to avoid the
problem of applying an end effects correction for the
finite tank, no use was made of data taken in the end
third of the tank. Someone may wish to undertake the prob-
lem of deriving the expression for the amplitude and phase
of this position and frequency dependent end correction
term.

Future research with the present equipment

The accelerator, thermalizing apparatus, and subcriti-
cal assembly used in this dissertation could be used after
minor modification to study several new problems:

Anisotropic effects.--Anisotropy in reactor lattices
can be studied by causing the wave to propagate in a direc-
tion transverse to the fuel rods instead of longitudinally
as in this dissertation.

Shut-down margin.--Wave propagation as a function of
lattice pitch can be studied to measure reactor shut-down
margin.

Control rods.--The effect of control rods upon neutron
propagation can also be investigated with minor changes in
the present equipment.

Cadmium shutter.--A quantitative study of the effect
of the cadmium shutter, as discussed in Chapter V, would
also be of interest.

Improvements in the experimental apparatus

The frequency range from zero to approximately 350 cps
can be investigated with the present equipment. The upper
limit is established by the necessity of using a relatively
large amount of moderator material to develop the funda-
mental transverse spatial mode and to thermalize the 14.7

MeV source neutrons from the tritium target. The thermal-
izing apparatus itself absorbs the high frequency signal
preferentially, and delivers a neutron pulse which is broad
in time. One avenue of improvement would be the use of a
deuterium target in order to obtain neutrons of lower initial
energy which would not require so large a thermalization
apparatus, but the yield from this reaction for a 150 KeV
machine is very low, and the loss in counting rate would
make this change prohibitive. Significant improvement of
the experiment at the University of Florida appears to be
possible only through the use of the 4 MeV pulsed Van de
Graaff accelerator, which can produce neutrons copiously in
the KeV range by use of other reactions.

A second limitation encountered in the experiment was
found in the instability of the electronic gear used. The
detector systems were checked against a standard Pu-Be
source almost daily, and were found to drift about 1 or 2
per cent per day--an error 10 times as large as the statis-
tical error in 10^6 counts. Also, some of the electronic
equipment tended to be unreliable if the room temperature
exceeded approximately 70° F. In view of these troubles,
it appears that a special cooling system for the equipment,
in addition to ordinary building air-conditioning may be
needed.

APPENDIX A

SPATIAL DISTRIBUTION OF NEUTRONS
FROM THE THERMALIZING APPARATUS

A physical description of the thermalizing apparatus
is given in Chapter IV. This section contains the results
of flux measurements across the horizontal mid-line of the
graphite output face of the thermalizing apparatus. In terms
of the coordinate system described in Chapter IV, the flux
measurements were made along the X axis.

These measurements were performed with the thermaliz-
ing apparatus rolled away from the subcritical assembly.
This fact is mentioned to emphasize that except for room
scattering, the spatial flux distribution presented here is
entirely that of neutrons leaving the graphite face for the
first time, and not the result of albedo effects between a
graphite source region and an adjacent D_2O reflector.
(Such albedo effects would result in a more nearly cosine
distribution at the interface than that for source neutrons
crossing the interface from graphite to D_2O for the first
time. A comparison of the following graphs with the trans-
verse flux map in Chapter VI for zero frequency at Z = 5 cm

in D_2O will illustrate the above effect.) Because of its
localized sensitive volume, a Li-6 scintillation detector
was used for these measurements. For the epicadmium measure-
ments, the entire detector was wrapped with cadmium.

The following three graphs show total, epicadmium, and
subcadmium flux distributions for continuous mode (zero
frequency) operation of the neutron generator. Each curve
is slightly more peaked than the plotted cosine, showing a
detectable amount of higher spatial modes. Separate measure-
ments with a He-3 detector gave a cadmium ratio of approxi-
mately 90 at the center of the graphite surface.

The subcadmium flux distribution could have been
brought into even closer agreement with the plotted cosine
by a careful distribution of a few square inches of cadmium
sheet inside the graphite, placed near the Z axis, and about
a foot or so from the outer face. A few trials were made
using cadmium in this way to reduce the flux peaking, and
the results looked promising, but the idea was not pursued
to completion for lack of time, and because the flux distri-
bution was quite satisfactory without further refinement.
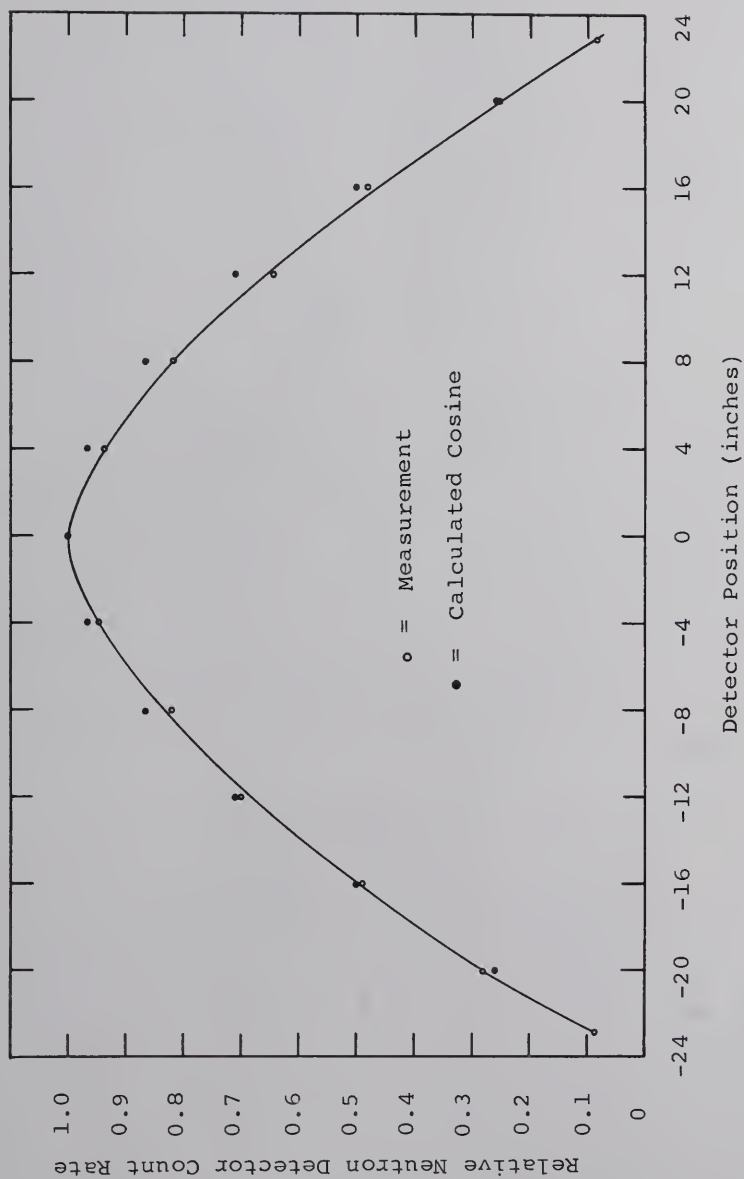
Fig. A-1. Subcadmium Flux Across the Horizontal Midline of the Graphite Face of the Thermalizing Apparatus.
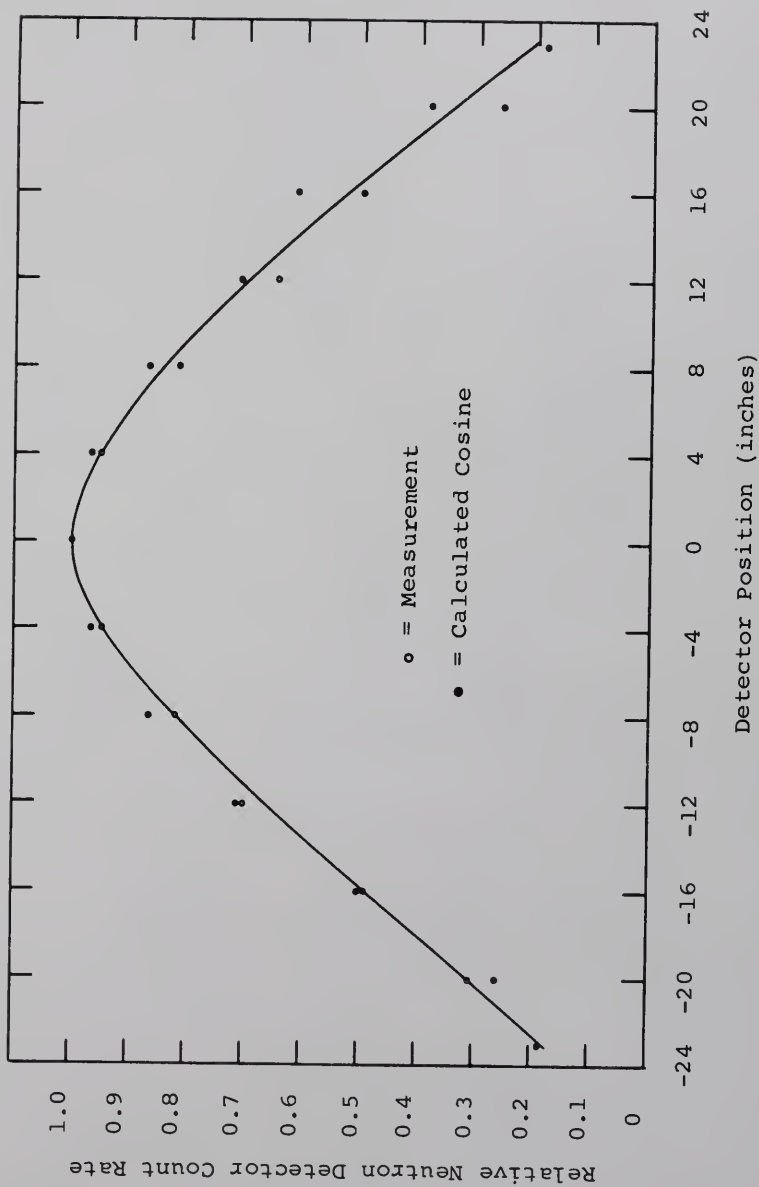
Fig. A-2. Epicadmium Flux Across the Horizontal Midline of the Graphite Face of the Thermalizing Apparatus.
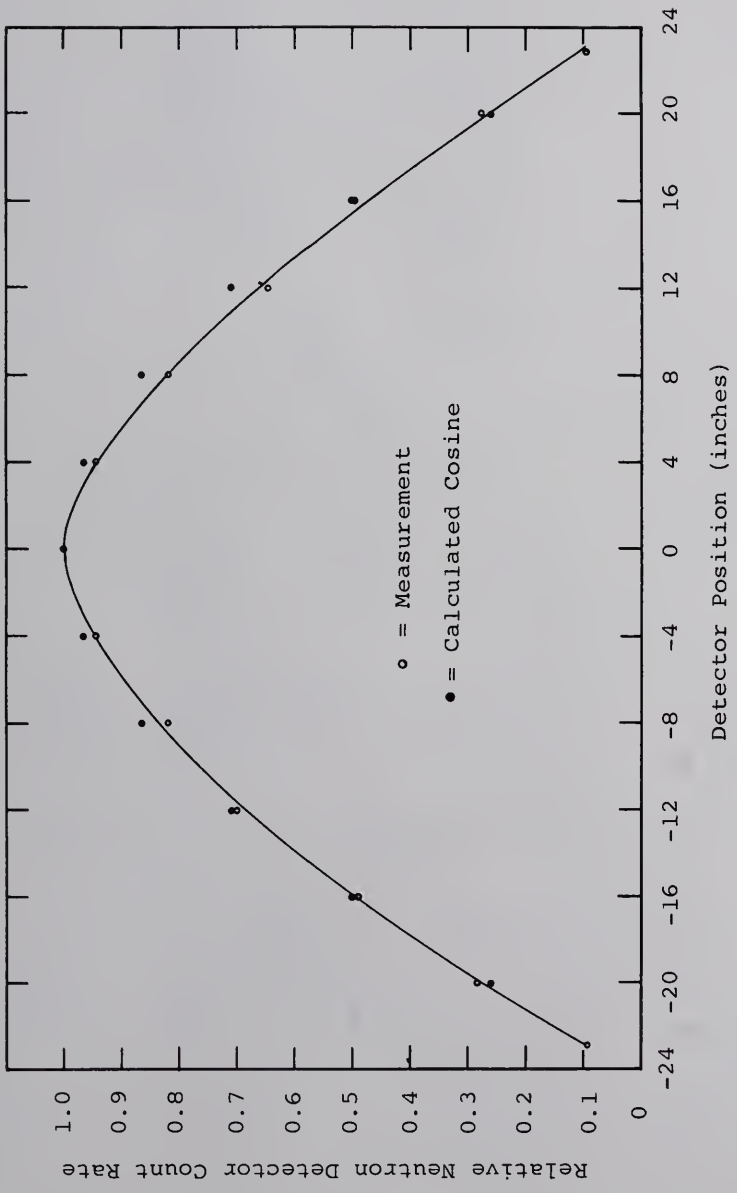
Fig. A-3. Total Flux Across the Horizontal Midline of the Graphite Face of the Thermalizing Apparatus.

APPENDIX B

DETERMINATION OF RESOLUTION TIMES
FOR NEUTRON DETECTION SYSTEMS

It was desirable to determine the resolution times of
the detection systems under the same operating conditions as
would exist during the experiment. The method used and the
results obtained are described in this section.

To determine the resolution times of the three combi-
nations of equipment described in Chapter IV, a method using
count data from two detector systems to determine the reso-
lution time of one of the two systems was applied three times.
The necessary range of neutron flux levels was provided by
the neutron generator and thermalizing apparatus. Because
the ion beam current of the neutron generator as read from
the meter on the control console was not a sufficiently accu-
rate indication of the neutron output, it was necessary to
use one of the two detector systems to determine the relative
neutron output of the generator at each flux level.

The approach involved in the resolution time determina-
tion was first to determine $(1 - F)$, and then with F known, to
use the second equation below to obtain the resolution time, τ.

193

$$1 - F = \text{(observed counts)} / \text{(correct counts)}$$

$$F = \frac{\text{(observed counts/min)} \ (\mu\text{sec/observed count})}{60 \times 10^{6} \ \mu\text{sec/min}}$$

F is the fraction of counting time lost because of the resolution time interval following each observed pulse.

Referring to two detector systems as X and Y, and letting X cpm = count rate of system X, and Y cpm = count rate of system Y, the resolution time of system X may be determined as follows: Detector Y is partially wrapped with cadmium to reduce its count rate relative to that of X, and both detectors are then placed in a thermal flux region where high count rates can be obtained. With the cadmium on Y adjusted so that X cpm $\cong$ 20Y cpm, the fractional resolution loss in the counts recorded from Y is small enough either to be ignored, or to allow the use of an assumed approximate resolution time for Y during the determination of the resolution time of X. Without disturbing the positions of the two detectors, counting data are recorded for both X and Y over a wide range of count rates for X by operating the neutron generator at different levels of beam current.

The ratio, (observed X counts) / (observed Y counts), decreases with increasing count rate because of resolution loss in X. A graph of observed X cpm plotted versus this ratio is a straight line and may be extrapolated to zero

count rate to obtain the "true" value of the ratio in the absence of resolution error. Next, resolution-corrected X counts may be obtained by multiplying the corresponding Y counts by the extrapolated ratio. Then the value of (1 - F) may be determined for each data point by the relationship:

$$1 - F = \frac{(\text{observed X counts})}{(\text{Y counts})(\text{extrapolated ratio})}$$

A graph of observed X cpm plotted versus (1 - F) for each data point may be fitted by a straight line over the range of useful count rates. Note that (1 - F) is unity for zero count rate. This graph itself is useful because (1 - F) is the resolution correction factor. Any point on the line (other than the origin) may be used to yield values of F and observed X cpm for use in the following equation, which yields τ in units of μsec per observed count.

$$\tau = \frac{6 \times 10^7 \text{ F μsec/min}}{\text{observed X cpm}}$$

Figures B-1 and B-2 illustrate the method. Figure B-1 yields an extrapolated value of 17.68 for the ratio spoken of above, and Fig. B-2 leads to a value of 1.47 μsec for the resolution time of the reference detector system shown earlier in Fig. 4-7 of Chapter IV.

Linearity to 5 x 10^6 cpm is not typical. For the other detector system used, a gradual departure from the
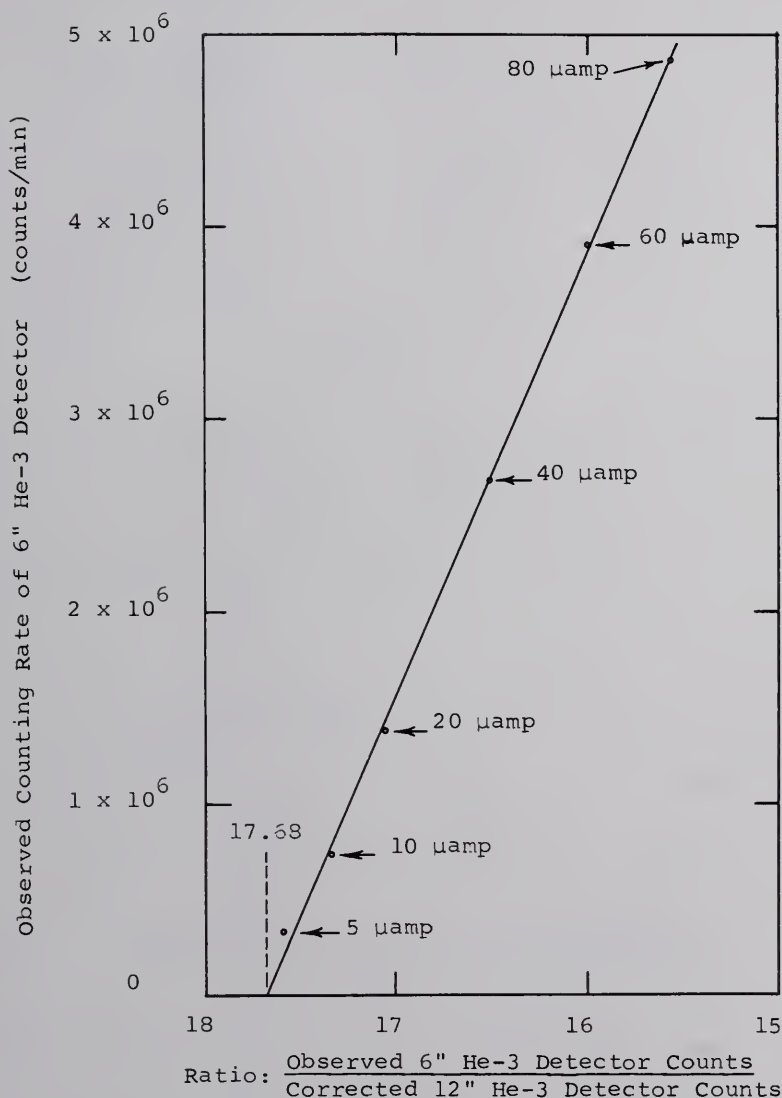
Fig. B-1. Graph Used in the Determination
of the Resolution Time for the
Reference Detector System.
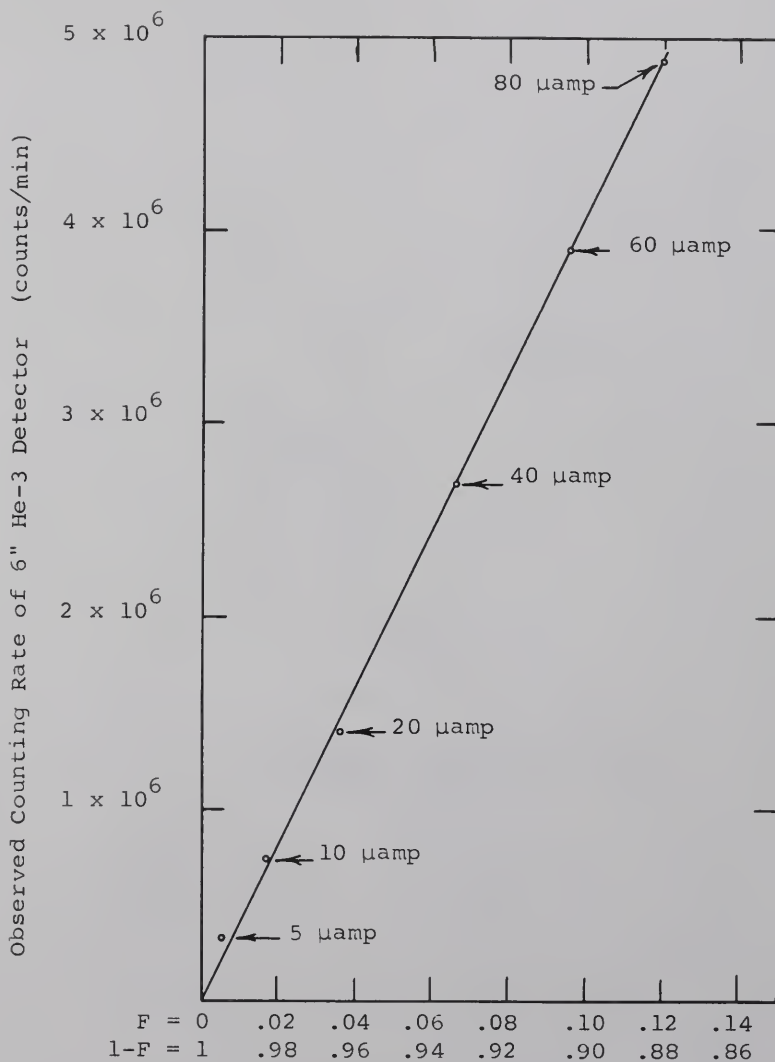
Fig. B-2. Resolution Loss Correction Factors
for the Reference Detector System.

straight line in the second graph began at about 2.3×10^6

cpm. A final observation concerning linearity seems worthy

of recording here. At first, because it seemed natural to

work with a multiplicative correction factor greater than

unity, the equation relating corrected counts to observed

counts was written in the form:

$$1 + F = \text{(correct counts)}/\text{(observed counts)}.$$

However, the graph using this form was a smooth, gradual

curve from which no single value of τ could be obtained.

The form,

$$1 - F = \text{(observed counts)}/\text{(correct counts)},$$

was found to be nearly linear, and yielded a single value of

τ fitting a wide range of count rates. The two forms are

approximately equivalent because $(1 - F) \cong 1/(1 + F)$ for $F << 1$.

APPENDIX C

A METHOD FOR DETERMINING THE RESOLUTION LOSS COR-
RECTION FACTOR FOR A DETECTOR EXPOSED TO A FLUX
FIELD WHICH VARIES IN A REPETITIVE FASHION IN TIME

As explained in Chapter V, a six-inch He-3 detector

was placed in one corner of the H_2O tank of the thermaliz-

ing apparatus and served as a standard measure of the

output from the neutron generator during both continuous

mode and pulsing mode operation of the generator. For

continuous mode runs the resolution loss correction factor

may be based directly upon the time-averaged count rate

for the run and can be read from a graph such as Fig. B-2

in Appendix B. However, for the pulsing mode of operation,

the observed time-averaged counting rate is frequently far

less than the true counting rate of the detector during the

pulse, and to base the correction factor on this average

count rate would result in a smaller correction than is

needed. To meet this difficulty, a method was devised by

which the effective counting rate, ECR, could be determined

as a function of the observed average count rate, the pulse

width, detector position, and pulse repetition rate. The

199

following nomenclature and relationships will be useful:

$CR(t)$ = Time-dependent count rate of the detector.

ACR = Time-averaged observed count rate. This is the average of $CR(t)$, and is an "observed" rather than true count rate because it contains the resolution error.

T = Run time.

TC = $\int_{0}^{T} CR(t)\, dt = (ACR)(T)$ = Total counts for a run. This quantity is recorded from a scaler after each run. It contains the resolution error.

ECR = Effective count rate. This quantity is to be determined for each run in such a way that it can be used with graphs such as in Fig. B-1 of Appendix B to obtain $(1 - F)$, ECR is also the height of ERP.

$1 - F$ = Resolution loss correction factor. $1 - F < 1$. $1 - F$ = observed count/correct count.

ERP = Equivalent rectangular pulse.

W = Width of ERP.

BF = Bunching factor. $BF = P/W$.

P = Period of pulse. P = time per trigger, time per pulse, or time per sweep. P = inverse of pulse repetition rate.

The method being discussed has as its central idea the replacement of $CR(t)$ by an equivalent rectangular pulse, ERP, with width W and height ECR such that the resolution loss of a detector reporting this rectangular pulse would be precisely the same as the resolution loss of the same detector reporting the observed $CR(t)$. See Fig. C-1. The
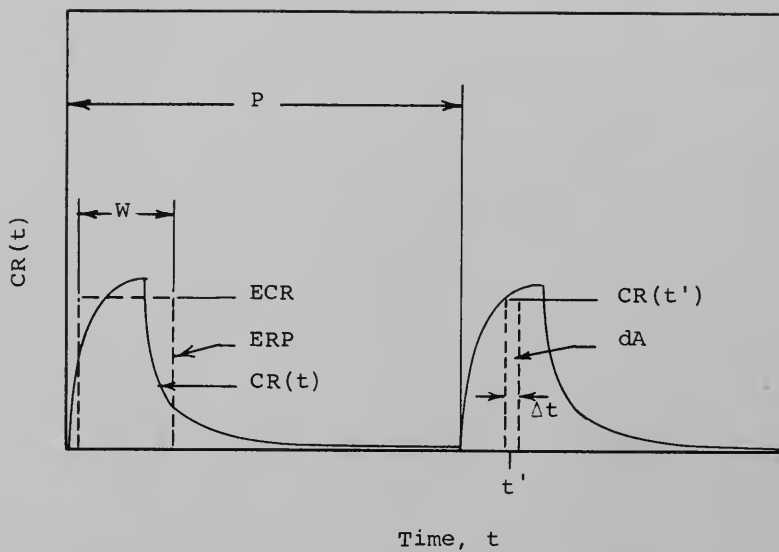
Fig. C-1.   Illustration of the Nomenclature for the Derivation of the Equivalent Rectangular Pulse.

necessary relationships between ERP and CR(t) are:

$$\int_0^P CR(t)\,dt = \int_0^P ERP\,dt = (ECR)\ (W) \qquad\qquad (C-1)$$

$$\int_0^P [CR(t)]^2\,dt = \int_0^P (ERP)^2\,dt = (ECR)^2(W) \qquad (C-2)$$

The first equation equates areas, requiring that the total

counts represented by ERP be equal to the total counts in

CR(t) over one period. The second equation makes the

resolution loss for the two shapes equal. In this connection,

refer to Fig. C-1. Note that the counts lost during Δt is

proportional to the number of counts observed during Δt

times a loss factor which is proportional to the count rate

during Δt. Or counts lost in $\Delta t = K\Delta t[CR(t')]^2$. Since the

factor K is a characteristic of the detector system, it

cancels through on both sides of Eq. C-2. K is a function

of the resolution time of the system and the units employed.

To apply the above relationships to the reference

detector system used in the experimental work, it was

necessary to determine the shape of the pulse as seen by

the detector. The 1024 channel time analyzer was used to

closely approximate CR(t) by yielding 1024 values of C_i.

Let C_i = Counts accumulated in the ith channel.

Let N = The number of channels enclosed in W, the width
of ERP.

Let $\overline{C}$ = Height of ERP in terms of counts per channel.

Then Eqs. C-1 and C-2 become:

$$\sum_{i=1}^{1024} C_i = N\overline{C} \qquad (C-3)$$

$$\sum_{i=1}^{1024} C_i^2 = N(\overline{C})^2 \qquad (C-4)$$

Since N is of greater usefulness than $\overline{C}$, eliminate $\overline{C}$ from the set to obtain:

$$\sum C_i^2 = N\left[\frac{\sum C_i}{N}\right]^2, \text{ from which } N = \frac{(\sum C_i)^2}{\sum C_i^2}$$

From the above equation can be drawn a very important conclusion: That the content of each channel may be multiplied through by any constant without changing the value of N, the width of ERP. This fact makes it possible to analyze the reference flux once and use the same value of N for all pulse runs regardless of the use of different beam currents or run times, provided the target pulse duration and reference detector position remain unchanged. N is only a function of pulse shape; not overall magnitude. The method discussed here therefore does not require the use of two analyzer systems to conduct a wave propagation experiment at flux levels for which resolution losses are significant.

Figure C-2 shows the shape of the pulse as seen by the reference detector placed in the corner of the H_2O tank, its
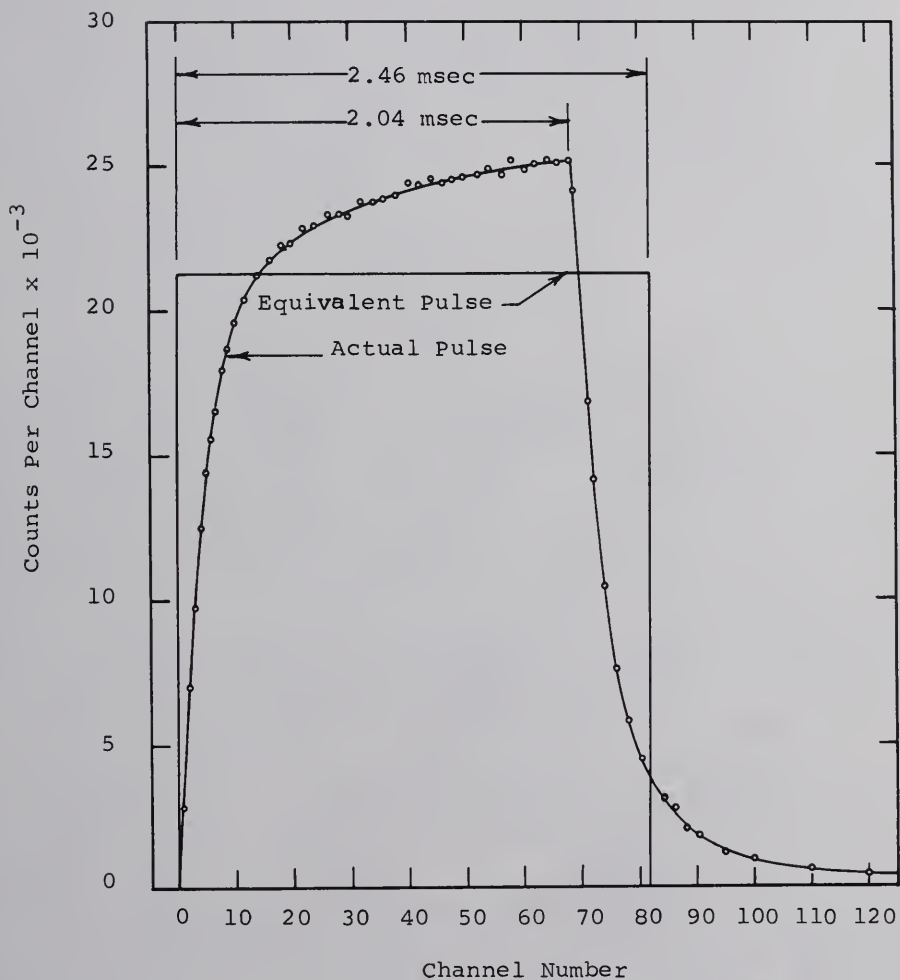
Fig. C-2. The Equivalent Rectangular Pulse
and the Actual Pulse for the
Reference Detector System.

standard position throughout the wave propagation runs. The
neutron generator was operated with a pulse width of 2 msec,
the same as used during the experiments. This width was
determined by observing the oscilloscope display of the beam
current received by the target of the neutron generator. The
pulse seen by the detector continues to rise through channel
no. 68, and then falls. For a 20 μsec channel plus a 10 μsec
storage time, the duration of the target pulse is therefore
68 x 30 μsec, or 2.04 msec. The width and height of the
associated ERP was calculated as follows, using a desk
calculator.

$$N = \frac{(\Sigma c_i)^2}{\Sigma c_i^2} \qquad \frac{(1,741,401)^2}{3,700,631 \times 10^4} = 81.9 \text{ channels}$$

$$W = (81.9)(30 \mu sec) = 2.46 \text{ msec.}$$

$$C = 1,741,401/81.9 = 21,270 \text{ counts/channel.}$$

The equivalent rectangular pulse is also plotted in Fig. C-2
for comparison with the actual pulse. The two areas must be
equal.

Figure C-3 presents the squared functions. If the
correct ERP has been found, the area under the square of $\overline{C}$
must equal the area under the square of $c_i(t)$. This require-
ment, as set forth in equations C-2 and C-4, is also satisfied.

From the above measurements, the quantity of greatest
usefulness is W = 2.457 msec, the width of the equivalent
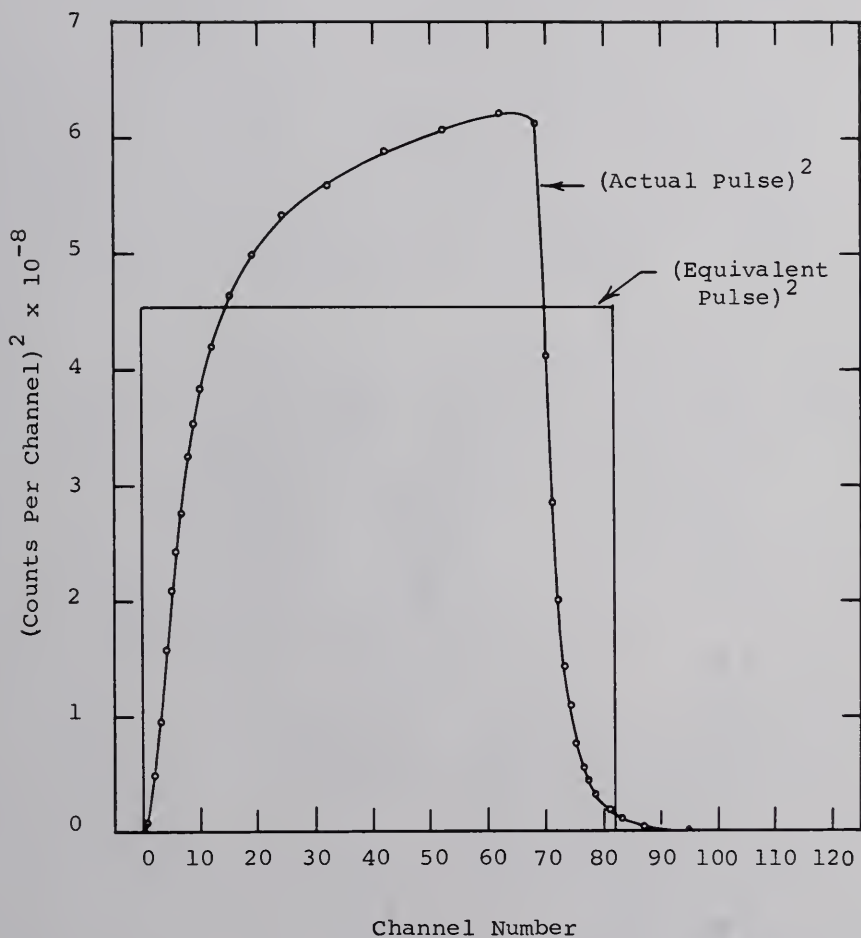
Fig. C-3. The Equivalent Rectangular Pulse
Squared and the Actual Pulse Squared
for the Reference Detector System.

rectangular pulse, a constant so long as the target pulse width and reference detector are not changed. With W known, and if the pulse width and detector position are held constant, the appropriate ECR for any pulse run may be obtained from integral count information without further use of the analyzer by use of the following relationship:

$$ECR = (ACR)(BF) = \frac{(\text{total detector counts})(\text{period of pulse})}{(\text{total run time})(W)}$$

The resolution loss correction factor $(1 - F)$ is obtained by using a graph such as Fig. 8-2 in Appendix B, and reading $(1 - F)$ for a count rate equal to ECR.

APPENDIX D

A TEST OF THE TMC ANALYZER FOR ACCURACY OF TIME DIVISION

The author was informed that certain strange results from a student laboratory experiment could be accounted for nicely if either the channel width or the storage time of the TMC Model 212 Logic Unit and Computer Unit Model CN 1024 were out of calibration. Since this equipment was used in the work with the rectangular subcritical assembly, it was considered necessary to check the time calibration.

A. Method

The method used is simple and, except for a Pu-Be source, no equipment other than that already associated with the analyzer is needed. A Pu-Be source supplies neutrons for the 12" detector system and TMC analyzer. The method makes use of a peculiarity in the performance of the analyzer: if the time between sweep triggers is less than that required for the complete sweep of that portion of the 1024 channels in use, there is an abrupt loss of counts recorded in one or two channels which are

208

open during and immediately after the trigger pulse, and a
general reduction of counts in the remaining channels. An
experimental value of time per channel may therefore be
obtained by dividing the time between triggers by the number
of channels which complete their counting before the distur-
bance created by the early-arriving trigger.

B. Procedure

Since channel width settings of 20 μsec and 40 μsec
had been used in taking data for D_2O and for the loaded
assembly respectively, the equipment was checked for these
two settings. Consider the 20 μsec case: With an additional
10 μsec storage time between channels, the total nominal time
associated with each channel is 30 μsec. Hence if the equip-
ment is functioning properly, the time required to sweep 1024
channels would be 30 μsec x 1024 = 30.72 msec. Therefore, a
trigger frequency greater than 32.55 cps should cause clip-
ping of some of the channels, as desired in this method.
For each trigger frequency used, the analyzer was run for 100
sec with the memory location knob set on position $\frac{1}{1}$ to put
the entire memory into action. However, one finds that with
this full memory setting and a trigger frequency exceeding
approximately 32.55 cps, the analyzer does not count every
trigger. (It counts about half of them.) Therefore, a

second 100 sec run was performed with the memory location
knob set on a sufficiently small portion of the memory to
allow each trigger to be counted. For this second run,
only the trigger information is used. Dividing the run
time by the number of triggers counted yields the time per
trigger. From the print-out of a channel number and content,
one finds how many channels completed counting. Finally,
division of time per trigger by channels counted between
triggers gives time per channel, which may then be compared
with the nominal channel width plus storage time. Note that
time and paper are saved by printing out only the last
quarter of the memory. But if this short cut is taken,
the channel numbers printed out for the last quarter will
begin with one, and the quantity 3 x 256 must be added to the
channel number read directly from the print-out in order to
obtain the true channel number. Table D-1 shows both ob-
served data and related calculated results.

C. Results

The analyzer is not out of calibration. Since no
interpolations can be made between channels, an error of
less than about 0.1 per cent cannot be claimed for a single
observation. However, for the 20 μsec channel width setting,
and an assumed 10 μsec between channels, one gets 30 μsec

TABLE D-1

OBSERVED DATA AND CALCULATED RESULTS FOR TEST OF TMC MULTICHANNEL ANALYZER

| | Observed Data Taken August 4, 1964 | | | | Values Calculated From Observed Data | | |
Nom. Chan. Width (μsec)	Run Time (sec)	Freq.* Dial (cps)	No. of Observed Triggers	Channels Completed Between Triggers	Trig. Per sec. (cps)	Time Per Trig. (msec)	Time** Per Channel (μsec)
20	100	20.0	3212	All	32.12	31.13	----
20	100	21.0	3311	1008	32.11	30.20	29.96
20	100	22.0	3407	978	34.07	29.35	30.01
20	100	23.0	3505	950	35.05	28.53	30.03
20	100	20.4	3253	All	32.53	30.74	----
20	100	20.7	3282	1015	32.82	30.47	30.02
20	100	20.5	3268	1021	32.68	30.60	29.97
20	100	20.6	3274	1018	32.74	30.54	30.00
20	100	20.8	3291	1013	32.91	30.39	30.00
20	100	20.45	3268	1020	32.68	30.60	30.00
20	100	21.0	3313	1006	33.13	30.18	30.00
20	100	. . .	. . .	. . .	Average time per channel = 30.00 ± 0.02		
40	100	7.0	1964	1018	19.84	50.92	50.02 ± 0.05

* The frequency dial setting is given for reference only. It is not an accurate indication of trigger pulse frequency.

** This column is obtained by dividing (msec/trig.) by (channels/trig.).

per channel, which compares well with the experimental results of 30 ± 0.02 µsec. For the single measurement with the 40 µsec channel width setting, the calculated value of 50 µsec compares well with the experimental value of 50.02 ± .05 µsec. Reliability of the method is demonstrated by 9 measurements for the 20 µsec setting. Only one measurement is really necessary, as shown in the test on the 40 µsec setting.

Note that the trigger frequency as read from the frequency dial setting is in error 50-100 per cent for the above settings, and is given for reference only.

APPENDIX E

CALCULATION OF LATTICE PARAMETERS

It was necessary to calculate certain basic lattice
parameters before use could be made of the two-group equations
of Chapter II or the age-theory equations of Chapter III.
The calculations for these parameters and others are presented
in this section in sufficient detail so that future users of
the subcritical assembly may know how these parameters were
obtained, and may thereby have a better basis upon which to
decide whether to use the same values for their purposes, or
to compute them again by some other method. A significant
change in moderator purity or in lattice spacing, for ex-
ample, would necessitate a new calculation.

In brief, two computer codes were employed. CEPTR (29)
was used to compute average fluxes for various regions of
the lattice unit cell. These average values were needed as
part of the input to the BUCKSHOT code (30), by which most
of the parameters of interest were obtained. Therefore,
this section is organized largely in terms of input and out-
put of these two codes.

The basic dimensions of the fuel slugs are presented in the following table.

TABLE E-1

BASIC NOMINAL DIMENSIONS OF FUEL SLUGS

Diameter of Uranium	1.000	in
Length of Uranium	8.000	in
Outside Diameter of Uranium Slug	1.0625	in
Outside length of Slug	8.40	in
Thickness of Side Cladding	0.03125	in
Thickness of Cladding End Plugs (Approximate)	0.20	in

The unit cell has a square pitch of 4.35", and a length of 8.40". The length of the cell was selected to enclose one entire fuel slug and its corresponding length of aluminum fuel tube of 1.25" OD and 0.049" wall thickness. The lattice pitch was computed by dividing the undistorted inside dimension of the tank by the number of fuel tubes across that width: 47.87/11 = 4.3518". Volumes of the various core materials based on this unit cell are presented in the following table.

TABLE E-2

CALCULATED VOLUMES AND
VOLUME RATIOS BASED ON THE UNIT CELL

Total Volume of Unit Cell	159.081 in^3
D_2O Volume Per Unit Cell	150.080 in^3
Total Volume of One Fuel Slug	7.448 in^3
Volume of Uranium Per Slug	6.283 in^3
Total Volume of Aluminum Per Unit Cell	2.718 in^3
Volume of Aluminum Fuel Tube 8.40 in long	1.553 in^3
Volume of Aluminum Radial Cladding Per Slug	0.850 in^3
Volume of Two Aluminum End Plugs (End Cladding)	0.314 in^3
Total Volume of Aluminum Cladding Per Slug	1.165 in^3
Volume of Uranium / Volume of Unit Cell	0.03950
Volume of Aluminum / Volume of Unit Cell	0.01708
Volume of D_2O / Volume of Unit Cell	0.94342
Volume of D_2O / Volume of Uranium	23.886

Note that the result of 23.886 above is literally the
moderator-to-fuel volume ratio, with the aluminum counted as
neither moderator nor fuel. This figure does not agree with
that ratio computed by BUCKSHOT because BUCKSHOT counts the
fuel slug cladding and plugs in with the fuel volume.

The method by which this error was taken into account is presented later in this section.

Since CEPTR was written for cylindrical geometry, it was necessary to compute the radius of a cylindrical unit cell equivalent to the actual square unit cell. By requiring that the cylindrical cell have the same area as the actual square unit cell, the radius of the cell was found to be 2.4552".

Similarly, since BUCKSHOT was written principally for the case of cylindrical fuel rods arranged in a hexagonal array, the input to this code calls for the triangular lattice pitch, and the code computes volume ratios on the assumption that the fuel rods are located at the corners of equilateral triangles. A study of the geometry reveals that if P is the pitch of the square array, and P' is the triangular pitch of a hexagonal array having the same volume ratios, the relationship between P and P' is:

$$2P^2 = (3)^{0.5}(P')^2$$

By setting P equal to 4.3518", P' is found to be 4.678". The same result can be obtained by dividing the radius of the equivalent cylindrical cell by the constant, 0.5240.

Reference 31 was the source of the information in the first four columns of Table E-3. This reference also states that the density of 6061-T6 is 0.098 lbs/in^3, from which the

TABLE E-3

CROSS SECTION CALCULATION FOR 6061-T6 ALUMINUM FOR 2200 METER/SEC NEUTRONS

Element	Nom. Wt.%	Min. Wt.%	Max. Wt.%	Σ_a cm^{-1}	Density gm/cm^3	Volume Fraction Nominal	Volume Fraction Maximum Impurities	Σ_a x Volume Fraction Nominal	Σ_a x Volume Fraction Maximum Impurities
Si	0.6	0.40	0.80	0.008	2.42	0.00672		0.0000538	
Fe			0.70	0.222	7.86		0.002415		0.000536
Cu	0.25	0.15	0.40	0.326	8.94	0.000758		0.0002470	
Mn			0.15	1.04	7.2		0.000566		0.000589
Mg	1.0	0.80	1.20	0.003	1.74	0.0156		0.0000468	
Cr	0.25	0.15	0.35	0.255	7.1	0.00077		0.0001963	
Zn			0.25	0.072	7.14		0.000774		0.000056
Ti			0.15	0.119	4.5		0.000904		0.000108
Others (each)			0.05						
Others (total)			0.15	0.5 (guessed)		Approx. 0.00058		Approx. 0.000290	
Al	97.5 nominal			0.015	2.699	0.984	0.01476	0.01476	
							Totals:	0.015304	0.00158

density in grams/cm^3 was found to be 2.71. The basic cross
section information in the table was taken from ANL 5800,
and is for 2200 m/sec neutrons. Several problems arise in
making such calculations for a commercial alloy, principally
because the composition is not known exactly. It is well to
understand that though Si, Cu, Mg, and Cr are the only
alloying elements which are deliberately added to the alumi-
num to make the alloy; Fe, Mn, Zn, Ti, and other unnamed
elements are present in amounts up to the maximum weight
per cent listed. Note in Table E-3 that Si, Cu, Mg, and Cr
are not necessarily present in the amounts listed in the
nominal composition column, but have the maximum and minimum
concentrations listed. The absorption cross section for
"others" is, of course, merely a guess.

The contents of Table E-3 were used to produce Tables
E-4 and E-5. Table E-4 presents the results on the unlikely
assumption that the impurities are present in the maximum
allowable amounts, thereby establishing an upper limit to
the absorption cross section of the alloy within the accuracy
of the assumed values for "other" elements. Table E-5 pre-
sents the results on the more reasonable assumption that the
impurities, both named and "other," are present in amounts
equal to one third of the maximum allowable amounts. In
this section, the term, "impurity," refers to elements not
present in the nominal composition of the alloy.

TABLE E-4

2200 METER/SEC CROSS SECTIONS FOR 6061-T6 ALLOY ON THE ASSUMPTION
THAT IMPURITIES ARE PRESENT IN THEIR MAXIMUM ALLOWABLE QUANTITIES

Element	Amount of Element	Σ_a x Volume Fraction	
		Expressed In Cm^{-1}	Expressed In Per Cent
Aluminum	Nominal Amount in Table E-3	0.01476	87.4
Si, Cu, Mg and Cr	Nominal Amount in Table E-3	0.000544	3.22
Fe, Mn, Zn and Ti	Maximum Amount in Table E-3	0.00129	7.68
Others – Total	Maximum Amount in Table E-3	0.00029	1.72
	Totals:	0.01687	100.0

Table E-4 shows that the maximum impurities in 6061-T6 increase the absorption cross section by about 10 per cent over that of the nominal alloy, and for the case presented in Table E-5, the impurities add about 3.3 per cent to the absorption cross section. From this second, more realistic case, one may conclude that the penalty paid in the use of this alloy is not excessive since the absorption cross section is only about 7 per cent greater than that of absolutely pure aluminum.

Next, attention will be given to the problem presented by the presence of aluminum cladding on the ends of the fuel slugs. Both CEPTR and BUCKSHOT treat cylindrical geometry, looking upon the unit cell as being of infinite length. All fuel dimensions enter the code in terms of radial dimensions; hence there is no provision for taking axial inhomogeneity into account. The presence of two end plugs, each approximately 0.2" thick, on a slug 8.4" long, reduces the fuel present by the factor: $(8.4 - 0.4)/(8.4) = 0.952$. Therefore, to ignore the presence of the aluminum end plugs would result in an error of about 5 per cent in the quantity of fuel. This error would be reflected in the moderator-to-fuel ratio. To correct for this situation, two basic steps were taken:

TABLE E-5

2200 METER/SEC CROSS SECTIONS FOR 6061-T6 ALLOY ON THE ASSUMPTION THAT
IMPURITIES ARE PRESENT IN ONE THIRD OF THEIR MAXIMUM ALLOWABLE QUANTITIES

Element	Amount of Element	Σ_a x Volume Fraction	
		Expressed In Cm^{-1}	Expressed In Per Cent
Aluminum	Nominal Amount in Table E-3	0.01476	93.2
Si, Cu, Mg and Cr	Nominal Amount in Table E-3	0.000544	3.44
Fe, Mn, Zn and Ti	One Third Max. Amount in Table E-3	0.00043	2.72
Others – Total	One Third Max. Amount in Table E-3	0.000097	0.61
	Totals:	0.01583	100.0

1. The aluminum of the end plugs was added to the
    radial fuel cladding and to the aluminum fuel tube.

2. The 8.0" uranium slug was spread over the full 8.4"
    length of the clad slug by reducing the density of
    the uranium by the factor 0.952.

In keeping with the reduction in density, all macro-
scopic cross sections for the uranium were reduced by multi-
plication by 0.952. To accomplish step (1) above without
reducing the amount of volume left for the moderator, the
extra aluminum was added to the radially distributed
aluminum by, in effect, packing it into the volume already
occupied by the cladding and the fuel tube. This called for
an appropriately estimated increase in the cross sections
for the aluminum occupying that volume. The computation of
the cross sections takes several facts into account:

1. The cladding and fuel tubes are of different alloys.

2. The end plug cladding is in a region of relatively
    low flux.

3. BUCKSHOT assumes that the cladding aluminum and
    the aluminum of the fuel tube have the same cross
    sections, and has provision for reading in only
    one set of cross sections for all the aluminum
    in the problem.

4. The fictitious cross sections should be such as to
    produce the same number of absorption and scattering
    events per unit time for the geometry assumed by
    the code as occur in the actual existing geometry.

Item (1) above made it necessary to compute the cross
sections for the cladding alloy, for which, unfortunately,

only the nominal composition is known. See Table E-6.
Items (2) and (4) require either a guess or a preliminary
computation of the flux depression in the fuel relative to
that on the surface of the fuel and in the fuel tube.
This information was obtained by doing a calculation with
CEPTR in which the end plug problem was ignored. This
preliminary CEPTR calculation yielded a volume-averaged
flux in the fuel region equal to 81.5 per cent of the
volume-averaged flux in the aluminum cladding and fuel tube
regions. It was assumed that the radial flux distribution
in the end plugs is approximately the same as in the fuel.
This assumption seems reasonable since the thickness of
two adjacent end plugs is considerably less than the
diameter of the uranium slug.

The calculation of the required fictitious aluminum
cross sections is carried out in Table E-7, where the
volume and flux-weighted macroscopic cross sections for
the three aluminum regions are first added together, and
then divided through by the sum of the volume of the radial
cladding and the volume of the fuel tube. The final results
are: Σ_a = 0.0162, and Σ_s = 0.114. Both values are about
10 per cent higher than the true cross sections for the
alloy.

TABLE E-6

CROSS SECTION CALCULATION FOR FUEL SLUG CLADDING ALLOY
FOR 2200 METER/SEC NEUTRONS AND FOR NOMINAL ALLOY COMPOSITION

Element	Nominal Wt. %	Density Gm/cm^3	Σ_a Cm^{-1}	Σ_s Cm^{-1}	Calculated Values		
					Volume Fraction	Σ_a x Vol. Fraction	Σ_s x Vol. Fraction
Silicon	0.20	2.42	0.008	0.089	0.00226	0.000018	0.000201
Iron	0.58	7.86	0.222	0.933	0.00201	0.000447	0.00188
Copper	0.10	8.94	0.326	0.611	0.000306	0.000100	0.000187
Nickel	1.10	8.90	0.420	1.60	0.00337	0.001415	0.00540
Aluminum	98.02	2.699	0.015	0.084	0.9920	0.01488	0.0833
				Totals:	1.000	0.01686	0.0910

TABLE E-7

CALCULATION OF FICTITIOUS CROSS SECTIONS FOR ALUMINUM FOR USE IN CEPTR AND BUCKSHOT CODES IN ORDER TO ACCOUNT FOR PRESENCE OF END CLADDING ON SLUGS

Region	Volume In^3	Average Flux, ϕ	For 2200 m/sec Neutrons			
			Σ_s	Σ_s	Vol. times $\phi\Sigma_a$	Vol. times $\phi\Sigma_s$
Fuel Tube, 6061-T6	1.553	1.0	0.0158	0.0863	0.0246	0.134
Radial Cladding	0.850	1.0	0.0174	0.091	0.01476	0.0773
End Plugs	0.314	~0.815	0.0174	0.091	0.00445	0.0233
				Totals:	0.0438	0.235

Effective Σ_s = (0.235)/(1.55 + 0.850) = 0.0976   For 2200 m/sec neutrons

Effective Σ_a = (0.0438)/(1.55 + 0.850) = 0.0182   For 2200 m/sec neutrons

Correct the above for 1/v absorption, assuming a Maxwellian distribution:

Effective Σ_a = 0.0182 / 1.128 = 0.0162 Σ_t = 0.0162 + 0.0976 = 0.114

It should also be explained that the quantity, 0.0174, for Σ_a of the cladding alloy in Table E-7, was obtained by adding an assumed 0.0005 to the 0.01686 result in Table E-6. The quantity, 0.0005, is an estimate of the effect of unnamed impurities in the cladding alloy.

Reference 32 was used to obtain much of the information in Table E-8. The equations by which Σ_{s0}, Σ_{s1} and Σ_{s2} were calculated for D_2O are given below. M and N are the fractional concentrations of D_2O and H_2O respectively.

$$\Sigma_{s0} = .4637 \, M + 3.196 \, N$$

$$\Sigma_{s1} = .0665 \, M + 1.023 \, N$$

$$\Sigma_{s2} = .00432 \, M + .153 \, N$$

Table E-9 gives the dimensions of the regions into which the unit cell was divided for use in the CEPTR code. Table E-10 gives the information contained on the data cards used with the final CEPTR calculation.

The average scalar fluxes for the 5 regions of the unit cell as calculated by CEPTR are given in Table E-11, and the spatial variation of the scalar flux is presented in Fig. E-1. For these calculations, the moderator temperature and purity were taken to be 20° C and 99.62 per cent, respectively.

The remainder of Appendix E will deal with the use of BUCKSHOT. This code was written by R. Razminas, and uses

TABLE E-8

CROSS SECTIONS FOR USE IN CEPTR CODE

Material and Condition	Σ_t	Σ_{so}	Σ_{s1}	Σ_{s2}	Σ_{s3}
Uranium of Normal Density	0.7197	0.3970	0	0	0
Uranium of Density Reduced By the Factor, 0.952.	0.687	0.378	0	0	0
D_2O 99.8% at 20 Degrees	0.469227	0.469165	0.068413	0.0046174	0
D_2O 99.62% at 20 Degrees	0.474203	0.474080	0.070135	0.0048840	0
D_2O 99.3% at 20 Degrees	0.482996	0.482826	0.073195	0.0053608	0
Aluminum Cladding Alloy	0.1039	0.0901	0	0	0
Aluminum Adjusted Values To Account For End Plugs	0.11375	0.0986	0	0	0

TABLE E-9

REGIONS INTO WHICH THE UNIT CELL WAS DIVIDED FOR USE IN CEPTR CODE

Region Number	Material	Outer Radius cm	Radial Thickness cm	Number of Intervals In Region	Mesh Thickness cm
1	Uranium	1.27	1.27000	20	0.06350
2	Aluminum Cladding	1.34937	0.07937	4	0.0198425
3	D_2O	1.46305	0.11368	4	0.02842
4	Aluminum Fuel Tube	1.5875	0.12445	4	0.0311125
5	D_2O	6.2357	4.64820	40	0.116205
		Total:	6.23570	72	

TABLE E-10

DATA CARDS USED WITH CEPTR CALCULATION FOR SUBCRITICAL ASSEMBLY

Columns	
3-72	CEPTR CALCULATION FOR RECTANGULAR D2OSUBCRITICAL ASSEMBLY JHD CEPTR
1-13	01+05+2+0+072
1-37	02+01+020+.0635000E+00+.00000000E+00
1-72	03+.68600000E+00+.37800000E+00+.00000000E+00+.00000000E+00
1-37	04+02+004+.01984250E+00+.00000000E+00
1-72	05+.11375000E+00+.09860000E+00+.00000000E+00+.00000000E+00
1-37	06+03+004+.02842000E+00+.10000000E+01
1-72	07+.47420327E+00+.47408000E+00+.07013500E+00+.00488400E+00+.00000000E+00
1-37	08+04+004+.03111250E+00+.00000000E+00
1-72	09+.11375000E+00+.09860000E+00+.00000000E+00+.00000000E+00
1-37	10+05+040+.11620500E+00+.10000000E+01
1-72	11+.47420327E+00+.47408000E+00+.07013500E+00+.04884003+00+.00000000E+00

TABLE E-11

AVERAGE SCALAR FLUX FOR REGIONS
OF THE UNIT CELL AS CALCULATED BY CEPTR CODE

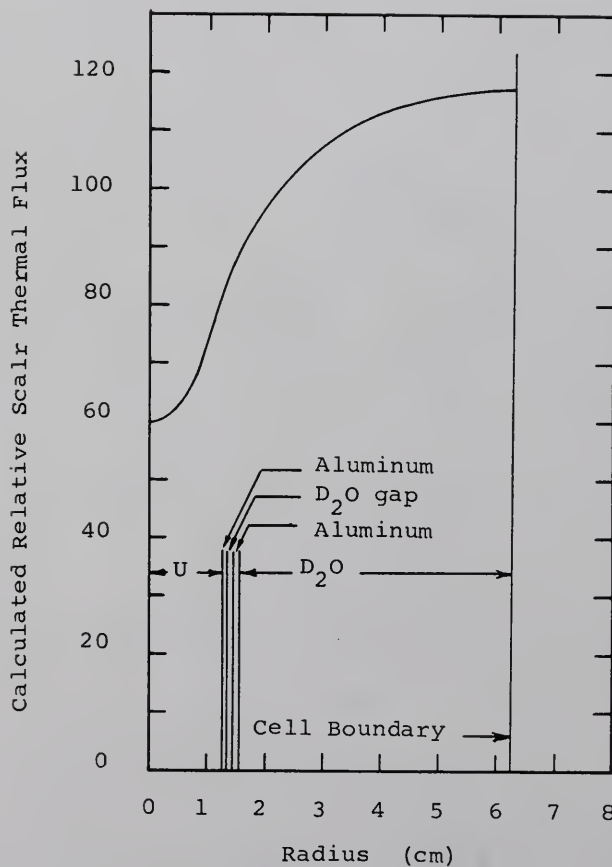| Region	Relative Average Scalar Flux
1	70.903
2	83.906
3	85.946
4	88.156
5	112.32
Entire Unit Cell	110.00

Fig. E-1. Relative Scalar Thermal Flux for
the Equivalent Cylindrical Unit
Cell Calculated by the CEPTR Code.

recipes employed at the Savannah River Laboratory to calcu-
late reactor parameters of lattices using natural uranium
and heavy water. The equations were developed in close
association with experimental work, and one may expect
their use to result in reasonably accurate values.

The equations by which the calculations are performed
in the code are valid for solid or hollow uranium fuel slugs,
but the input format is specialized for hollow slugs, and
it is necessary to look upon the solid slugs as hollow
slugs in which the hole and internal radial cladding are
of zero dimensions. Moderator is assumed to fill the hole.
Beginning with the axis of the slug, one must assume that
region 1 is moderator, region 2 is cladding, and region 3
is fuel. The fuel <u>must</u> be in region 3. See Table E-12.
The cross section information read in for the inner
cladding is assumed to apply also to the fuel housing tube,
if any.

The cross sections obtained for CEPTR were also appro-
priate for BUCKSHOT, except for the P-3 scattering cross
sections which were employed by CEPTR but not by BUCKSHOT.
As before, the aluminum cross sections were increased some-
what to take the end cladding into account, and the uranium
was looked upon as having reduced density.

Tables E-13 and E-14 complete this appendix.

TABLE E-12

REGIONS INTO WHICH THE UNIT CELL
WAS DIVIDED FOR USE IN BUCKSHOT CODE

Region No.	Material	Outer Radius (cm)
1	None	0
2	None	0
3	Natural Uranium	1.27
4	Aluminum Cladding	1.34937
5	D_2O Gap	1.46305
6	Aluminum Fuel Tube	1.5875
7	D_2O	6.2357

TABLE E-13

IDENTIFICATION OF INFORMATION ON INPUT CARDS FOR BUCKSHOT CODE

Card No.	Content of Card
1	Outer radii for regions 1 - 4.
2	Outer radii for regions 5 - 7.
3	Average thermal fluxes for regions 1 - 4.
4	Average thermal fluxes for regions 5 - 7.
5	Macroscopic absorption cross sections for regions 1 - 3, (D_2O, Al, U) and $T^\circ C$.
6	Diffusion coefficients for regions 1 - 3, and atomic weight of aluminum.
7	Macroscopic scattering cross sections for regions 1 - 3, and atomic wt. of U.
8	Resonance cross section for D_2O, and for U.
9	Molecular fraction of H_2O in moderator. Constants A, A3, and A4.
10	η for natural uranium, and control constants, L, K, and M.

TABLE E-14

DATA CARDS USED WITH BUCKSHOT CALCULATION FOR SUBCRITICAL ASSEMBLY

```
0000000001111111111222222222233333333334444444444555555555566666666667777
1234567890123456789012345678901234567890123456789012345678901234567890123456789012
```

Card No.				
1	0.0 E+00	0.0 E+00	1.27 E+00	1.34937 E+00
2	1.46305 E+00	1.5875 E+00	6.2357 E+00	4.678 E+00
3	0.0 E+00	0.0 E+00	7.0903 E+01	8.3906 E+01
4	8.5946 E+01	8.8156 E+01	1.1232 E+02	
5	1.0327 E-04	0.01615 E+00	0.3070 E+00	0.23 E+02
6	0.8269 E+00	2.9500 E+00	0.4870 E+00	2.696 E+01
7	0.47408 E+00	0.09760 E+00	0.378 E+00	2.3807 E+02
8	0.262616E+00	0.489 E+00	0.1192 E+00	1.80 E+01
9	0.3800 E-02	0.875 E+00	0.50000 E+00	-1.66666 E-01
10	1.3270 E+00	0 0	0	

APPENDIX F

CONVENTIONAL DIE-AWAY MEASUREMENTS FOR D_2O

The last measurements performed on the D_2O moderator before the tank was emptied in preparation for the loading of the fuel into the core were conventional die-away measurements using a fast neutron pulsed source. The thermalizing apparatus was rolled away, and the neutron generator was moved forward so that the target end came almost in contact with the middle of the end of the tank. The target itself was therefore outside the tank, on the Z axis at about $Z = -5$ cm. All boundary surfaces of the medium were covered with cadmium. (The shutter was down.) The water temperature was approximately $23°$ C, and the D_2O was 99.5 ± 0.1 per cent.

The neutron generator was adjusted for a beam current of 1.5 μamp, a pulse width of 10 msec, and a repetition rate of 13.6 cps. The analyzer channel width was 40 μsec, not including the 10 μsec storage time between channels. The run lasted 10^4 sec (or 166.7 min or 136,066 triggers), resulting in a maximum of 132,000 counts in the peak channels.

The long run time supplied high counts also in the portion of the pulse from which the decay constant was computed; with 51,000 in channel 334, and the minimum of 1,850 in channel 500.

The detector system was as described in Fig. 4-6, except for the use of a 6" He-3 detector instead of the 12" detector indicated in that figure. For the results presented here, the detector was submerged to mid-depth of the tank at Z = 75 cm. Trial measurements had been made with the detector at other Z positions, both closer to the source and farther from it, and in the middle of the tank, but the 75 cm position resulted in a decay curve which established a constant slope more rapidly than was the case for other positions. With the detector closer to the source, the decaying pulse approached a constant slope after decaying too rapidly for awhile. With the detector too far from the source, the opposite was true: The pulse decayed more and more rapidly until it approached a constant slope after a considerable loss of amplitude. With the detector at 74 cm, a satisfactory compromise between the two situations was obtained.

For the 75 cm position, a least squares fit to the analyzer data was performed through the use of a computer code which corrected for resolution loss channel-by-channel, and subtracted a background based on an average calculated

from channels 785 through 1024.[1] A separate least squares
fit was performed for each of 13 "channel chops" within the
range of channels 334 to 500, and the results of all 13
calculations were as follows:

Decay Constants, (sec^{-1}): From   399.605   to   400.989

Chi Square Test Results: From   0.9400   to   1.049

Correlation Coefficients: From   0.999897   to   0.999942

The statistical tests show an unusually close agreement
between the data and the fitted line. Although the results
above might justify a claim of a 0.25 per cent error in the
decay constant, the result will be quoted with a 1 per cent
error, in view of the fact that experience with similar
experiments has shown that the dependence of results upon
detector position is difficult to eliminate.[2] The decay
constant is therefore 400 ± 4 sec^{-1}.

---

[1] The data analysis was performed by Nils J. Diaz.

[2] Private communication with Nils J. Diaz.

APPENDIX G

CONVENTIONAL PULSE MEASUREMENTS IN THE SUBCRITICAL ASSEMBLY FOR SEVERAL DIFFERENT WATER LEVELS

Following the measurements described in Appendix F, the D_2O tank was drained and dried, and the full fuel loading was installed for the first time. In the interest of safety, the filling of the fueled tank with D_2O was performed in steps, and pulse die-away measurements were made at several different moderator levels. As expected, the assembly proved to be safely subcritical with the full (and optimum) lattice.

The measurements and results will be described here because they may be used to furnish a rough experimental value of the prompt critical geometrical buckling of the assembly, and because it would be possible for some inter-ested party to subject the experimental decay constants and buckling values to further analysis to obtain certain other parameters characteristic of the assembly. This is especially so if the results from Appendix F are used in conjunction with these.

The thermalizing apparatus was not in use. The target

239

position, cadmium placement, detector system, water temper-
ature and water purity were the same as given in Appendix F.
The detector was at Z = 75 cm, and at mid-depth of the
moderator.

Table G-1 gives the results of measurements and calcu-
lations for five different water levels. The decay constants
were computed through the use of the SIMPLE ALPHA code fit of
the channel data (after subtraction of background which
included the delayed neutrons) to a single exponential.

Figure G-1 shows a graph of decay constant versus the
geometric buckling of the moderated portion of the core.
The curve may be extrapolated to a rough estimate of the
prompt critical geometrical buckling for the lattice.

TABLE G-1

DATA AND RESULTS FOR PULSE MEASUREMENTS
IN THE SUBCRITICAL ASSEMBLY AS A FUNCTION OF MODERATOR LEVEL

Water Level (inches)	Run Time (sec)	Pulse Width (msec	Beam Current (μamp)	Number of Triggers	Pulse Rate (cps)	Geometric Buckling	Decay Constant* (sec⁻¹)	
10.0	1682.6	2.0	4.5	37,496	22.4	130.44	2887 ±	60
20.5	2004.9	2.0	2.5	44,948	22.4	48.28	1272 ±	25
30.0	2199.6	2.0	1.5	49,215	22.4	27.16	779 ±	16
40.0	2004.6	2.0	0.8	44,887	22.4	20.72	560 ±	11
47.9	3510.0	10.0	1.0	48,138	13.7	18.09	465 ±	9

* Calculated by Nils J. Diaz, using the SIMPLE ALPHA code.
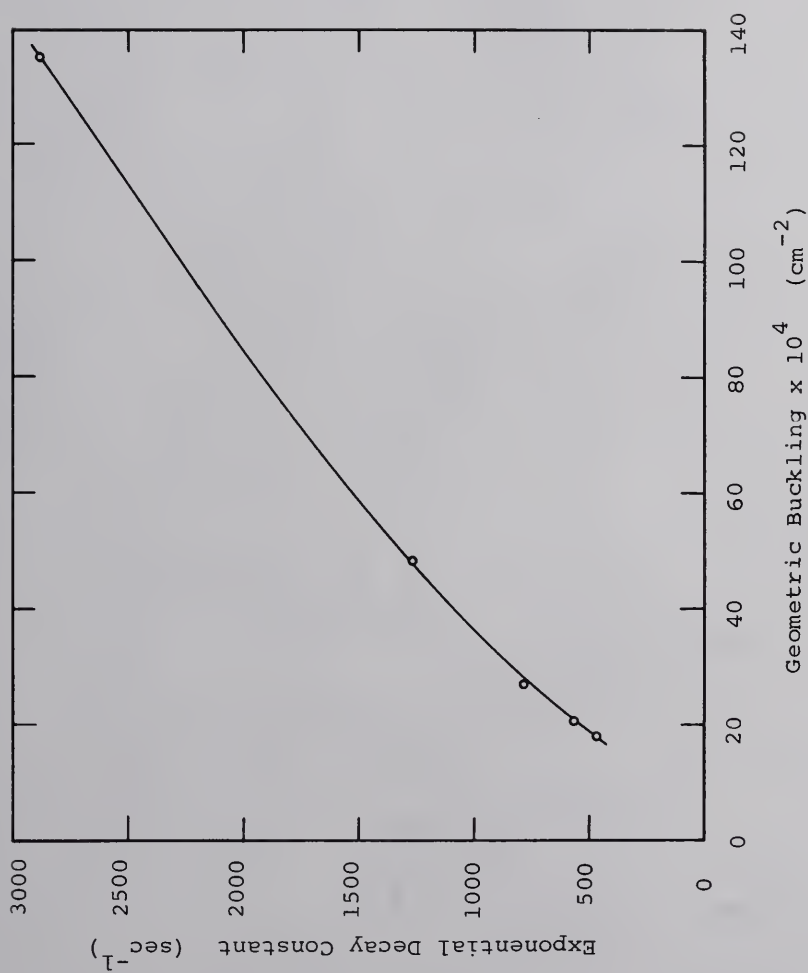
Fig. G-1. Decay Constant Versus Geometric Buckling for the Sub-
critical Assembly with Various Moderator Levels.

EXACT SOLUTION TO THE AGE-THEORY
EQUATIONS BY A SEMIGRAPHICAL METHOD

In this section the semigraphical method introduced in Chapter III will be illustrated in detail through a calculation of α and ξ as functions of frequency for a subcritial assembly described by the parameters in Table H-1.

TABLE H-1

VALUES OF PARAMETERS FOR THE SUBCRITICAL ASSEMBLY
USED IN THE SOLUTION OF THE AGE-THEORY EQUATIONS
BY THE SEMIGRAPHICAL METHOD

Parameter	Value	FORTRAN Symbol Used in Table H-4
B^2	1.2616×10^{-3} cm^{-1}	BT2
$k_\infty / \epsilon L^2$	1.087×10^{-2} cm^{-2}	F1
τ	1.2753×10^{2} cm^{2}	TAU
L_s	4.6×10^{-5} sec	ELSLO
D	1.641×10^{5} cm	D

Note that these parameters are not all identical to those listed earlier for the subcritical assembly used in the experimental portion of this work, and the numerical results obtained differ from those given earlier for that reason.

Values of B_r^2 and B_i^2 which satisfy both equations 3-4 and 3-5 for a particular value of ω were obtained by plotting B_r^2 versus B_i^2 for each of the two equations for various values of ω, and observing the points of intersection. For a given ω, the coordinates of the point of intersection are solutions to both equations.

Figure H-1 presents these graphs for 0, 50, 100, 200, and 300 cps. Figures H-2 and H-3 deal with 400, 600, 800, and 1000 cps. The technique by which these graphs were constructed is described later in this section. The coordinates of the intersections for these frequencies are presented in Table H-2 along with the corresponding values of $(\alpha^2 - \xi^2)$, $2\alpha\xi$, α, and ξ, all as functions of ω.

In the above description of the method of solution, nothing was said about how points on the graphs in Figs. H-1, H-2, and H-3 were calculated. These details will occupy the remainder of this section.

Equations 3-4 and 3-5 were rewritten as follows, for greater convenience in the computer program used.
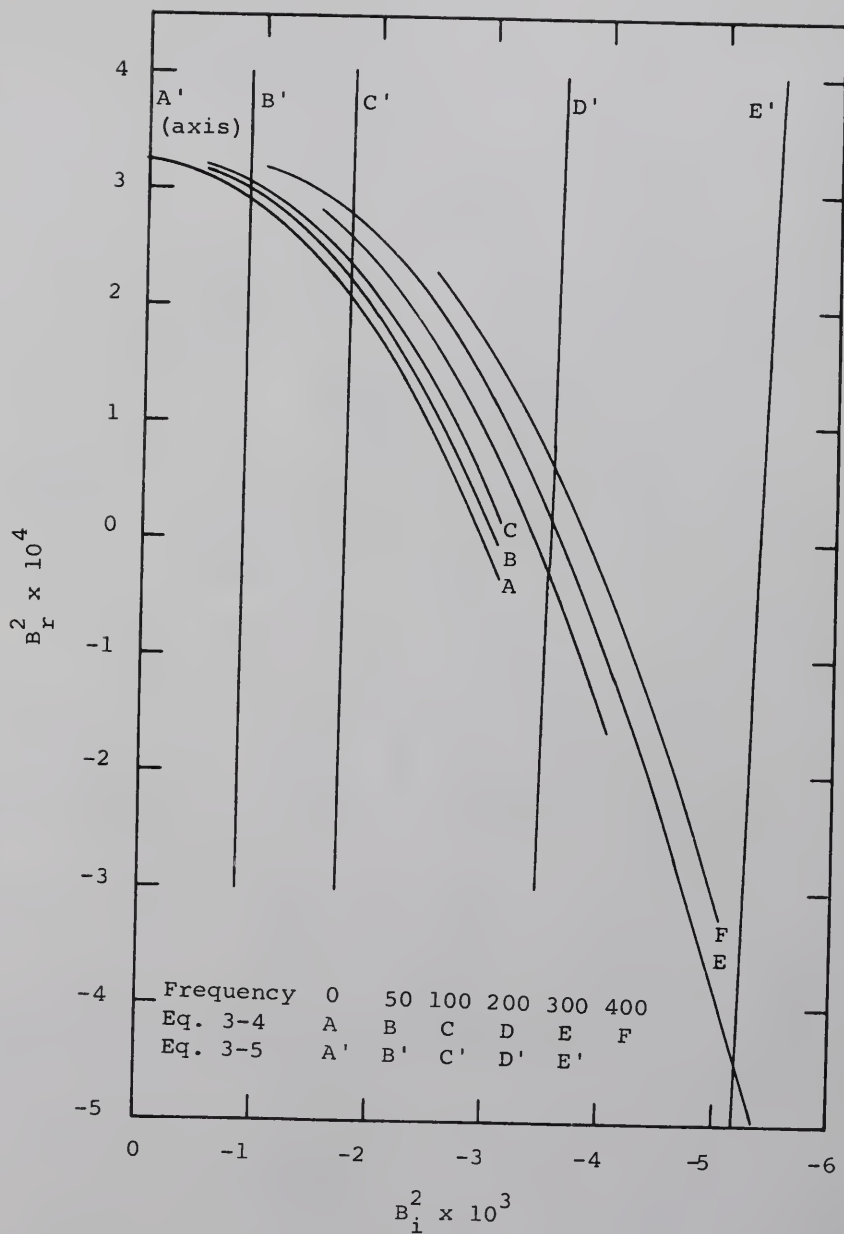
Fig. H-1. Solutions to Equations 3-4 and 3-5 for Frequencies From 0 cps to 300 cps.
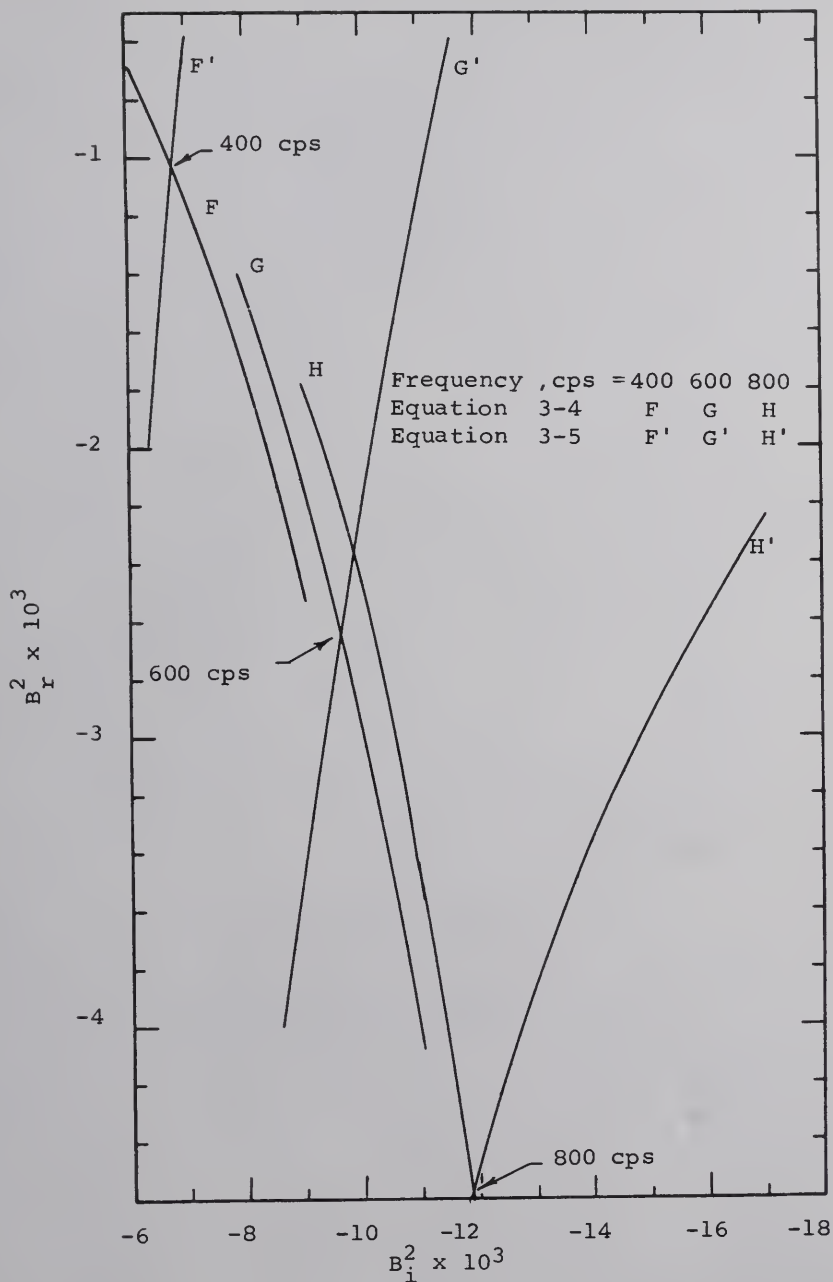
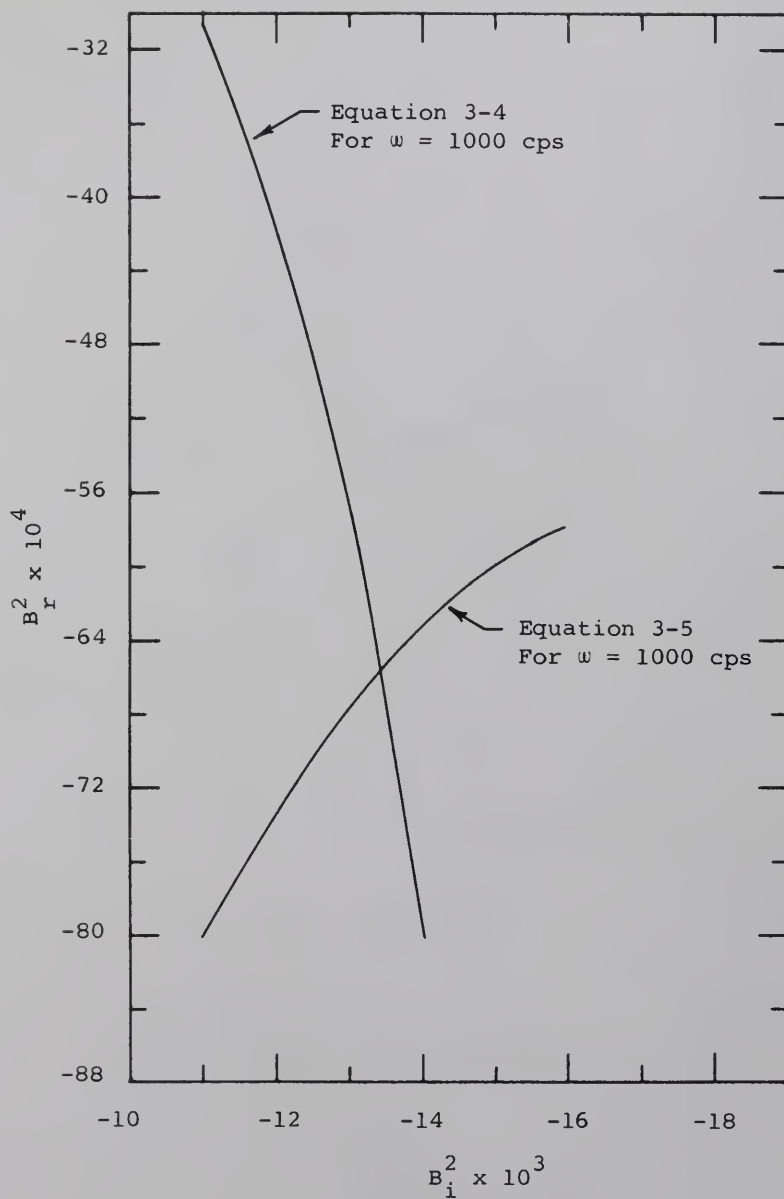Fig. H-2. Solutions to Equations 3-4 and 3-5
for 400, 600, and 800 cps.

Fig. H-3. Solutions to Equations 3-4
and 3-5 for 1000 cps.

TABLE H-2

CALCULATED RESULTS FROM AN EXACT SOLUTION OF THE FERMI AGE EQUATIONS
BY THE SEMIGRAPHICAL METHOD USING THE PARAMETERS LISTED IN TABLE H-1

Frequency Cycles/sec	BI2 $(= 2\alpha\xi)$	BR2	$\alpha^2 - \xi^2$	α	ξ
0	0	0.0003225	0.000939	-0.0306	0
50	-0.000888	0.000300	0.000962	-0.0337	0.0132
100	-0.00177	0.000235	0.001027	-0.0391	0.0226
200	-0.00350	-0.0000230	0.001285	-0.0501	0.0350
300	-0.00519	-0.000460	0.001722	-0.0600	0.0433
400	-0.00680	-0.00103	0.00229	-0.0688	0.0494
600	-0.00965	-0.00265	0.00391	-0.08463	0.0570
800	-0.01185	-0.00458	0.00584	-0.0960	0.0608
1000	-0.01341	-0.00657	0.00783	-0.108	0.0621

$$BR2CAL = \frac{K_\infty \exp\left[-(BR2)\ \tau\right]}{\epsilon L^2} \cos\left[(BI2)\ \tau + L_s\omega\right] - \frac{1}{L^2}$$

(H-1)

$$BI2CAL = \frac{-K_\infty \exp\left[-(BR2)\ \tau\right]}{\epsilon L^2} \sin\left[(BI2)\ \tau + L_s\omega\right] - \frac{\omega}{D_o}$$

(H-2)

The symbols BR2 and BI2 replace B_r^2 and B_i^2. Also, the use of the letters, CAL, on the left-hand sides of the equations serve as a reminder that BR2CAL and BI2CAL are calculated values based on assumed values of BR2 and BI2 used in the right-hand sides of the equations. Note that BR2CAL and BI2CAL are not in general equal to BR2 and BI2. When values are found such that BR2CAL is equal to BR2 in Eq. H-1, one has a solution to Eq. 3-4. Likewise, when values are found such that BI2CAL is equal to BI2 in Eq. H-2, one has a solution to Eq. 3-5.

A short FORTRAN program was written to calculate BR2CAL as a function of some arbitrarily fixed values of and BI2, and for assumed values of BR2, using Eq. H-1. The calculated values of BR2CAL were plotted versus the corresponding assumed values of BR2 for each frequency and BI2 considered. Figures H-4, H-5, and H-6 were obtained in this way for frequencies of 0, 100, and 600 cps respectively.
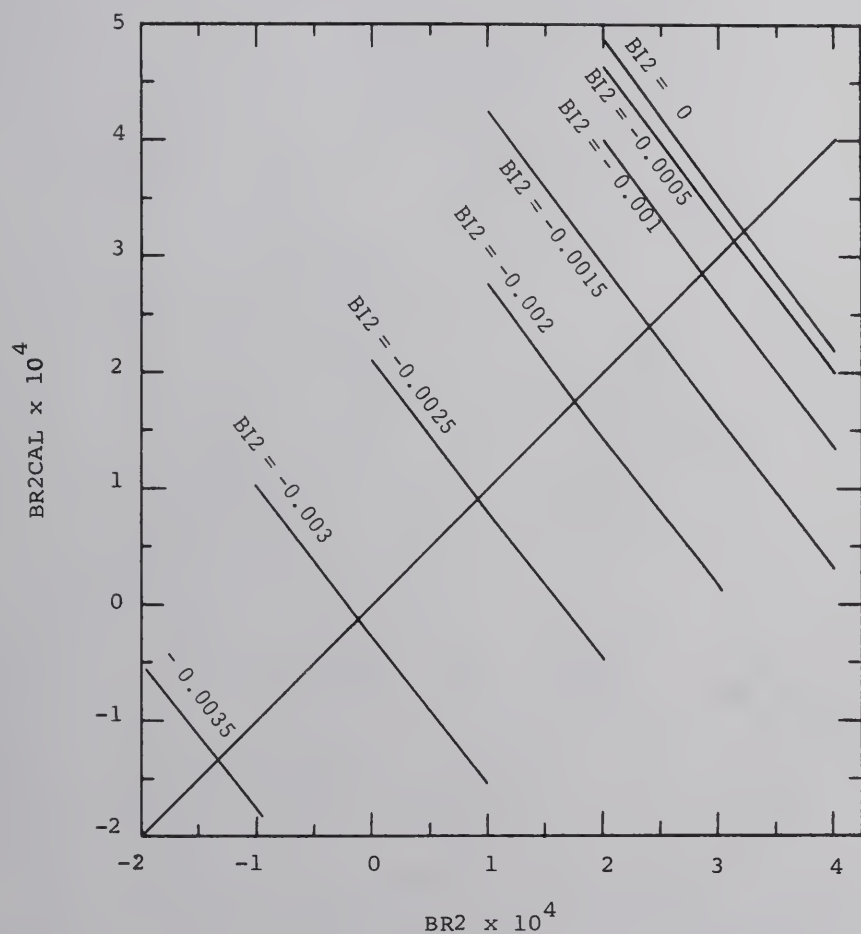
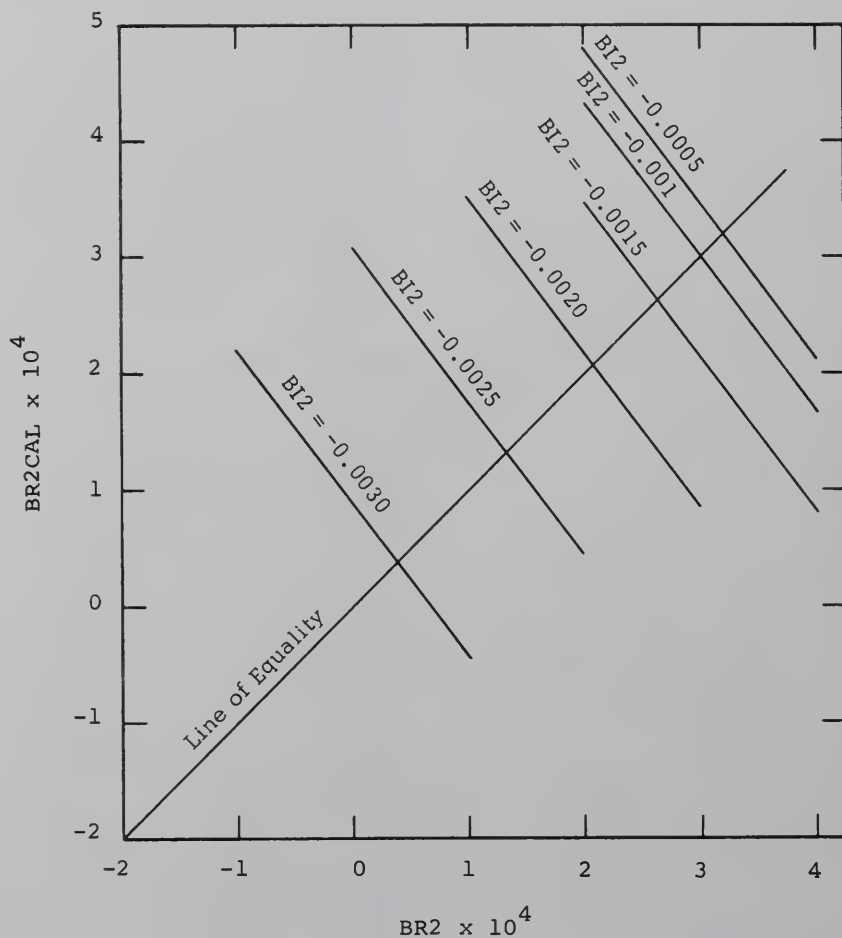Fig. H-4. Solutions to Equation H-1 for Zero Frequency and for Various Values of BI2.

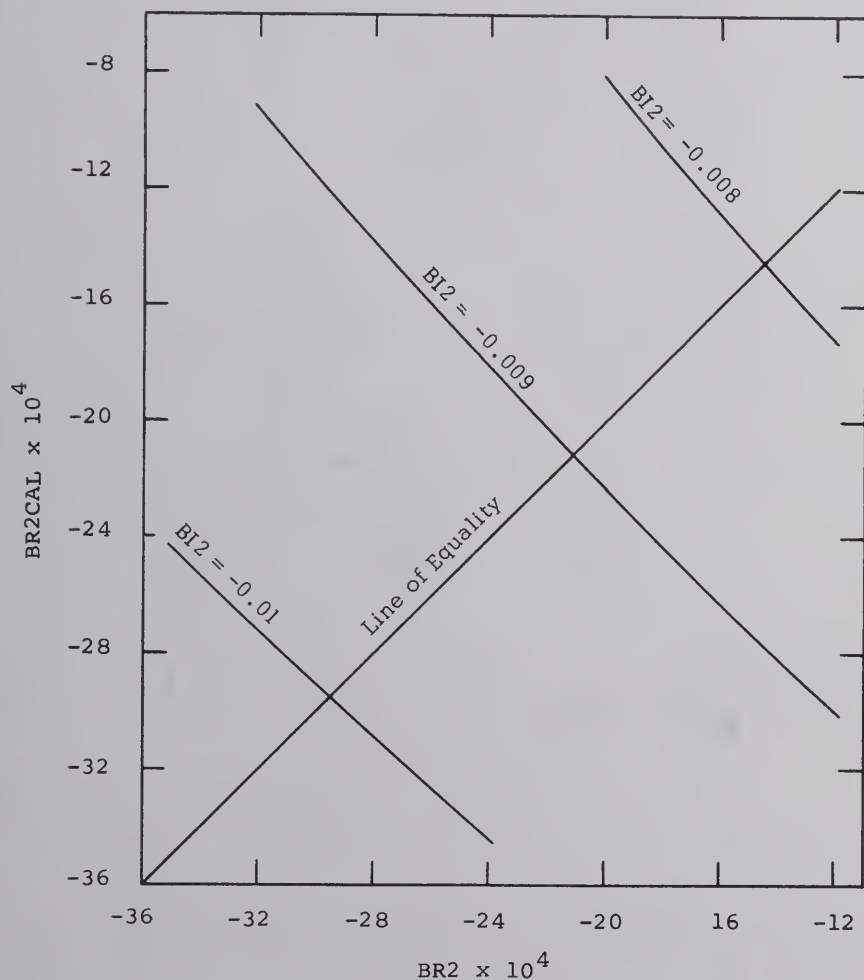Fig. H-5. Solutions to Equation H-1 for 100 cps for Various Values of BI2.

Fig. H-6. Solutions to Equation H-1 for 600 cps
for Various Values of BI2.

(Similar graphs not included here were obtained for 50, 200, 300, 400, 800, and 1000 cps.) Note that for each frequency considered, BI2 was varied, and for each differ-ent combination of ω and BI2, BR2 was varied. For each combination of ω , BI2, and BR2, BR2CAL was calculated and plotted versus BR2. On each graph, the intersections of the line BR2CAL = BR2 with the line whose points repre-sent solutions of Eq. H-1 are solutions to the trans-cendental Eq. 3-4. Curves A, C, and G in Figs. H-1 and H-2 are solutions to Eq. 3-4 and were obtained by plotting values of BR2 and BI2 taken from the intersections of Figs. H-4, H-5, and H-6.

The same FORTRAN program treated Eq. H-2 in a similar way. For each frequency considered, BR2 was varied, and for each combination of ω and BR2, BI2 was varied. For each combination of ω , BR2, and BI2, a value was computed for BI2CAL. Again, the resulting BI2CAL values were plotted versus BI2 to find the intersections with the line BI2CAL = BI2 as illustrated in Figs. H-7 and H-8 for several differ-ent frequencies. These intersections represent solutions to Eq. 3-5, and furnished the remaining information necessary for plotting the graphs in Figs. H-1, H-2, and H-3.
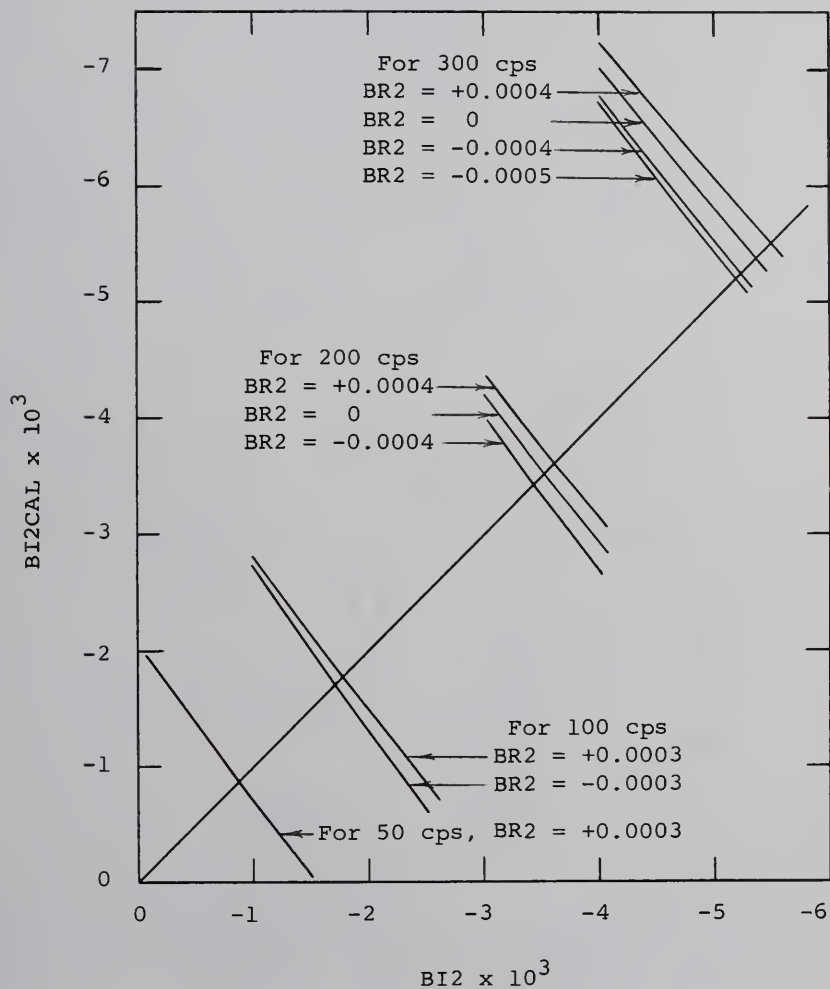
Fig. H-7.   Solutions to Equation H-2 for 50,
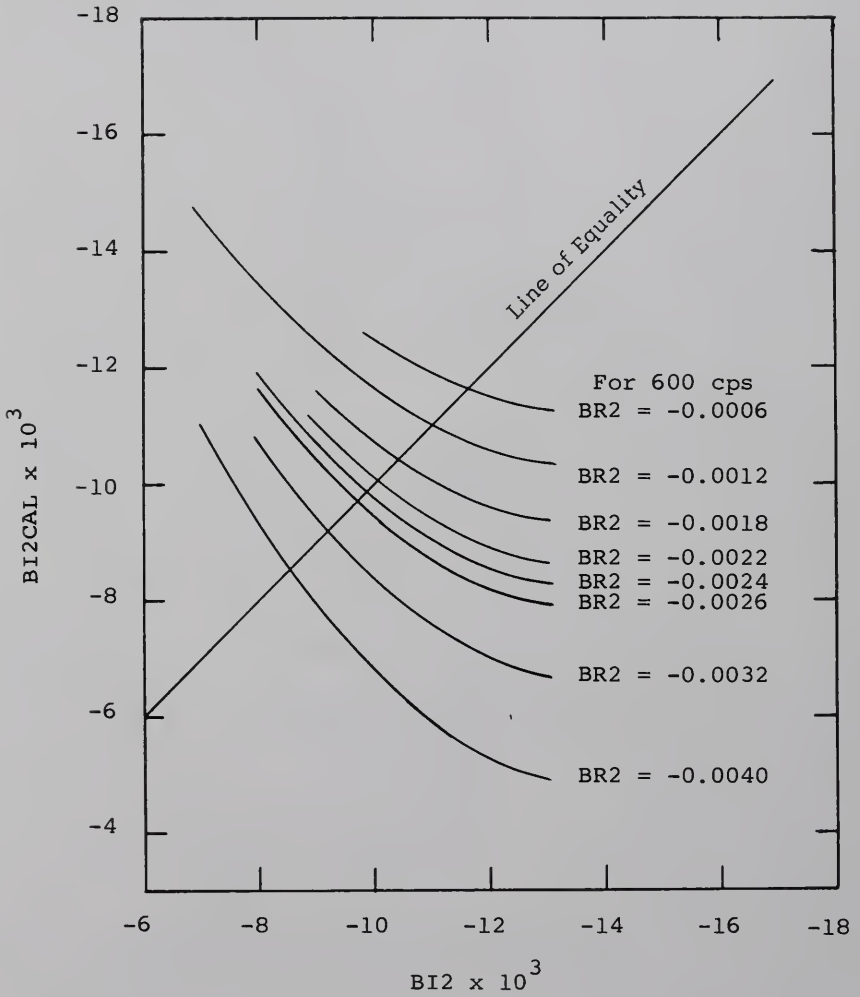   100, 200, and 300 cps for Various
            Values of BR2.

Fig. H-8.   Solutions to Equation H-2 for 600 cps
            for Various Values of BR2.

It should be understood that the computer program was not written to find directly solutions satisfying both equations simultaneously, as such a program would have been much more complicated and actually less revealing of the behavior of the equations.

The structure of the FORTRAN program is presented in Table H-3.

TABLE H-3

STRUCTURE OF FORTRAN PROGRAM WRITTEN
TO AID IN THE SOLUTION OF THE AGE-THEORY EQUATIONS

Loop Diagram	FORTRAN Statement Number	Loop	Function of Loop
	83	A	Fix Frequency.
	70	B	Fix BI2 for Equation H-1.
	75		Fix BR2 for Equation H-1. and compute BR2CAL as a
	None	C	function of ω and BI2
	52		as fixed by loops A and C, respectively.
	86	D	Fix BR2 for Equation H-2.
	87		Fix BI2 for Equation H-2 and compute BI2CAL as a
	None	E	function of ω and BR2
	89		as fixed by loops A and D, respectively.
	85		

Control statements near the beginning and end of each loop govern the range and mesh of each quantity varied. These statements were altered several times in the use of the code because the range of interest for BI2 and BR2 was dependent upon the frequency, and occasionally it became clear that the solutions lay outside the range of trial values first used in the code.

The program as given in Table H-4 has the control statements which were used to investigate frequencies from 400 to 1000 cps in steps of 200 cps, working a range of B12 values from -.020 to -.010 in steps of +.001. The range of BR2 values is from -.0040 to -.0004 in steps of +.0004 in loop B, and in steps of +.0002 in loop D. The solutions for 800 and 1000 cps lay outside the above ranges, and the program was altered for the high frequency investigation.

TABLE H-4

FORTRAN PROGRAM FOR THE AGE-THEORY EQUATIONS

```
      BT2 = 1.2616 E -03
      TAU = 1.27533 E 02
      ELSLO = 4.6 E-05
      D = 1.641 E 05
      F1 = .01087
      FREQO = +200.0
      FFREQ = 50.0
      DFREQ = 200.0
      FREQ = FREQO
   83 IF (FREQ - 199.0 ) 111, 222, 222
  111 FREQ = FREQ + FFREQ
      GO TO 333
  222 FREQ = FREQ + DFREQ
  333 CONTINUE
      WRITE OUTPUT TAPE 6,100
  100 FORMAT (48HOSTART CALCULATION WITH NEW VALUE OF FREQUENCY      )
      OMEGA = FREQ * 6.28318
      BI20 = -.021
      DBI2 = .001
      BI2 = BI20
   70 WRITE OUTPUT TAPE 6,65
   65 FORMAT( 75HOHOLD FREQUENCY AND BI2 CONSTANT      COMPUTE BR2CAL AS A
                                                    )
CFUNCTION OF BI2
      BI2 = BI2 + DBI2
      ANGLE = BI2 * TAU + ELSLO * OMEGA
      COSANG = COSF (ANGLE)
      BR20 = -.0044
      DBR2 = .0004
```

TABLE H-4 (Continued)

```
      BR2  = BR20
   75 BR2  = BR2 + DBR2
      F2   = EXPF ( -BR2 * TAU)
      ELSQIN = 1.0 /( EL ** 2.0)
      BR2CAL = F1* F2 * COSANG - ELSQIN
      CHISQ = BT2 - BR2CAL
      WRITE OUTPUT TAPE 6,50,FREQ,BI2,BR2,BR2CAL,CHISQ
   50 FORMAT (8H0FREQ = E10.3,9H       BI2 = E12.5,11H       BR2 = E12.5,
  C12H    BR2CAL = E12.5,12H       CHISQ = E12.5 )
      WRITE OUTPUT TAPE 6,51,F1,F2,ANGLE,COSANG,ELSQUIN
   51 FORMAT (6H F1 = E12.5,9H      F2 = E12.5,11H     ANGLE = E12.5,
  C 12H    COSANG = E12.5, 12H    ELSQIN = E12.5 / )
      IF ( BR2 + .0004 )  75,52,52
   52 IF ( BI2 +.006 ) 70,82,82
   82 BR20 = -.0044
      DBR2 = .0002
      BR2 = BR20
   86 WRITE OUTPUT TAPE 6,186
  186 FORMAT (75H0HOLD FREQUENCY AND BR2 CONSTANT    COMPUTE BI2CAL AS FU
      CNCTION OF BI2
      BR2 = BR2 + DBR2
      BI20 = -.021
      DBI2 = .001
      BI2 = BI20
   87 BI2 = BI2 + DBI2
      ANGLE = ( BI2 * TAU) + (ELSLO * OMEGA)
      SINANG = SINF (ANGLE)
      F2 = EXPF (-BR2*TAU)
      OMEDO = OMEGA/D
      BI2CAL =-F1*F2*SINANG-OMEDO
      WRITE OUTPUT TAPE 6,152,FREQ,BR2,BI2,BI2CAL
  152 FORMAT (8H0FREQ = E10.3,9H     BR2 = E12.5,11H       BI2 = E12.5,
```

TABLE H-4 (Continued)

```
C 12H    BI2CAL = E12.5 )
    WRITE OUTPUT TAPE 6,53,F1,F2,ANGLE,SINANG,OMEDO
53 FORMAT (6H F1 = E12.5,9H    F2 = E12.5,11H    ANGLE = E12.5,
C  12H    SINANG = E12.5,11H    OMEDO = E12.5 /)
    IF (BI2 +.006 ) 87,89,89
89 IF (BR2 +.0004 ) 86,85,85
85 IF (FREQ - 999.0) 83,90,90
90 CALL EXIT
```

LIST OF REFERENCES

1.   M. N. Moore, "The Dispersion Law of a Moderator," to
      be published in Nuclear Science and Engineering.

2.   A. M. Weinberg and H. C. Schweinler, "Theory of Oscilla-
      ting Absorber in a Chain Reactor," Physical Review, 74
      851-863 (1948).

3.   A. M. Weinberg and E. P. Wigner, The Physical Theory
      of Neutron Chain Reactors, University of Chicago Press,
      Chicago (1958).

4.   V. Raievski and J. Horowitz, "Determination of the Mean
      Transfer Free Path of Thermal Neutrons by Measurement
      of the Complex Diffusion Length," Proceedings of the
      International Conference on the Peaceful Uses of
      Atomic Energy - Geneva. 1955, 5, 42-51, United Nations,
      New York (1956).

5.   R. E. Uhrig, "Operating Characteristics of a Graphite
      Moderated Subcritical Assembly," Nuclear Science and
      Engineering, 5, 120-126 (1959).

6.   R. E. Uhrig, "Oscillating Techniques in a Subcritical
      Assembly," Proceedings of the University Subcritical
      Assemblies Conference, 1961, TID-7619, 161-182 (1962).

7.   R. S. Booth, "Neutron Wave Propagation in a Subcritical
      Assembly," Master's Thesis, University of Florida (1962).

8.   R. B. Perez, R. S. Booth, R. S. Denning, and R. H. Hartley,
      "Propagation of Neutron Waves in Subcritical Assemblies,"
      Transactions of the American Nuclear Society, 7, 49-50
      (1964).

9. R. B. Perez and R. E. Uhrig, "Propagation of Neutron Waves in Moderating Media," <u>Nuclear Science and Engineering</u>, <u>17</u>, 90-100 (1963).

10. H. L. Hussmann, "Characteristics of Neutron Waves in a Subcritical Assembly," Master's Thesis, Iowa State University of Science and Technology (1960).

11. M. N. Moore, "The Propagation of Neutron Bursts and the Determination of the System Dispersion Law," <u>Transactions of the American Nuclear Society</u>, <u>7</u>, 278-279 (1964).

12. R. B. Perez, R. S. Booth, and R. H. Hartley, "Experimentation with Thermal Neutron Wave Propagation," <u>Transactions of the American Nuclear Society</u>, <u>6</u>, 287-288 (1963).

13. R. L. Brehm, "The Analysis of Neutron Wave Experiments," Ph.D. Dissertation, University of California at Los Angeles (1965).

14. M. N. Moore, "The Determination of Reactor Dispersion Laws from Modulated-Neutron Experiments," <u>Nuclear Science and Engineering</u>, <u>21</u>, 565-574 (1965).

15. R. L. Brehm, "Comments on the Existence of Exceptional Frequencies in Multiplying Media," <u>Nuclear Science and Engineering</u>, <u>21</u>, 575-576 (1965).

16. R. S. Booth, "A Theoretical and Experimental Study of Neutron Wave Propagation in Moderating Media," Ph.D. Dissertation, University of Florida (1965).

17. J. M. McCormick and M. G. Salvadori, <u>Numerical Methods in FORTRAN</u>, Prentice-Hall, New Jersey, 61-65 (1964).

18. R. H. Hartley, "Propagation and Detection of Pulses of Thermal Neutrons," Master's Thesis, University of Florida (1964).

19. N. K. Ganguly and A. W. Waltner, "Measurement of Neutron Diffusion Parameters of D_2O at Different Temperatures by the Pulsed Source Method," <u>Transactions of the American Nuclear Society</u>, <u>4</u>, 282 (1961).

20.   F. R. Westfall and A. W. Waltner, "Measurements of Nat-
      ural Uranium D_2O Lattices by the Pulsed Neutron Technique,"
      Transactions of the American Nuclear Society, 5, 386
      (1962).

21.   G. Kussmaul and H. Meister, "Thermal Neutron Diffusion
      Parameters of Heavy Water," Journal of Nuclear Energy
      A/B, 17, 411 (1963).

22.   B. K. Malaviya and A. E. Profio, "Measurement of the
      Diffusion Parameters of Heavy Water by the Pulsed
      Neutron Technique," Transactions of the American
      Nuclear Society, 6, 58 (1963).

23.   T. F. Parkinson and N. J. Diaz, "Pulsed and Static
      Neutron Measurements in D_2O-Moderated Lattices," Summary
      Report for U. S. Atomic Energy Commission under Contract
      AT(38-1)-374 (1965).

24.   P. B. Parks and N. P. Baumann, "Pulsed Neutron Measure-
      ments of Neutron Diffusion Parameters in D_2O," Trans-
      actions of the American Nuclear Society, 8, 436 (1966).

25.   N. J. Diaz, "Pulsed and Static Neutron Measurements on
      Heavy Water Moderated Lattices," Master's Thesis, Uni-
      versity of Florida (1964).

26.   H. Meister, "Pulsed Neutron Experiments on Subcritical
      Heavy Water Natural Uranium Lattices," Journal of
      Nuclear Energy, 17, Parts A/B, 97-114 (1963).

27.   E. R. Cohen, "Exponential Experiments on D_2O-Uranium
      Lattices," Proceedings of the International Conference
      on the Peaceful Uses of Atomic Energy, 5, 268 (1955).

28.   T. F. Parkinson, N. J. Diaz, et al., "Pulsed and Static
      Measurements in Light and Heavy Water Exponentials,"
      Proceedings of the IAEA Symposium on Exponential and
      Critical Experiments, 3, Amsterdam, Netherlands
      (September, 1963).

29.   P. B. Daitch, et al., "CEPTR -- An IBM Code to Solve
      the P-3 Approximation to the One-Velocity Transport
      Equations in Cylindrical Geometry," AEC Research and
      Development Report, TID-6940 (1959).

30. R. B. Razminas, "Temperature Coefficients of D_2O-Moderated Systems," Master's Thesis, University of Florida (June, 1962).

31. J. M. Tull Metal and Supply Co., Inc. <u>Metal</u> <u>Catalog</u> <u>No</u>. <u>58</u>, Atlanta, Georgia, 2 (1958).

32. F. E. Driggers and J. C. English, "Calculation of Heavy Water Lattice Parameters, "AEC Research and Development Report, DP-661 (November, 1961).

BIOGRAPHICAL SKETCH

Johnny Hall Dunlap was born along with a twin brother, Julian Lee Dunlap, in La Grange, Georgia on January 27, 1932, to Mr.and Mrs. R. L. Dunlap. He was graduated in 1949 from the La Grange High School of La Grange, Georgia. He obtained the Bachelor of Engineering degree in Mechanical Engineering from Vanderbilt University in Nashville, Tennessee, in 1953. He held an A.E.C. Radiological Physics Fellowship at Vanderbilt University, and received the degree of Master of Science in Physics from Vanderbilt University in 1956.

He joined the faculty of the Vanderbilt University School of Engineering in 1955, and taught in the area of Applied Mechanics until taking a leave of absence to attend the International School of Nuclear Science and Engineering at Argonne National Laboratory from 1957 to 1959. He returned to Vanderbilt to teach Applied Mechanics and Nuclear Engineering until taking a second leave in September, 1961, to study Nuclear Engineering at the University of Florida, where he held a Ford Foundation Fellowship, taught a course in Radiation Safety, and later held a graduate assistantship
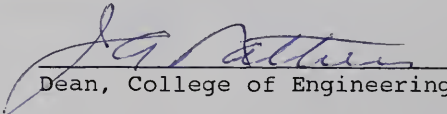
265

in the Department of Nuclear Engineering. He returned to the Faculty of the School of Engineering at Vanderbilt University in February, 1966.

Johnny Hall Dunlap married the former Mary Larimore Burton of Nashville, Tennessee on December 22, 1954. They have one daughter, Cindy, who was born January 22, 1958.

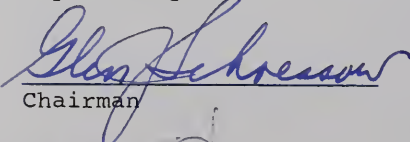He is a member of the Society of Tau Beta Pi, Sigma Xi, and the Health Physics Society.

This dissertation was prepared under the direction of the chairman of the candidate's supervisory committee and has been approved by all members of that committee. It was submitted to the Dean of the College of Engineering and to the Graduate Council, and was approved as partial fulfillment of the requirements for the degree of Doctor of Philosophy.
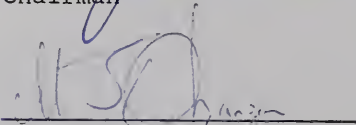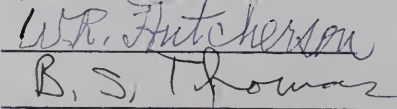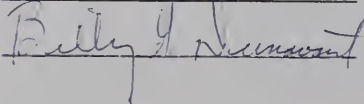
December, 1967

_____
Dean, College of Engineering

_____
Dean, Graduate School

Supervisory Committee:

_____
Chairman

_____

_____

_____

_____